# COMPUTATIONAL STUDIES OF BIOLOGICAL ION CHANNELS

by

**William Joseph Kowallis**

B.S. Chemistry, University of Pittsburgh, 2001

M.S. Chemistry, University of Pittsburgh, 2009

Submitted to the Graduate Faculty of the

Dietrich School of Arts and Sciences in partial fulfillment

of the requirements for the degree of

Doctor of Philosophy

University of Pittsburgh

2016

UNIVERSITY OF PITTSBURGH

DIETRICH SCHOOL OF ARTS AND SCIENCES

This dissertation was presented

by

William Joseph Kowallis

It was defended on

July 19th, 2016

and approved by

David H. Waldeck, Professor, Department of Chemistry

Kenneth D. Jordan, Professor, Department of Chemistry

Peter F.M. Koehler, Professor of Physics emeritus, University Honors College

Dissertation Advisor: Rob D. Coalson, Professor, Department of Chemistry

**COMPUTATIONAL STUDIES OF BIOLOGICAL ION CHANNELS**

William J. Kowallis, PhD

University of Pittsburgh, 2016

Structural and functional characteristics of three biological ion channels were studied. First, current-voltage characteristics were calculated using non-equilibrium molecular dynamics (NEMD), Brownian Dynamics (BD), and Poisson-Nernst-Planck theory (PNP) for the ion channel alpha-hemolysin, comparing and contrasting the results among each other and experimental values. Results show that all methods produce qualitatively accurate results in terms of selectivity, where quantitave accuracy increases with more atomistic detailed simulation methodology. Results from NEMD simulations show that a specific location within the pore may account for selectivity of the channel, and point mutation of one residue (lys147) would likely result in a change in selectivity. The residue was mutated to serine, structural viability was tested with all-atom molecular dynamics, and PNP and BD calculations of the mutated structure show that selectivity is changed via this mutation. Second, pH dependence of current-voltage characteristics of alpha-hemolysin were studied using PNP and compared to experimental data, applying pH-dependent charge states determined from calculated pKa values for all titratable residues in the structure. Results indicate that altered charge states of both internal and external residues most accurately described experimental data. Third, Poisson-Boltzmann and PNP calculations were performed to determine the functional state of the crystallographic structure of the mitochondrial channel VDAC1, finding that the current-voltage properties indicated that structure represents the open conformation of the channel. Calculations were repeated using mutant channel structures,

reflecting experimental results showing changes in selectivity. Two proposed gating motions of the channel were explored, with calculated current-voltage results from the gated structures not reflecting experimental changes in current-voltage properties, suggesting that the two proposed gating methods were not correct for this channel. Last, Poisson-Nernst-Planck calculations were performed of the influx of ferrous ions ($Fe^{2+}$) into human H-ferritin protein. All-atom molecular dynamics simulation was used to determine both the equilibrium pore structure as well as the diffusion constant profile through the channel, using Force-Force Autocorrelation Function methodology. Results show relatively slow (compared to other channels) transit of $Fe^{2+}$ ions through the channel due to greatly reduced internal diffusion constants (from bulk values) within the ferritin pore as well as low physiological concentration of $Fe^{2+}$.

## TABLE OF CONTENTS

## LIST OF TABLES

## LIST OF FIGURES

## LIST OF EQUATIONS

# PREFACE

I would like to thank my advisor Professor Rob Coalson for his patience and encouragement, my family, my friends, my committee members, and my colleagues, past and present, for their support. Knowing all of you is my proudest accomplishment.

# 1.0 INTRODUCTION

## 1.1 THE IMPORTANCE OF ION CHANNEL STUDIES

One of the essential characteristics of eukaryotic cellular structure is compartmentation. The means by which cells are protected from the environment as well as compartmentalized within themselves is through the presence of phospholipid bilayers, or membranes, generally being anywhere from 40 to 60 Angstroms in thickness. These bilayers are amphipathic in nature, meaning that they are comprised of both hydrophilic regions (surface glycerophosphate head groups) and a hydrophobic region (internal hydrocarbon tails). A consequence of this structure is that bilayers present a barrier to the permeation of both charged and polar solutes as well as (partially) water (Figure 1.1) through their hydrophobic interiors. As such, small solute molecules which are necessary for numerous cellular processes such as inter/intra-cellular signaling, metabolism, and mitosis are unable to pass through biological membranes without the presence of additional structures to mediate their diffusion.

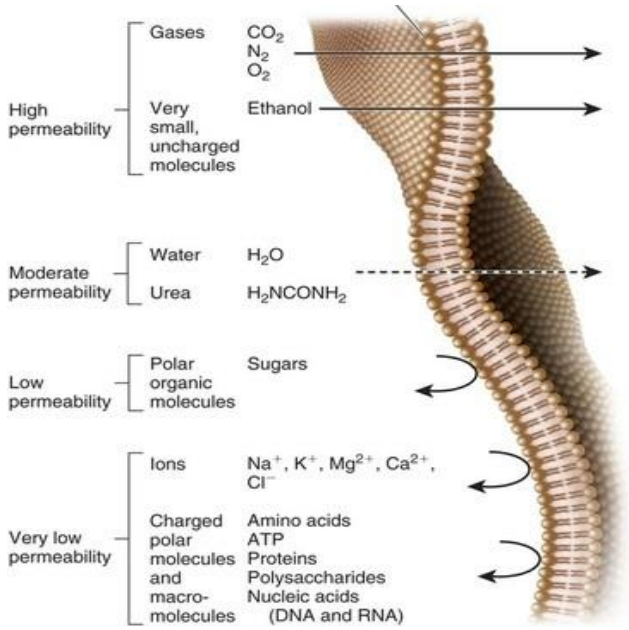


**Figure 1.1:** Diffusivities of various molecules through a phospholipid bilayer. (TGES Biology, 2014)

Organisms are able to transport small polar and charged solutes (typically less than 25 atoms (Voet et al., 2011)) across their membranes by using three types of transport protein molecules: channels, carriers, and pumps; larger molecules cross the membrane via processes which deform the membrane itself, such as topogenesis and endocytosis. Both channels as well as carriers are passive-type transporters, meaning that they facilitate the diffusion of solutes down their respective electrochemical gradients, while pumps require chemical energy, e.g. ATP hydrolysis or coupling to a spontaneous process, in order to move solutes against their electrochemical gradients. Carriers typically physically bind solvent molecules and then change conformation in order to release the solvent on the opposite side of the membrane, and channel proteins, also commonly called ion channels, span the membrane and maintain an aqueous pathway for the permeation of charged solutes (Figure 1. 2a). While both carriers and ion channels are selective to one or few types of solutes, ion channels are able to transport molecules much more rapidly, considering that they are able to maintain an open pathway for diffusion. For

example, a common potassium cation carrier protein, Valinomycin (Figure 1.2b), will transport approx. 10,000 $K^+$ ions/sec., while an ion channel such as the nicotinic acetylcholine receptor (nAChR) (Figure 1.2c) will allow permeation rates of ten million $K^+$ ions/sec or more. Cellular processes that require high diffusion rates of ions, such as signaling events or nerve impulses, thus depend on the function of ion channels in order to occur

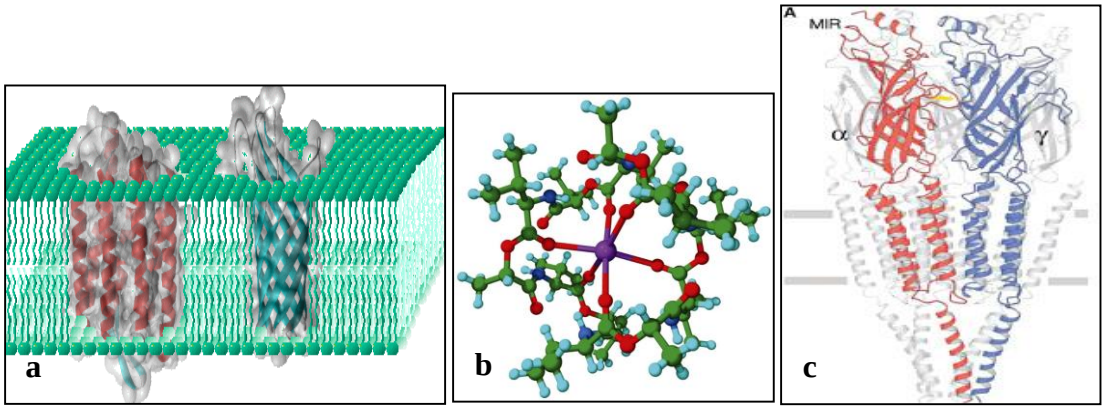


**Figure 1.2:** Examples of ion channels and carriers. (Voet et al., 2008). **a:** Protein ion channels Bacteriorhodopsin (left) and OpcA (right) forming aqueous pores through a bilayer. **b:** Structure of a Valinomycin carrier molecule. **c:** A Nicotinic acetylcholine receptor ion channel.

Ion channels comprise a superfamily of over 300 different proteins, diverse in terms of structure as well as functionality. In general, they are classified according to functional properties, including both selectivity of solute(s) as well as how they are gated, i.e. the mechanism by which channels are opened or closed. Porins are the simplest type ion channels, and are typically found on the outer membranes of bacteria, mitochondria, and chloroplasts. Porins are comprised of β-barrel secondary structure (Figure 1.2a) and only have moderate selectivity for ions and small solutes. Eukaryotic ion channels are typically more complex structurally as well as functionally. They are usually multimeric proteins made up of α-helices, connecting loops and β-sheets (Figure 1.2c) which, upon assembly, form narrow transmembrane pores that are highly selective for one or few ion types. Additionally, eukaryotic ion channels have specific gating mechanisms,

including mechanosensitive ion channels, which open/close in response to deformations in the lipid bilayer, receptor channels whose gating are regulated by binding of external ligands or internal molecular signals, voltage-gated channels that open and close in response to charge balance across the membrane, and light-activated channels, which gate in response to exposure to specific wavelengths of electromagnetic radiation.

The idea of mobile charge playing an important role in biological function can be traced to the 1780's and the experiments of Luigi Galvani, who found that touching the exposed sciatic nerve of dissected frog legs with a charged electrode (Figure 1.3) would trigger muscle contraction (Wells, 1859). Following these findings, later investigations into the existence of selective pathways for ions through biological membranes particularly targeted nerve cells. Kenneth Cole and Howard Curtis performed electrophysiological studies of action potential propagation in nerve cell axons (Figure 1.3b) in the 1930's (Cole and Curtis, 1939), and were successful in inserting electrodes into nerve cells and taking electrical measurements during nerve response. These studies showed that stimulation of the nerve cell with electric current, triggering a nervous response, would cause a measureable change in the membrane potential, indicative of ion flow through the membrane. The "giant axon" of the squid, which is responsible for control of the squid's propulsion motion, was first utilized by English zoologist and neurophysiologist John Zachary Young in 1936. This particular axon can be up to 1 mm in diameter, which is up to 1000 times larger than mammalian axons, and, because of this larger size, made it much easier to conduct electrophysiological studies. While these experiments were groundbreaking in the field of electrophysiology, they still were limited in their scope, as they did not allow experimentalists to control the membrane potential nor did they allow for researchers to identify which ions were flowing through the membrane.

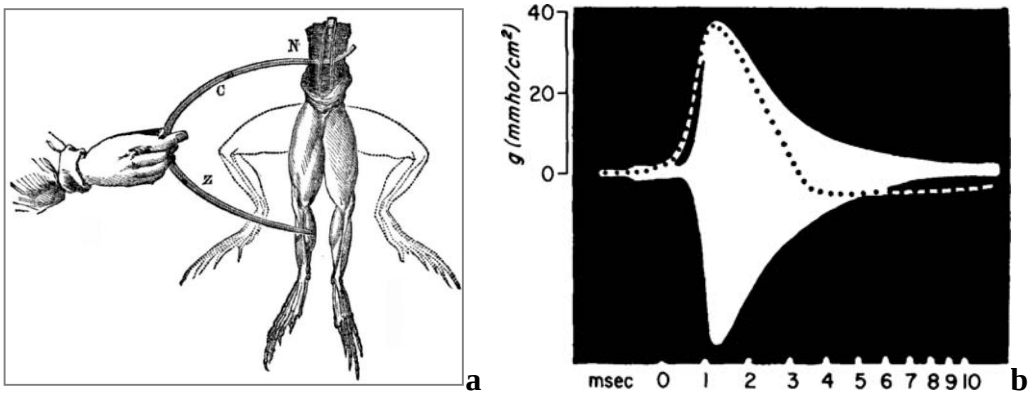


**a** **b**

**Figure 1.3: a:** Diagram from Luigi Galvani's experiments on electrophysiology. Touching a charged metallic object to the sciatic nerve and leg of a dissected frog triggers muscle contraction (Wells, 1859). **b:** Conductance measurement of the squid giant axon membrane during nerve response, showing an increase in conductance of ions through the membrane when the nerve cell is triggered by an electric stimulus (Cole and Curtis, 1939).

These electrophysiological measurements were continued and refined by Cole along with George Marmont, leading to the development of the voltage clamp technique in the 1940's, a breakthrough in membrane research (Cole, 1949, Hodgkin et al., 1949). Using a feedback amplifier device, this technique (Figure 1.4) allowed voltage across the membrane to be set at a specific value, and the transmembrane ionic currents to be measured by monitoring current sent through the lead electrode to maintain a constant voltage. Using this technique, Alan Hodgkin and Andrew Huxley resolved details of the ionic nature of the action potential through nerve cell axons in 1952. By varying both the membrane potential and extracellular electrolyte composition, they found that permeabilities of $K^+$ and $Na^+$ contribute separately to the action potential of the squid giant axon (Hodgkin and Huxley, 1952a,b). Their results showed that membrane permeability of each of these ions was characterized by different selectivity and separable kinetics, but the conductance of both ions was voltage dependent, leading Hodgkin and Huxley to conclude that there are separate ionic pathways for $K^+$ and $Na^+$ through the membrane. Their model not only predicted different features of the action potential upon further experimentation, but served as key

insight into the functionality of ion channels. Hodgkin and Huxley were awarded the Nobel Prize in medicine in 1963 for their work in this field.

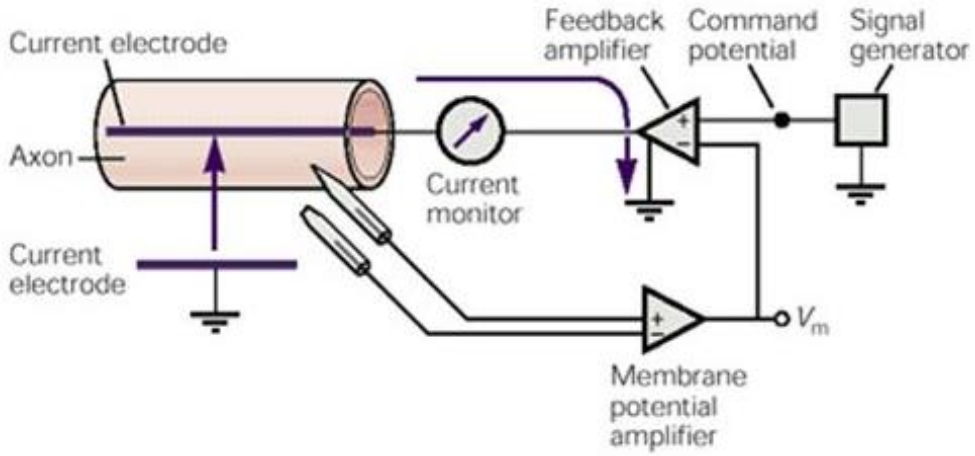


**Figure 1.4:** A diagram of voltage clamp on a nerve axon. Transmembrane potential is measured between an intracellular micropipette electrode and an electrode in the extracellular fluid by the membrane potential amplifier and compared with the clamp voltage by the feedback amplifier. A current (upward arrow) is generated to bring the membrane potential to the clamp voltage, and the current is measured by the current monitor, or ammeter. (Mann, 1997)

Membrane electrophysiology continued to be studied through the 1970s in the manner pioneered by Cole, Hodgkin and Huxley, meaning that functional detail was limited to measurement of mobile charge flux through whole cells, or with the development of artificial membranes (Chang, 1964), through sections of membrane (Hladkey and Haydon, 1972). Even with this limitation, important advances were made, including the discovery that several compounds that are identified as toxins or neurotoxins block the permeation of specific ions through membranes (Narahashi et al., 1964; Armstrong et al., 1965). This information would later prove to be essential in identifying and isolating activity of specific ion channels within membranes having multiple channel types. Although it had become apparent that unique pathways

existed for ions to traverse biological membranes, the means by which this occurred was still unclear. Examination of smaller sections of artificial membrane led researchers to a discovery that ion current through membranes would fluctuate in a step-wise manner, indicating that, at least in some scenarios, individual structures within bilayers regulate ion permeation by having open and closed states (Bean et al., 1969; Stevens, 1972; Hladkey and Haydon, 1972).

In 1976, Erwin Neher and Bert Sakmann developed a new technique in electro-physiology, whereby very small sections of a biological membrane could be isolated for measurement of current-voltage properties. In this method, known as the patch clamp technique (Neher and Sakman, 1976), a microscopic-scale glass pipet is placed on the surface of a cell, small enough to isolate few or even single channel structures within the pipet tip. Signal amplification allowed Neher and Sakman to measure current on the picoampere ($10^{-12}$ amps) scale, a sensitivity sufficient to detect ion flow through single channels. This technique continues to be used to the present day, albeit with some improvements, such as creating suction inside the glass pipet to form a tighter seal against the membrane, resulting in reduced noise (Hamill et al., 1981). The ability to isolate and monitor the current-voltage activity of ion channels in situ has allowed researchers to determine many functional dynamics of these structures, including selectivity, ion permeation rates, and factors that affect their gating.

Along with advances in experimental techniques for measurements of ion channel function there has been extensive research into determining the structure of ion channels as well over the past 40 years, as per the maxim in protein chemistry that *structure dictates function*. The advent of recombinant DNA techniques in the 1970's (Jackson et al., 1972) provided the means to obtain sequence information about genes and therefore the proteins they coded for. Genetic information specific to proteins, including ion channels, could be isolated and then transferred, or transfected,

into easily grown bacteria, such as *E. coli* (Cohen et al., 1973). Up to this point, researchers had been dependent on natural tissue samples as the only available source of ion channels for study, but transfected bacteria could now be used as a source to produce large quantities of specific proteins. Being able to correlate genes with protein segments allowed molecular biologists to determine that some ion channels consisted of more than a single protein subunit. For example, the channel nAChR was found to consist of 5 polypeptide subunits (pentameric) with a total molecular weight of about 290 KDaltons, corresponding to 290,000 grams per mole, along with a full mapping of the amino acid sequences, or primary structures, of each of these subunits (Noda et al, 1982; Numa et al., 1983).

With primary structures of some ion channels known, it was possible to begin making predictions of what these ion channels should look like in 3-dimensional space (secondary, tertiary, and quaternary structure). Being integral membrane proteins, ion channels must have distinctive structural components: conserved secondary structures for segments that span the bilayer interior (in order to shield the polar functional groups of the backbone from the phospholipid tails), nonpolar R-groups on amino acids that directly contact the bilayer interior, and residues with polar groups that would comprise the aqueous pores and surfaces of the channel structure on either side of the membrane. Utilizing these general rules, along with primary structure information, the first detailed model of a eukaryotic ion channel was developed for nAChR in 1983 (Noda et al., 1983). This same group of researchers was able to further illustrate functionality within the nAChR channel structure by utilizing a then recently-developed technique, site-directed mutagenesis (Hutchison et al., 1978), to alter single residues within the channel, observe resultant changes in behavior, and thereby determine the roles of individual amino acids within the channel function (Imoto et al., 1988).

Considering the vital role that ion channels play in physiological function, understanding their behavior was quickly expanding as a field of research in molecular biology and pharmacology, particularly as researchers began to find that many human diseases are the direct result of ion channel malfunction. Mutations of ion channel genes result in incorrect amino acids within the primary structures of channel proteins, possibly causing either a loss or a gain of channel function. Loss-of-function mutations in ion channels often lead to recessive diseases, such as cystic fibrosis resulting from the malfunction of the chloride channel CFTR in lung epithelia (Riordan et al., 1989) or Bartter syndrome resulting from a mutation that renders the channel CLCNKB inoperable, an essential mechanism of fluid and solute exchange in the kidneys (Simon et al., 1997). Further advancement in resolving the structures of ion channels was essential in order to explain and, if necessary, regulate their function through therapeutic means. Ion channelopathies continue to be connected to a growing number of diseases, and presently over half of newly developed medications specifically target ion channel function (Elinder et al., 2007).

Ion channels present a unique problem in terms of experimental determination of structure. X-ray crystallography has long been utilized to determine the structures of aqueous proteins (Kendrew et al., 1958, Muirhead 1963) to atomic-scale resolution. These types of proteins are structurally stable in aqueous media and, when purified and suspended under appropriate pH and salt concentrations, will agglomerate into crystals suitable for x-ray diffraction. Ion channels, however, must be situated within a membrane environment, requiring exposure to clearly defined polar and nonpolar surroundings in order to maintain a natural, or native, conformation. If ion channel proteins were to be placed into an aqueous medium, without a membrane being present, they would assume a conformation that would be markedly different than their native structure.

Taking x-ray crystallographic images of purified ion channel proteins, therefore, is not possible in the manner typical of many other protein types.

The first in-situ structure of an ion channel was obtained using Nuclear Magnetic Resonance, or NMR (Arseniev et al., 1985), for the small ion channel Gramicidin A, which is excreted by the soil bacteria *Bacillus brevis* as a defense mechanism against other micro-organisms. By incorporating Gramicidin A channels into sodium dodecyl sulfate micelles and then suspending these micelles in media, solution state NMR was used to resolve the 17 residue structure. Unfortunately, NMR is not an effective method for resolving the structures of other, typically much larger, ion channels, due to overlapping peaks and peak broadening that become prohibitive in larger protein structures (Wüthrich, 1990). Fortunately, there have been several advances in crystallization methodologies, including complexation of channel proteins with antibody fragments (Ostermeier et al., 1995), use of protein homologs (Kendrew et al., 1957), addition of heavy atom reagents (McPherson, 1999), and using heavy water as a medium (Lutter et al., 1993), that have allowed researchers to determine the structures of several ion channel systems. As advances are made in determining the structures of ion channels, new insight is continually being gained in terms of the operation of these proteins. However, the large majority of ion channel structures have yet to be accurately determined; and crystallographic images themselves represent only snapshots and cannot by themselves infer the overall functionality of such dynamic systems.

## 1.2 COMPUTATIONAL METHODS FOR ION PERMEATION STUDY

Along with these developments in experimental studies of ion channels there were also advances in the theoretical descriptions of their behavior. Although several competing theories had been proposed following the work of Hodgkin and Huxley as to how ions are physically able to traverse the bilayer, the model describing protein molecules as structures that form aqueous pores that span the membrane, and thus allow passage of ions, was established as the mostly likely and energetically favorable (Hille, 2001; Bezanilla, 2006). In accordance with this type of scenario, various methods have been proposed for modeling the passage of ions across the bilayer through a channel protein, including Molecular Dynamics (MD) (Crozier et al., 2001a), Poisson-Nernst-Planck (PNP) Theory (de Levie et al., 1971, Kurnikova et al., 1999), and Brownian Dynamics (BD) (Cooper et al., 1985), where each of these methods include differing amounts of atomistic detail.

Of these three methodologies, MD uses the highest atomic resolution, representing each atom in the system as a finite-sized particle, whereas PNP treats solvated ions as well as water molecules as a continuum, not accounting for the atomic sizes of the ions and water, and BD treats the ions as finite-sized particles while water is represented as a dielectric continuum. Furthermore, MD simulations allow for fluctuation of the protein structure, whereas PNP and BD both treat the pore molecule as a rigid body during simulations. Thus, for calculating ion currents in protein channels, especially in narrow pores (Corry et al., 2000, Graf et al., 2000, Crozier et al., 2001 a,b), explicit atomic representation with MD is thought to be the most realistic simulation approach; however, it is also the most computationally intensive method and, until recent years, has not been practical for simulating systems of the scale of typical ion channels (often hundred(s) of thousands of atoms).

### 1.2.1 Molecular Dynamics

Molecular Dynamics (MD) is a computational method that is based in the classical regime of physics, modeling atomic motions and interactions with Newton's equations and utilizing the Born-Oppenheimer approximation that electron and nuclear motions are separable. Atoms are treated as explicit volumes and bonds as spring potentials applied at equilibrium bond distances. Modern MD techniques are an amalgam of numerous algorithms, developed over the past fifty years and designed to predict the interaction of particles in simple liquids and water (Alder and Wainwright, 1957, 1959; Rahman, 1964; Stillinger and Rahman, 1974). The first MD simulations of a protein, the bovine pancreatic trypsin inhibitor, appeared in 1977 (McCammon et al., 1977).

In MD simulations, time evolution of a set of interacting particles (atoms) is determined by integrating their equations of motion. MD utilizes classical mechanical methodology, most notably Newton's Second Law: $\vec{F}_i = m_i \vec{a}_i$ for each atom $i$ in a system of N atoms, with $m_i$ as the mass, $\vec{a}_i$ the acceleration $d^2\vec{r}_i/dt^2$ , and $\vec{F}_i$ the force acting upon the particle. This force is determined from the gradient of a potential energy function $V(\vec{R})$, $\vec{R}$ being the complete set of system coordinates (3N in all). In particular,

$$V(\vec{R}) = V_{bonded}(\vec{R}) + V_{nonbonded}(\vec{R}) \tag{1.1}$$

where:

$$V_{bonded}(\vec{R}) = \sum_{bonds,i} \frac{1}{2} k_i^b (r_i - r_i^o)^2 + \sum_{angles,i} \frac{1}{2} k_i^\theta (\theta_i - \theta_i^o)^2 + \sum_{torsions,i} k_i^\phi (1 + \cos(n_i \phi_i - \delta_i)) \tag{1.2}$$

and:

$$V_{nonbonded}(\vec{R}) = \sum_{nonbonded\ pairs(i,j)} \left\{ \varepsilon_{min}^{i,j} \left[ \left( \frac{r_{min}^{ij}}{r_{ij}} \right)^{12} - 2 \left( \frac{r_{min}^{ij}}{r_{ij}} \right)^{6} \right] + \frac{q_i q_j}{\varepsilon r_{ij}} \right\} \tag{1.3}$$

where $k_i^b$ is the bond vibrational spring constant, $r_i$ is bond length, $r_i^o$ is equilibrium bond length, $k_i^\theta$ is the angular spring constant, $\theta_i$ is bond angle, $k_i^\phi$ is the torsional spring constant, $\phi_i$ is dihedral rotational angle, $\delta_i$ is the phase constant denoting initial dihedral angle, $\varepsilon_{min}^{i,j}$ is the potential well depth, $r_{min}^{ij}$ is the distance where the potential reaches a minimum, $\varepsilon$ is dielectric constant, and $q$ is the charge on an atom.

As can be seen from equations 1.1-1.3, $V(\vec{R})$ is expressed in terms of i) bonded interactions such as bond stretching, bending, or twisting across the molecule, plus ii) nonbonded interactions such as Van der Waals forces estimated via the Lennard-Jones potential and electrostatic interactions. It is important to note here that the electrostatic contribution to the $V(\vec{R})$ expression is calculated as if the charge on each atom is a point charge at the center of mass of the atom. Delocalization of electron density, conjugation across bonds and electronic polarizability, all of which are intrinsically quantum mechanical effects, are ignored in standard MD simulation. A notable exception to this is Quantum Mechanics/Molecular Mechanics (Warshel and Karplus, 1972; Warshel and Levitt, 1976), where a small portion of the system of particular chemical interest, i.e. a reactive center, is treated using quantum mechanical methods, while the rest of the system is treated using less computationally intensive classical physics. Even with the most modern computational platforms, however, this method remains too resource-intensive to apply to chemical systems containing more than a few hundred atoms.

The kinetic energy of the system may be calculated according to the motion of the individual atoms, where for a system of N atoms, the total kinetic energy (K) is found by calculation of velocities or momenta:

$$K = \sum_{i=1}^{N} \frac{1}{2} m_i \left(\frac{d\vec{r}_i}{dt}\right)^2 = \sum_{i=1}^{N} \frac{\vec{p}_i^2}{2m_i} \tag{1.4}$$

where $m_i$ is the mass of an individual atom, $\frac{d\vec{r}_i}{dt}$ is the velocity of the atom, and $\vec{p}_i$ is its momentum.

If initial conditions and a time step increment are defined, the values for the potential and kinetic energies may be calculated as the atomic positions and velocities evolve over time. The algorithm used in MD to accomplish this is the Velocity Verlet algorithm (Swope, W.C., et al., 1982), which explicitly solves for both positions and velocities:

$$\vec{R}(t+\delta t) = \vec{R}(t) + \vec{v}(t)\delta t + \frac{1}{2}a(t)\delta t^2 \quad (1.5a)$$

$$\vec{v}(t+\delta t) = \vec{v}(t) + \frac{1}{2}[a(t) + a(t+\delta t)]\delta t \quad (1.5b)$$

At the most basic level, an MD simulation is a collection of particles in a box of consant volume surrounded by vacuum, thus being isolated and forming an NVE, or microcanonical ensemble. In accordance with the Ergodic Hypothesis (Ford, 1973), this type of MD simulation relies on the assumption that long time scales will provide enough sampling to yield time-averaged system properties that are equivalent in value to ensemble-averaged properties. Provided a given total energy, if time evolution is sufficiently extensive, it is found that the microstate population will be distributed proportional to their corresponding Boltzmann factors $e^{-\beta E}$, where $\beta = \frac{1}{k_B T}$, total energy (E) is the sum of kinetic (K) and potential (V) energies, E = K + V, $k_B$ is Boltzmann's constant, and T is temperature in Kelvin. By calculating system trajectories via the Velocity Verlet algorithm, it is possible to determine the evolving microstates and thus determine the most probable microstates, as defined by their corresponding Boltzmann factors (Rapaport, 1997). Furthermore, through kinetic sampling, an estimate of the system temperature may found be according to:

$$\langle K \rangle_{system} = \frac{3}{2} N k_B T \quad (1.6)$$

where $\langle K \rangle_{system}$ is the expectation value for the total kinetic energy of a system of N particles, assuming motion in three dimensions. This equation is easily modified for systems containing particles constrained in their motion to fewer dimensions, where according to the Equipartition Theorem,

$$\langle K \rangle_{1-D,i} = \frac{1}{2} k_B T \tag{1.7}$$

where $\langle K \rangle_{1-D,i}$ is the expectation value for kinetic energy of a single particle moving in one dimension (Atkins and dePaula, 2002).

This description of MD is limited in its real-world application – real systems may be closed from their surroundings, that is, no mass is exchanged, but energy exchange will still occur (e.g. thermal energy), as in the cases of NVT (canonical) and NPT (isothermal isobaric) ensembles. This coupling may be integrated into the MD method, which is accomplished through the Nose-Hoover (for NVT) (Nose, 1984; Hoover, 1985) and Berendsen (for NTP) (Berendsen et al., 1984) algorithms, which both use Lagrange multipliers to couple the system with a constant external value of temperature or pressure. Specifically, the Nose-Hoover algorithm rescales the kinetic energies of individual particles at each time step, with the new value chosen from a range of kinetic energies averaged around a target value for the assigned temperature. The Berendsen algorithm rescales the instantaneous pressure of the system towards a target pressure value by reassigning particle positions in order to either contract or expand the system in response to a higher or lower external pressure, respectively.

Additionally, it is possible to perform non-equilibrium molecular dynamics (NEMD) calculations, in which the system is subjected to perturbational or external forces such as pressure or an electric field, and the system response, and resultant properties, can be measured. These types of simulations are particularly valuable in the study of protein channels, where the simulation

of osmotic pressure (driving aqueous media) or of an applied voltage potential (providing a drift force to mobile ions) would be necessary to compute nonzero fluxes of media or solute through these channel structures.

One essential aspect for determining the accuracy of MD is choosing an appropriate time step – that is, to allow for Δt to accurately reflect the dynamics represented in the potential energy function. To illustrate this, one can consider the bond vibration energy term, i.e. the harmonic potential along a bond axis, as is given in the above description of the potential energy function $V(\vec{R})$. If Δt were 10 fs, then the MD time step would be longer than the period of a hydrogen bond vibration, thus making it impossible to represent the motion determined by this potential. As such, the time step must be short enough to ensure accurate computations and long enough to allow efficient computer usage. Typical time steps that are used in MD simulations are 1fs or 2fs to allow for resolution of the full range of molecular vibrations ($10^{12}$-$10^{14}$Hz) (Que, 2000).

The first MD simulation of an ion channel system was published in the early 1980's by K. R. Wilson's research group, in conjunction with the structural determination of Gramicidin A via NMR imaging, as mentioned previously. In these calculations the channel pore was filled with water molecules and different single ions were placed inside the channel (Mackay et al., 1984). The narrow pore of Gramicidin resulted in a single file of water molecules, along with the ion, forming through the channel, and it was noted that the ion translocation through the pore must be in concert with the motion of the string of water molecules. This early MD study showed the importance of excluded volume effects of both ions as well as water molecules in the simulation of narrow ion channel types. As more ion channel structures have been resolved, and computational resources have allowed for MD simulations with larger numbers of atoms, molecular dynamics has been used to simulate ion behavior in several ion channels, resulting in

calculations of energetic profiles of different ion types traversing ion channel systems (Allen et al., 2004) and diffusion constant calculations of ions within channel pores (Mamonov et al., 2006).

Even with advances in methodology and computational platforms, NEMD simulations to study electrophysiological characteristics of ion channels are still relatively few in number (Aksimentiev and Schulten, 2006; Kutzner et al., 2011; Khalili-Arghi et al., 2013). Under typical physiological conditions, single ion permeation times are generally in the 10's to 100's of nanoseconds for ion channels, and in order to achieve reliable statistics, total simulation times would be required to approach millisecond time scales. Simulations of ion channel systems (hundreds of thousands of atoms), running on supercomputing platforms, have a simulation time limitation on the microsecond time scale. Required simulation time, however, may be reduced by studying wider ion channels (with higher permeation rates), increasing ion concentration, or applying higher voltage biases across the system; alternately, some of the atoms in the channel or membrane system may be frozen in order to speed up the calculation, as discussed in chapter 2 of this document.

In recent years MD computations have successfully simulated realistic systems such as solvated proteins, nucleic acids, enzyme-substrate interactions, and lipid systems, e.g., biological membranes. There are a variety of available software packages that perform MD computations, including GROMACS (Van der Spoel et al., 2005), NAMD (Kale et. al, 1999), and AMBER (Case et al., 2005). NAMD software is particularly well-suited for larger system sizes and longer timescale simulations, as would be required to examine permeation through ion channels, as it maintains high efficiency scaling across hundreds of processors. AMBER has a well-commented and easily edited source code and is a good choice for calculations that are not possible with modules included in the other above software packages.

### 1.2.2 Poisson-Nernst-Planck Theory

Poisson-Nernst-Planck Theory utilizes the Nernst-Planck equation (Nernst, 1888; Planck 1890), which describes the diffusion of charged particles by combining Fick's Law of diffusion with Kohlrausch's electrophoretic equation. Instead of being explicitly defined as independent bodies, however, mobile charges are described as a continuum charge density that changes (i.e. diffuses) in response to an electrostatic potential gradient. Supposing that one is studying the electro-diffusion of species $i$, its ionic flux $j_i$ in a single dimension x, at steady-state, it is described by the Nernst-Planck equation as follows:

$$j_i(x) = D_i \left[ \frac{dc_i(x)}{dx} + \frac{z_i e_o}{k_B T} c_i(x) \frac{d\phi(x)}{dx} \right] \tag{1.8}$$

where $D_i$ is the diffusion constant, $c_i$ is the concentration of ion type $i$, $z_i$ is the ionic charge of ion $i$, $e_o$ is the magnitude of an electron charge, $k_B$ is Boltzmann's constant, $T$ is temperature in Kelvin, and $\phi$ is the electrostatic potential.

As a first pass at applying this equation to ion diffusion across a membrane, a few assumptions were made in order to simplify this calculation. First, the diffusion constant was taken to be a constant value across the channel; second, each ion type was taken to act independently; and third, the electrostatic potential was changed linearly across the membrane. In the 1940's, Hodgkin, Katz and Goldman, utilizing these three assumptions and the Nernst-Planck equation, were able to both estimate the electric potential across membranes as well as derive equations for ion flux (Hodgkin and Katz, 1949; Goldman, 1943).

As early ideas were developed about the structures of ion channels, it became evident that some behaviors, such as selectivity, must arise from specific charges residing within the channel structures (Hladkey and Haydon, 1972). If there is some degree of knowledge about these charges

that may be contained within the ion channel structure, the Poisson equation may also be applied to determine the electrostatic potential in one dimension, according to:

$$\frac{d}{dx}\left(\varepsilon\frac{d\phi(x)}{dx}\right) = -4\pi\left[\rho_{fixed}(x) + \sum_{i=1}^{N} z_i e_o c_i(x)\right] \tag{1.9}$$

where $\varepsilon$ is the dielectric constant of the medium, $\rho_{fixed}$ is the density of fixed charges, and $N$ is the number of ion types in solution. Solving both the Nernst-Planck and Poisson equations self-consistently for a given channel model allows for calculation of steady-state ion flux through an ion channel, also known as 1-D Poisson-Nernst-Planck (PNP) theory (deLevie et al., 1972; Levitt, 1991; Coalson and Kurnikova, 2005).

As more insight has been gained about ion channel structure, shape and charges within component residues, a more realistic 3-D PNP approach has been developed. At steady state, for each mobile ion species, the divergence of the current density at each point within the channel goes to zero in the system of mobile charges:

$$div(\vec{J}_i) = 0 \tag{1.10}$$

The Nernst-Planck equation for each of the $N$ ion species is written as:

$$0 = \vec{\nabla}\cdot D_i(\vec{R})\left[\vec{\nabla}c_i(\vec{R}) + \frac{c_i}{k_B T}(\vec{R})\vec{\nabla}V_i(\vec{R})\right]; i = 1, \ldots, N \tag{1.11}$$

where $\vec{R}$ is a 3-D position vector and $V_i$ is the total potential energy for ion type $i$, proportional to the electric potential :

$$V_i(\vec{R}) = q_i\phi(\vec{R}) \tag{1.12}$$

where $q_i$ is ionic charge ($z_i e_o$ for species $i$).

The accompanying 3-D Poisson equation is:

$$\vec{\nabla}\left(\varepsilon(\vec{R})\vec{\nabla}\phi(\vec{R})\right) = -4\pi\left[\rho_{fixed}(\vec{r}) + \sum_{i=1}^{N} q_i c_i\,(\vec{R})\right] \tag{1.13}$$

These equations are then solved using a finite difference approach whereby the mobile charge distribution, electrostatic potential, and dielectric constant are discretized onto a 3-D lattice and a real-space relaxation algorithm is applied to update lattice points based on averaging nearest neighbor values (Kurnikova, et al., 1999, A. E. Cárdenas, et al., 2000). The 3-D structure of the ion channel is mapped out in the simulation box, allowing for the pore to have dimensions determined by solvent accessible surfaces, with atomic charges assigned according to residue type. The channel structure remains fixed during PNP simulations, and so it is desirable to first equilibrate the ion channel structure using MD before performing PNP calculations.

### 1.2.3 Brownian Dynamics

Brownian dynamics (BD) differs from PNP in that ions are treated explicitly, while the solvent is represented as a continuum with an assigned dielectric constant and friction coefficient used to determine the diffusion constant values of the mobile ions (Ermak and McCammon, 1978). As with PNP, the channel structure is similarly mapped out in the simulation box and remains fixed during the simulation, and the electric potential for ions at any given position within the simulation may be calculated using Poisson's law. The Langevin equation is used to describe the motion of ions in BD (Chung et al., 1998) according to:

$$m_i \frac{d^2\vec{r_i}(t)}{dt^2} = \vec{F}_{sys} - \gamma_i \frac{d\vec{r_i}(t)}{dt} + \vec{R}(t) \quad (1.14)$$

where $m_i$ is the mass of ion type $i$, $\vec{r_i}$ is the 3-D position of the ion, $\vec{F}_{sys}$is the systematic force acting on the ion resulting from Coulomb interactions with other mobile ions as well as charges within the channel structure, and any externally applied electric field (to simulate voltage bias across the membrane), $\gamma_i$is the friction coefficient, and $\vec{R}(t)$ is the random force that represents collisions with solvent molecules.

One difficulty with Brownian Dynamics is that determining electrostatic energy at each time step may require intensive calculations due to induced charges at the dielectric boundaries between the solvent, protein, and membrane regions. However, a methodology using an efficient empirical method to accurately calculate ion-ion electrostatic interactions in these types of systems (Cheng and Coalson, 2005) has been shown to effectively address this for BD simulations of ion channels. This method utilizes a dynamic lattice Monte Carlo (DLMC) algorithm (Graf et al., 2000, 2004) to generate kinetics equivalent to the Brownian Motion in the high-friction limit. In this approach, configurations of mobile ions within the simulation system are generated by random changes of the ion positions, and so, for a system containing *N* ions, one Monte Carlo cycle consists of *N* steps. At each step, one ion *k* is randomly chosen to move a single lattice point in one direction (either positive or negative in *x*, *y*, or *z*). A random number (*Rand*) in the interval [0,1] is then generated and this move is accepted if $Rand < exp(-\beta \Delta W)$, where $\beta=(k_B T)^{-1}$ and $\Delta W$ is the energy change between the two configurations:

$$\Delta W = W_k^{new} - W_k^{old} \quad (1.15)$$

where:

$$W_k = q_k \phi^{stat} + q_k^2 \phi_k^{self} + \sum_{j \neq k} \frac{q_k q_j}{\varepsilon_w} \phi^{coul}(r_{kj}) + \sum_{j \neq k} q_k q_j \phi_{kj}^{diel} \quad (1.16)$$

where $q_k\phi^{stat}$ is the potential energy of ion k resulting from the electrostatic interaction of the the charge of the ion $q_k$ and it surrounding electric potential $\phi^{stat}$ resulting from fixed charges as well as any external potential. $\phi^{stat}$ is found by solving Poisson's equation:

$$\nabla \cdot [\varepsilon \nabla \phi^{stat}] = -4\pi\rho \tag{1.17}$$

based on the complete (spatially dependent) dielectric constant profile and the specified boundary potential, with $\rho$ being the charge density due to the permanent charges and dipoles in the protein and membrane, $q_k^2\phi_k^{self}$ is the dielectric self-energy that accounts for the image potential due to the surface charge induced on dielectric boundaries by ion k, $\sum_{j\neq k} \frac{q_k q_j}{\varepsilon_w} \phi^{coul}(r_{kj})$ represents Coulombic interactions between pairs of ions in an environment characterized by the (uniform) water dielectric constant $\varepsilon_w$, and $\sum_{j\neq k} q_k q_j \phi_{kj}^{diel}$ corresponds to the image potential experienced by ion k due to the surface charge induced by ion j.

Comparatively larger time steps are possible with BD when compared to MD simulations, as neither bond vibrations within the fixed protein structure nor motion of solvent molecules need to be resolved in this method. Typical time steps used in BD simulations are up to 1ps, large enough to allow for more computationally efficient calculation of permeation rates, particularly when compared to MD.

### 1.2.4 Comparison of Methods

Of the three methodologies presented here, PNP is the most computationally efficient, followed by BD and then NEMD; this order reflects the increasing atomistic detail of the system. PNP has been tested for channels of various radii and has been found to be accurate for wider channels, but application to more narrow ion channels, particularly those that approach a single

file of waters and ions through the pore, encounters difficulties due to its mean-field approach (Corry et al., 2000; Im and Roux, 2002). In particular, ion-ion interactions are represented on the mean field level; thus physical interactions between ions such as excluded volume effects are not accounted for. This would be of particular concern in channels that contain specific binding sites for ions, and the kinetics of one ion replacing another at a particular binding site would not be accounted for in PNP (Miloshevsky and Jordan, 2004), while the atomistic representations of mobile charge in BD and NEMD successfully address this issue. Futhermore, since ions are infinitely small in PNP, the change in an ion's solvation energy upon moving from a high dielectric bath to a narrow channel with low dielectric (referred to as dielectric self energy, or DSE) is not accurately described in standard PNP theory. While ions are able to maintain their solvation shells upon entering wide channels and, as such, this effect is significantly reduced in wide channels, the DSE for ions to enter narrow channels has been calculated as high as 15 $k_BT$ (Graf et al., 2000) and should not be neglected.

Both PNP as well as BD represent solvent as a continuum and so neither excluded volume effects of water molecules nor proper treatment of hydration shells are accounted for in these approaches. These two factors become more prominent as solvated ions are confined to smaller volumes, as would be the case in narrow ion channels. Furthermore, both the dielectric constant as well as the diffusion constant values for mobile ions within ion channel pores have not yet been experimentally measured and must be estimated for these methods. Computational methodologies for determining internal diffusion constants for ion channels have been developed (Mamonov et al., 2006) and will be utilized in this thesis document. As for the ion channel structure, neither PNP nor BD simulate motion of the component residues, which may be an important aspect in I-V calculations as ion channel proteins may undergo natural breathing motions of the overall

structure (Noskov and Roux, 2004) and fluctuations of residues that line the pore may have an effect on the pore size as well as interactions with mobile charges passing through the channel (Mamonov et al., 2003). A fully atomistic approach such as NEMD can account for these issues, although at greatly increased computational expense.

# 2.0 SIMULATIONS AND POINT MUTATION STUDIES OF THE BIOLOGICAL ION CHANNEL ALPHA-HEMOLYSIN

## 2.1 INTRODUCTION

The biological ion channel alpha-hemolysin (α-HL) is secreted by the bacterium *Staphylococcus aureus* as an exotoxin that disrupts the membranes of target cells via channel formation. In addition to targeting red blood cells, the toxin is also known to cause lysis of nucleated cells such as monocytes, lymphocytes, erythrocytes, and endothelial cells (Gouaux, 1994). *S. aureus* uses this channel as a virulence factor to colonize and cause disease in various host organisms and thus is responsible for a variety of afflictions from superficial skin infections such as boils to serious disorders like endocarditis and Methicillin-resistant *Staphylococcus aureus* (MRSA) infections.

Mechanistically, α-HL is secreted by *S. aureus* as seven water-soluble monomers that bind to lipid membranes and self-assemble into a heptameric channel (Figure 2.1) (Braha et al., 1997; Gouaux, 1998). Its open-state crystallographic structure has been resolved (Song, et al., 1996) and its conduction properties have been studied in detail, both experimentally (Menestrina, 1986; Bezrukov and Kasianowicz, 1993; Kasianowicz and Bezrukov, 1995, Gu et al., 2001, Misakian and Kasianowicz, 2003) as well as using calculations (Noskov et al., 2004, Aksimentiev and Schulten, 2005, O'Keeffe et al., 2007); findings indicate that the native structure is slightly selective for anions over cations.

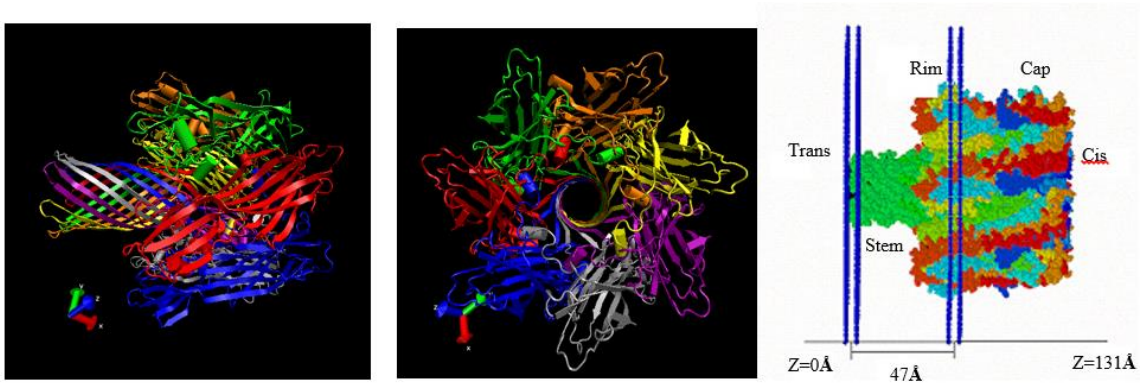


**Figure 2.1**: The left and center figures show two views of the alpha-hemolysin channel. The overall dimensions are approx. 80Å by 100Å while the pore dimensions are ~15Å in dia. by 80Å in length. The right figure schematically depicts α-HL positioned in a lipid bilayer. The three domains of the structure are labeled as stem, rim, and cap; The cis end of the pore is on the intracellular side of the membrane, while the trans end of the channel extends into the extracellular matrix (Kowallis and Coalson, in preparation(a)). [The two images w/ black background were rendered using VMD (developed by the Theoretical Biophysics Group in the Beckman Institute for Advanced Science and Technology at the University of Illinois at Urbana-Champaign) (Humphrey et al., 1996).]

There has been a variety of experimental interests in α-HL: for use as a biosensor (Gu et al., 1999), for controlled delivery across a membrane (Bayley, 1995), and for polynucleotide characterization (Kasianowicz et al. 1996). Thus simulations that analyze and predict behavior of this channel may be useful for its future applications. Considering these many potential uses of α-HL, understanding, and potentially being able to alter, the permeant properties of this channel remains an area of interest. For example, recent studies have investigated the covalent bonding of a prosthetic molecule, β-cyclodextrin, to the pore lumen and the subsequent effects on the selectivity and current-voltage (I-V) characteristics of α-HL (Egwolf et al., 2010, Luo et al., 2010, Toghraee et al., 2010).

In this study we performed a series of non-equilibrium molecular dynamics (NEMD) simulations to monitor the behavior of ions as they traverse α-HL, with simulation times sufficient to generate I-V data, comparing the results to experimental data (Misakian and Kasianowicz, 2003) as well as to results calculated using two other computational methods, Poisson-Nernst-Planck (PNP) (Chen and Eisenberg, 1993; Kurnikova et al., 1999) and Brownian Dynamics (BD) (Chung

et al., 1998, Graf et al., 2000, Cheng et al., 2005). In order to conserve computational resources, we utilized a novel NEMD setup where the system consists of an artificial membrane and partially frozen protein structure (described below).

For calculating ion currents in protein channels, explicit atomic representation with MD has been claimed to provide the most realistic simulation approach (Corry et al., 2000, Graph et al., 2000, Aksimentiev and Schulten, 2005). Since all atoms in a system are represented in MD, it is also the most computationally intensive method and, until recent years, has not been practical. PNP and BD are much more computationally efficient since the protein structure remains fixed during these calculations while PNP treats solvated ions as well as water molecules as a continuum and BD treats the ions as finite-sized particles and treats the water as a dielectric continuum. It has been established that both PNP (Kurnikova et al., 1999, Mamonov et al., 2003) as well as BD (Graf et al., 2000, Noskov et al., 2004; Cheng et al., 2005) produce qualitatively and (reasonably) quantitatively accurate results for studying I-V characteristics of ion channels. However, current estimations are expected to be artificially high when compared to experimental observations when using either of these methods since neither BD nor PNP account for excluded effects of solvent molecules, and PNP additionally lacks treatment of dynamical ion-ion correlation. The present study includes calculated I-V properties of $\alpha$-HL using all three of the above simulation methods, thereby enabling us to compare and contrast their quantitative as well as qualitative accuracies when compared to experimental data.

In calculations of ion flux through a channel, a factor to consider is the accuracy of the calculated free energy required for an ion to traverse the channel. This energy is artificially high in narrow channels, e.g. Gramicidin A (pore dia. ~4Å), likely due to inaccuracies in extant atomic-level force fields, including absence of delocalization/polarization across bonds and atoms

(Mamonov et al., 2003). Additionally, charge shielding in a narrow pore environment is systematically overestimated in PNP, where mobile charge is confined to a smaller volume and thus always in close proximity to the channel structure (Corry et al., 2000). Effects of these inaccuracies are largely diminished in systems that consist of a wider pore, particularly where the channel radius (α-HL has a minimum pore radius of ~7.5Å) approaches twice the Debye length (~3.0Å in 1.0M monovalent solution at 298K) (Corry et al., 2000), and thus will not be taken into account when comparing results from our different computational approaches.

In order to reduce the computational load for our NEMD simulation system, we chose to use a layer of uncharged Lennard-Jones spheres in place of a fully atomistic lipid bilayer. Further, we froze a portion of the channel structure (the regions closest to the membrane) while leaving no restraints on the residues near the pore-solvent interface. Clearly the most realistic simulation setup would have the protein embedded in a membrane with all atoms, both in the protein and bilayer, free to move. However, especially in the case of a large protein such as α-HL, large-scale motions, e.g. conformation changes and breathing, which may result in changes in the overall shape of the channel pore and thus alter permeant properties (Aksimentiev and Schulten, 2005), would not be accounted for on the time scale (ca. 10 ns) of these simulations. The speedup gained in our calculations by adding these restraints to our system was approximately 50% compared to test calculations with the channel situated in an atomistic membrane, allowing all atoms to be fully mobile.

Previous work by several authors (Allen et al., 2004; Chui et al., 1993, Mamonov et al., 2006) has shown that there is a reduction in the diffusion constant (D) for ions in solution upon their entrance into an ion channel, due to the additional confinement of these mobile ions by the channel pore structure, i.e. the pore radius, and also dependent upon the channel properties,

including charges in the protein structure. For our BD and PNP calculations the diffusion constants of ions are assigned as input parameters and so it was necessary to calculate the effective diffusion constants of ions as they traverse the channel interior. We have calculated D for ions using two different methodologies, Mean Square Displacement (MSD) as well as Force Autocorrelation Function (FACF), to see if a reduction is also apparent in α-HL. The results of these calculations of D inside the channel were used for the diffusion constant value in both our PNP and BD calculations of α-HL.

Based on the results of the simulations we were able to investigate and identify dynamical properties of our simulation system that are responsible for the channel's ion permeation characteristics. Concentration profiles were calculated from NEMD and BD trajectories, allowing us to identify an explicit region and, in particular, a single residue in the pore that accounts for both current rectification as well as ion selectivity for this channel. This region, which is one of the narrowest parts of the channel, creates a bottleneck for the flow of permeating ions and shows a selectivity favoring anions over cations. While this particular region has been suggested as the source of selectivity in the α-HL channel (Noskov et al., 2004; Aksimentiev and Schulten, 2005), to our knowledge no calculations have been performed to study effects of residue mutations, and specifically a mutation at this site that changes both the current rectification as well as the selectivity from anionic to cationic.

The corresponding residue number in the α-HL structure that provides the positive electrostatic charge (and thus the anionic selectivity) as well as the constriction in pore radius at this location is lysine 147 (Figure 2.2). The lys147 residues alternate with glutamate 111 around this region of the pore, with the side chains of lys147 extending further towards the center of the pore than those of glu111. This results in permeating ions passing through an overall positive

electrostatic potential in this region of the pore, favoring the passage of negatively charged ions. We propose that a mutation of the lys147 residue to a neutral residue with a shorter side chain, such as serine, would make this region strongly negatively charged due to the remaining glu111 residues and thus selective for positively charged ions.

Additionally, this channel exhibits current rectification, likely as a result of asymmetry in pore radius at opposite ends of the stem region. As it is the R-group chain lengths of lys147 that account for the physical constriction of the pore diameter in this region (approximately 15Å), we further propose that a point mutation of lys147 to serine would effectively widen the pore at this location (to approximately 19Å) and therefore result in a change in current rectification. By comparison, the pore diameter at the opposite end of the stem region is approximately 17Å.

Using PNP as well as BD we have tested the resultant changes in the permeant properties of the system, including a switch of the current rectification properties in addition to a change in the selectivity to favor cation permeation, which we found to be especially evident at low concentrations. We also tested the effect this mutation would have on the reversal potential of the system. This is the required voltage bias that must be applied in order for the net electrical current to go to zero when an ion channel system has different salt concentrations on either side of the membrane. It serves as a useful tool for describing selectivity for a specific ion type. For α-HL with asymmetric bathing solution concentrations (1.0M and 0.1M), PNP calculations were carried out for the native and mutated channel structures. The single point mutation we identified resulted in a marked shift in the reversal potential for this system.

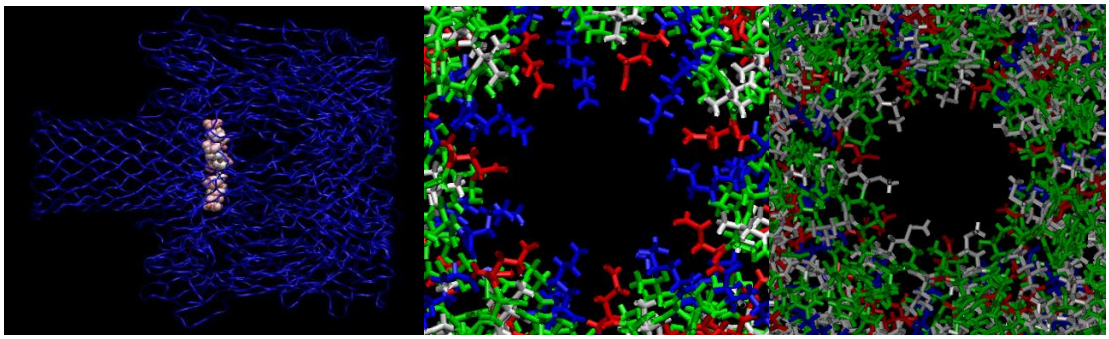

**Figure 2.2**: At left, lys147 is shown in pink. Note that it is found in the narrowest region of the channel - the entrance to the stem region. At center, the lys147 (blue) residues alternate with glu111 (red) to form a ring of salt bridges at the narrowest part of the α-HL channel. At right, all seven lys147 have been mutated to serines, The channel is both wider now as well as net negatively charged at this location due to the remaining glu111 residues.

## 2.2 METHODS

### 2.2.1 Modeling

The crystal structure of α-HL was obtained from the Research Collaboratory for Structural Bioinformatics Data Bank (PDB) (Bernstein et al., 1977), PDB entry code 7AHL (Song et al., 1996). Missing hydrogen atoms, which are not resolved in x-ray crystallographic methods, were added to the structure using XPLOR (Brünger, 1992), water molecules that were resolved as part of the x-ray structure removed, and the channel structure was repositioned so that the pore axis was oriented normal to the x-y plane (the plane of the bilayer), which is the proposed position of α-HL in the bilayer (Song et al., 1996). This positioning of the channel structure, however, has not been verified to remain perpendicular to the plane of the bilayer over long trajectories, and the possible effects of this on the channel's I-V properties cannot be known with certainty. Any such movements of the pore are not accounted for in our PNP or BD calculations, and so are a potential source for error.

In place of using an atomistic membrane, we chose to use uncharged "dummy" atoms, or Lennard-Jones spheres, to act as a barrier between external and internal bathing solutions. As a first step in creating this artificial membrane, the structure was placed in a water box of dimensions 110Åx110Åx92Å using the program SOLVATE (Grubmüller, 1996), with these dimensions chosen as to completely encompass the structure along the sides, yet leaving approx. 5Å of the channel extending beyond the solvation box in either z direction. This allowed for the channel structure to electrostatically interact with ions in solution on either side of this artificial membrane. Waters were then cut from the pore cylinder and the solvation box itself was cut normal to the xy plane into a hexagonal shape of dimensions 96Å x 96Å x96Å – just wide enough to encompass

the entire heptameric protein structure. The last step was to then select all of the waters that remained, all of which surrounded the external sides of the α-HL structure, and first remove their hydrogens and then strip their charges, thus effectively converting them into Lennard-Jones (L-J) spheres. These L-J spheres were frozen during the simulations, thus requiring solvent and mobile ions to pass through the pore of α-HL in order to traverse from one side of the channel structure to the other. The effects of using this artificial membrane on the channel motion as well as overall accuracy of the simulation are discussed in more detail below.

The system was then again solvated in a water box of dimensions 110Åx110Åx 140Å, so that the water would extend approximately 20Å beyond both ends of the channel structure. This water box was then cut hexagonally in the same fashion as before, except this time water molecules were not removed from inside the pore cylinder. Sodium and chloride ions were placed into the solution in order to bring the ionic concentration to 1.0M NaCl, with the qualification that seven more Cl- than Na+ ions were added (297 Cl- + 290 Na+ = 587 total ions) in order to bring the overall system to a charge neutral state (α-HL has a +7 overall charge as a sum of charges in its crystal structure). The overall system size, including the pore structure, dummy atoms, ions and water molecules totaled 91,593 atoms (Figure 2.3).

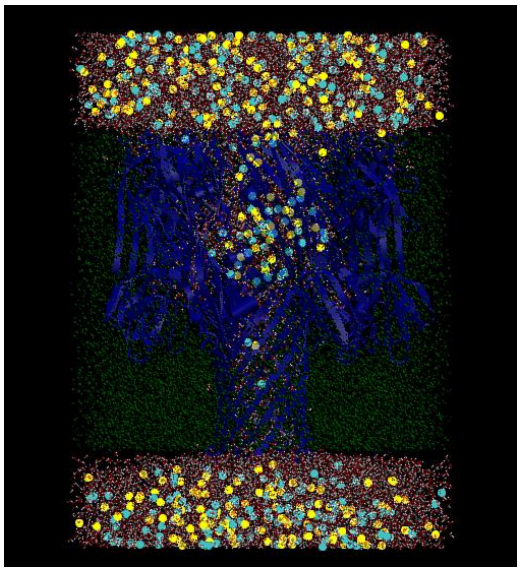

**Figure 2.3:** The NEMD simulation system, where the protein is shown in dark blue, Cl- anions are light blue spheres, Na+ cations are yellow spheres, Waters are red/white, Lennard-Jones spheres are shown in green.

### 2.2.2 Equilibration

After the dummy layer formation and solvation, the system was equilibrated as an NPT ensemble at 298K with an applied pressure of 1 atmosphere along the z-axis. For this process, both the channel structure and the L-J spheres were held fixed, periodic boundary conditions were disabled, and the time step was set to 2fs. The system was allowed to relax in the z-dimension while the x-y area remained fixed (the cell volume remained fixed during NEMD trajectories (production runs) used to calculate ion flux).

After 1ns of equilibration it was noted that water molecules inside the pore were migrating into spaces along the surface of channel structure in order to occupy spaces that were not effectively filled by SOLVATE, leaving empty spaces inside the channel. Instead of waiting for waters to migrate in to fill these spaces from outside the channel, the pore area was resolvated and equilibrated for another 2ns, after which no empty spaces appeared in the pore. After equilibration

the system dimensions were 96Å by 96Å by 128Å (note the reduction in the z- coordinate from 140Å – a result of the NTP equilibration).

### 2.2.3 NEMD Calculations

The program NAMD (Kale et al., 1999) and the CHARMM27 parameter set (Schlenkrich et al., 1996; MacKerell Jr. et al., 1998; Feller and MacKerell, 2000) were used for all simulations. Full periodic boundary conditions were imposed using hexagonal symmetry in the x-y plane and a wraparound in the z-dimension. The particle mesh Ewald (PME) method (Darden et al., 1993) was used for computation of electrostatic forces without truncation. The Berendsen and Nose-Hoover algorithms were used to maintain a constant pressure of 1.0 atm (during equilibration) and a constant temperature of 298 K, respectively (Feller et al., 1995). Use of PME electrostatics requires periodic boundary conditions (PBCs), including in the channel axis direction. In this work we considered only symmetric bathing solutions of 1.0M NaCl (i.e., 1.0 M NaCl in both the intracellular and extracellular compartments) in our NEMD simulations, as symmetric bathing solutions are naturally consistent with PBCs. Methods have been recently developed to allow use of asymmetric bath concentrations in NEMD ion permeation calculations (Kutzner et al., 2011, Khalili-Arghi et al., 2013), which we may apply in future work.

For the generation of current-voltage curves the system temperature was fixed at 298K and the dimensions of the cell were set to constant values in all dimensions, making it an NVT ensemble. Furthermore, the time step for production runs was 2fs for the first 4ns of simulation and then, in order to speed up simulation time, was changed to 3fs in order to test if the simulation system would remain stable (which it did). Simulation of an external voltage was accomplished by applying a uniform electric field ($\vec{E}$) perpendicular to the membrane, which acts on charged

particles throughout the system, and the resulting applied membrane potential (*V)* is equal to the applied electric field times the length of the periodic cell in the direction perpendicular to the membrane. This voltage was applied via an embedded function in NAMD, called eField, in which the required voltage bias was converted to units of calories/electron charge ($e_o$) and divided by the overall length of the simulation system in the z-direction (128Å) since the voltage is applied across the membrane, thus yielding an electric field in units of cal./$e_o$-Å (a potential of +200 mV across the 128Å simulation system corresponds to an electric field of +.036 cal./$e_o$-Å). A particle in the system with charge q (in units of $e_o$) would undergo a force according to $\vec{F} = q\vec{E}$, where this force would be acting parallel to the electric field lines (perpendicular to the membrane) and added to the forces acting on these particles (described in section **1.2**) at each time step. Application of periodic boundaries allowed for ions to recycle instead of simply collecting at opposite sides of the system, as would be the result with an applied voltage and no periodic boundary conditions. The eField function additionally allows the user to select which charged particles will interact with the electric field, so components of the system that are held immobile during the simulation will not be subjected to these interactions.

During initial NEMD simulations in our development grant at PSC the entire protein structure (~23,000 atoms) was held frozen to minimize the computation time needed to produce results that tested the accuracy and applicability of this approach; we found that this produced unphysical results, with ions actually migrating into the protein structure at different places (Figure 2.4). To rectify this, we subsequently allowed all residues at the protein-solvent interface to move freely while keeping the rest of the α-HL structure frozen (Figure 2.5)

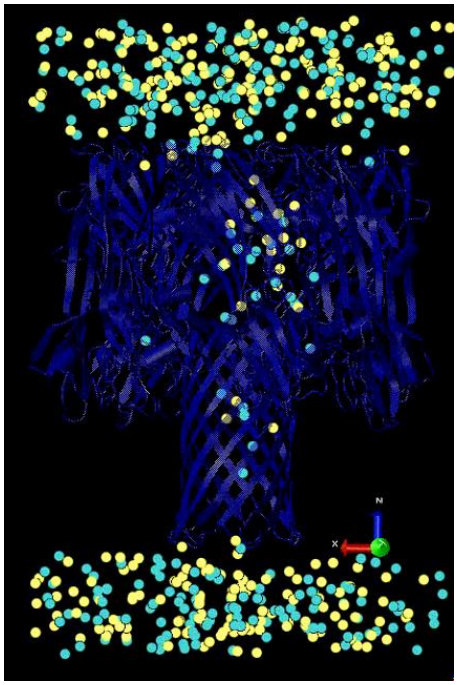

**Figure 2.4**: An example of ions migrating into the channel structure of α-HL when residues at the protein- solvent interface are not free to move. Chlorine anions are blue spheres and Sodium cations are yellow spheres. Specifically note the Na+ cation in the right part of the stem region as well as the Cl- anions in the rim region.

Freeing residues at the protein surface to allow for their motion during production runs serves to increase the realism of the model in a number of ways. First, the motion of the residues at the pore-lining changes the size and shape of the pore itself. Also, the amino acids found at the pore surface would have the highest impact in altering the electrostatic potential inside of the pore. Finally, most of the charged and polar groups in the protein structure are found at the surface of the protein, especially the pore. As such, these are the residues whose motion has the largest influence on permeation due to their effect on pore volume as well as their effect on electrostatic potentials inside the channel. Furthermore, large-scale motions of the protein, e.g. breathing, will not be observed on the time scale of our simulations (ca. 10ns) (Aksimentiev and Schulten, 2005), and so using the average overall shape of the channel (that being the overall shape of the crystal structure) should be sufficient for our calculations. Freeing these residues near the pore surface allowed the ions to move smoothly through the channel, since the fluctuations of these amino acids

eliminated the gaps in the frozen pore surface that had allowed ions to become lodged in the α-HL structure.

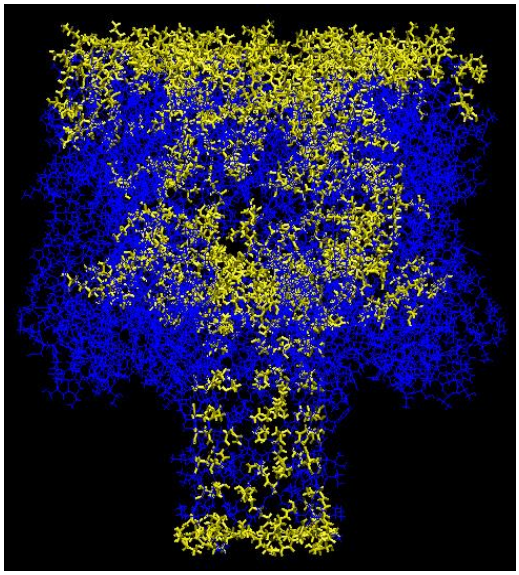

**Figure 2.5:** The residues at the protein-solvent interface that were selected to move during our production runs are highlighted in yellow.

By keeping the majority of the channel structure frozen during NEMD simulations, atomic fluctuations for most of this molecule were not considered and the interatomic forces within the fixed portions of the α-HL structure were not calculated, thus reducing the required computation power by approximately half compared to benchmark calculations using a fully mobile pore structure and mobile POPC membrane. Using our simulation setup, the only atoms that affect the computation are the solvent and the mobile ions, which consists of approximately 50,000 atoms, greater than 49,000 of which represent water molecules, plus the non-frozen residues at the protein-solvent interface (~8500 additional atoms). Calculations were performed for a concentration of 1M NaCl and applied voltages of 0mV, +/-200mV and +/-400 mV in order to determine ion occupancies through the channel both at equilibrium as well as with an applied voltage. The approximate total simulation times for each of the various voltage biases are listed on Table 2.1.

| voltage bias (mV) | permeation events | Approximate simulation time (s) |
|---|---|---|
| -400 | 29 | 1.17E-08 |
| -300 | 29 | 1.46E-08 |
| -250 | 29 | 1.75E-08 |
| -200 | 25 | 1.92E-08 |
| -150 | 19 | 1.98E-08 |
| -100 | 12 | 2.44E-08 |
| 0 | 0 | 1.20E-08 |
| 100 | 11 | 2.52E-08 |
| 150 | 18 | 1.98E-08 |
| 200 | 26 | 2.01E-08 |
| 250 | 27 | 1.76E-08 |
| 300 | 26 | 1.53E-08 |
| 400 | 26 | 1.21E-08 |

**Table 2.1**: Numbers of permeation events at each voltage bias for our simulations.

### 2.2.4 PNP and BD Calculations

PNP and BD calculations were performed using software that was developed in the Coalson group and has been explained in detail in section **1.2** as well as in previous publications from the Coalson Group (Kurnikova et al., 1999; Graf et al., 2000, 2004). The grid spacing for the PNP calculations was 1.2 grid points/Å and the grid size was 145×145×205. These same dimensions were used for our BD simulations and the same grid size was used for the solution of the Poisson Equation. This insured that the entire crystal structure was contained within the simulation boxes, with room for bathing solutions at either end of the channel. We used pdf and psf files, generated using VMD from the crystal structure of α-HL, as inputs for the structure and charge files in both PNP and BD. In our PNP calculations we used a probe radius of 1.4 Å (the radius of a water molecule), which determines the dielectric boundary between the protein and mobile charge continuum. For the PNP calculations with asymmetric bath concentrations, the bath on the stem side of the protein as

well as inside the channel was set at 0.10M concentration, while the bath concentration on the cap side was set at 1.0M.

### 2.2.5 Hardware Platforms

Our NEMD calculations were carried out using clusters at the Pittsburgh Supercomputing Center, including the Lemieux cluster and its replacement, the Bigben cluster. Additionally, we performed MD equilibrations as well as PNP and BD calculations on our local 17-node cluster as well as on the Markov cluster at the Center for Macromolecular Simulations (CMMS) at the University of Pittsburgh.

### 2.2.6 NEMD Analysis

All NEMD output files were analyzed using the program Visual Molecular Dynamics (VMD, Humphrey et al., 1996). We calculated the concentration profiles by first finding the number of ions present at steady state in slices of thickness 2Å along the z-axis of the entire length of the α-HL pore. Then the concentration in a given slice $i$ for ion of type $a$ is given by:

$$c_{i,a} = \frac{\#\ atoms\ of\ type\ a}{V \times n_t} \tag{2.1}$$

i.e. the sum of ions in that slice over the entire trajectory divided by the product of the slice volume (V) times the number of time steps ($n_t$) in the trajectory.

### 2.2.7 Diffusion Constant Calculations

The average diffusion constants for each ion type, both inside and outside of the pore, were determined by two different methods, both described in earlier work in the Coalson Group (Mamonov et al., 2006). The first method finds the diffusion constants of the ions by calculating their mean square deviation (MSD), or $\langle r^2 \rangle$, over a trajectory, plotting the MSD versus time, and taking the accumulated slope of this plot to yield D according to $\langle r^2(t) \rangle = 6Dt$ (Figure 2.8), the equation for diffusion in three dimensions in bulk solution (Einstein, 1905), and $\langle {r_z}^2(t) \rangle = 2Dt$ for displacement in the z-dimension as the ions diffuse through the channel cylinder. The cutoffs for delimiting internal D values were at -48Å at +2Å along the z-coordinate of the system, which correspond to the ends of the narrow part of the α-HL structure.

The second method, using the force autocorrelation function (FACF) methodology, is based on the Generalized Langevin Equation (McQuarrie, 1976):

$$m\frac{dv(t)}{dt} = F^{sys} - \int_0^t M(t-\tau)v(\tau)d\tau + R(t) \qquad (2.2)$$

where we consider only the z-component of the motion of the ion (along the channel axis). Here $m$ is the ion's mass, $F^{sys}$ is the systematic force, $R(t)$ is the random force acting on the ion and $M(t)$ is the appropriate memory function. According to the second Fluctuation Dissipation Theorem, the memory function is related to the random force autocorrelation function (Kubo, 1966) according to:

$$M(t) = \frac{1}{k_B T}\langle R(0)R(t) \rangle \qquad (2.3)$$

So, if the random force autocorrelation function is known for the Brownian particle in question, one can use Einstein's relation $D = \frac{k_B T}{\gamma}$ and the connection between friction constant and memory function $\gamma = \int_0^\infty M(t)dt$ to find a relation between D and the FACF:

$$D = \frac{(k_B T)^2}{\int_0^\infty \langle R(0)R(t)\rangle dt} \tag{2.4}$$

Specifically, for our calculations, bulk values for the ions were found by placing an ion in a box of 1077 water molecules, and evaluating a 10ns trajectory with the ion fixed. A plot of FACF vs. time was then made; evaluation of the integral of this plot followed by the dividing of $(k_B T)^2$ (in $kcal^2/mol^2*Å^2$) by this value yields a value for D. This calculation was then repeated, placing a single ion into the narrow (stem) region of the a-HL channel (we sampled three separate locations in the stem region).

### 2.2.8 Mutation of lys147 and modeling

In the native structure of α-HL, lys147 and glu111 alternate to form a ring of salt bridges around the pore at the inner end of the stem region in each of the seven subunits. There is one lys147 and one glu111 per subunit, forming the narrowest region of the channel. We tested two possible point mutations at residue 147: the first was a mutation of lys147 to glutamate and the second was a mutation of lys147 to serine. We generated the pdb and psf files of the mutated α-HL structures using VMD, and tested their stability by inserting the structure in a POPC membrane, solvating, and adding ions to produce a simulation box of dimensions 140×140×150Å and then ran 3000 minimization steps. We then equilibrated the structure as an NTP ensemble at 298K and 1.0Atm pressure applied in the z-dimension, with the first 1ns of the simulation keeping the alpha carbons of the protein restrained and then in the following 2.5ns allowing the entire

protein free to move. We checked the root mean-square deviation value of the alpha carbons from their initial positions throughout the equilibration and concluded that the structure was stable if the deviation remained at a consistent value under 2.0Å after the first ns of unconstrained equilibration. The structure with lys147 mutated to glu did not retain its structural integrity, whereas the structure with lys147 mutated to serine did, and so the structure files from these equilibration runs were used as inputs for I-V calculations using both BD as well as PNP.

## 2.3 RESULTS AND DISCUSSION

### 2.3.1 Permeation Data

From the current-voltage data we collected in our simulations, we found that NEMD, BD, and PNP results are qualitatively similar to experimental data for the wild-type structure (Figure 2.6). One prominent feature of these I-V curves is that all methods show current rectification in the direction observed experimentally, with higher current observed at negative voltages (Misakian and Kasianowicz, 2003). Additionally, results from all methods showed that there is a slight selectivity for permeation of anions over cations at 1.0M concentrations, occurring in approximately a 1.4$Cl^-$:1$Na^+$ ratio throughout our calculations.

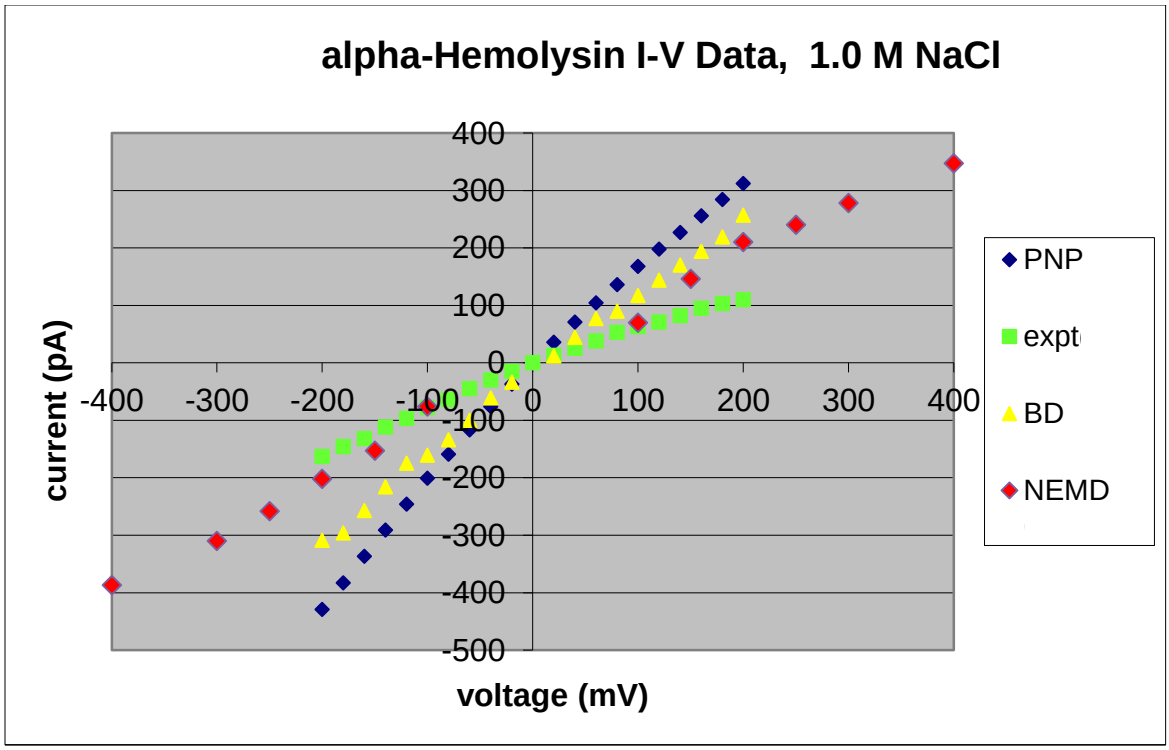


**Figure 2.6:** A graph of ion permeation data from NEMD, BD, PNP and experimental (Misakian and Kasianowicz, 2003) results for α-HL. All calculations were done at neutral pH.

Quantitatively, both PNP and BD over-estimate the flow of ion current through α-HL, although not in a manner dissimilar from other computational studies using these methods (Corry et al, 2000). Results from NEMD calculations also appear to predict somewhat higher currents as well, although these are more closely aligned with experimental data. It has been noted previously (Im and Roux, 2002, Choudhary et al., 2010) that PNP permeation data are systematically higher than what is observed in experimental studies, often by as much as a factor of two, and our I-V data for the native structure compares well previous computational studies (Noskov et al., 2004). Furthermore, it should be noted that there is some amount of variation in published experimental I-V data collected for this channel (Miles et al., 2002; Gu and Bayley, 2000; Menestrina, 1986), with the Gu and Bayley, 2000 and Menestrina, 1986 papers reporting currents at +40mV that differ approximately 40% from one another. As such, it is perhaps not surprising to find some discrepancy when comparing calculated I-V data to experimental results for this system.

An additional factor to consider for this system may be that, since the channel structure is held in an open state for the duration of all calculations, we are not able to entirely dismiss changes in current arising from changes in the overall pore shape. Furthermore, electrostatic contributions from the bilayer, as well as the position of the bilayer along the channel z-axis, and possible effects of this positioning, are not accounted for in our calculations. Some of these issues could be more carefully assessed by performing longer time-scale MD trajectories using an atomistic membrane and allowing the entire channel to move freely (Aksimentiev and Schulten, 2005).

As is stated above, it has been shown that PNP and BD provide qualitatively accurate results with respect to experimental data. Additionally, BD and PNP consistently produce results that are both qualitatively and (semi-)quantitatively similar to each other. Considering this, as well

as that most of the remaining calculations are done in order to study primarily qualitative aspects of the α-HL system, additional I-V data for this system were calculated using only BD and PNP.

### 2.3.2 Concentration Profiles

Steady-state ion concentration profiles provide a helpful tool in ion channel study since they give insight into the location of binding sites for ions within the pore (indicated by high concentrations, relative to the rest of the channel) as well as narrow or more selective pore regions (characterized by lower relative concentrations). Such profiles were calculated at every voltage bias for each ion type as we completed our production runs. We show in Figure 2.7a a profile for +200mV from our preliminary calculations (with the entire pore structure frozen) and, from our calculations with the martially mobile structure, profiles for voltage biases of +200mV and +/-400 mV.

Important features of these profiles include that there is a more continuous change in concentrations for the profiles that represent simulations where the pore-lining residues are not frozen as compared to the profile where the entire pore structure is frozen. This can be attributed to the fact that, due to the fluctuations of these residues, ions do not get stuck in frozen regions of the pore. This stands in contrast to earlier simulations in which the entire pore structure was fixed during simulations, where ions were actually able to penetrate into the channel structure itself (Figure 2.7b).

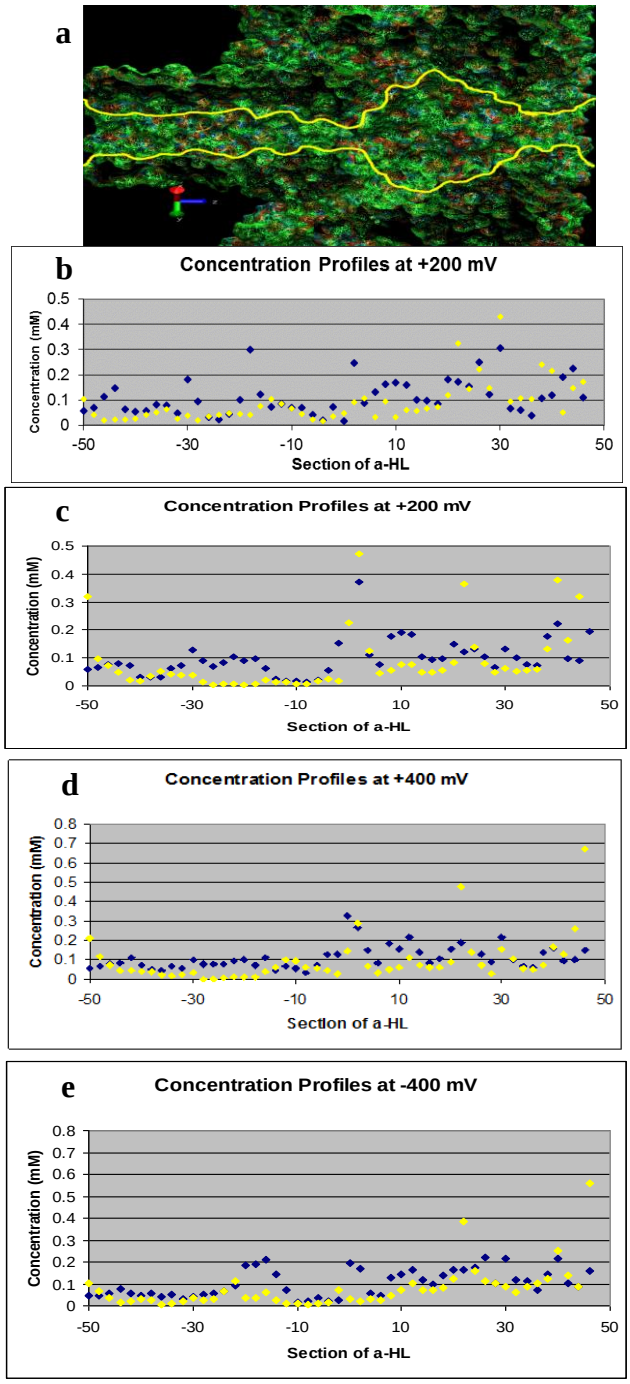


**Figure 2.7:** a. An outline of the approximate shape (in yellow) of the pore of α-HL. In the channel structure, green indicates neutral residues, blue indicates acidic residues, and red indicates basic residues. b. Concentration profiles of the α-HL channel calculated at +200 mV with the entire pore structure frozen. Blue dots are [Cl-] and yellow dots are [Na+]. c-e. These concentration profiles were calculated at the indicated voltage biases with the residues freed at the protein–solvent interface.

When comparing concentration profiles for opposite voltage biases e.g. +400mV (Figure 2.7d) and -400mV (Figure 2.7e), it can be noted that there are noticeable differences in populations of chloride ions dependent upon the voltage bias. For the +400mV bias, where the Cl- ions would be driven right to left through the channel on the axes that are depicted in the figure, there is a higher concentration of chloride anions on the right side of the selectivity filter (which is centered approximately at section -6 in the concentration profiles). Conversely, there is a heightened Cl- concentration to the left of the selectivity filter in the -400mV bias , where Cl- anions would be moving left to right across the channel, on the opposite side of the selectivity filter. As, for permeating Na+ ion, there is also a buildup of charge to the left of the selectivity filter at -400mV, while there is just a small peak in Na+ to the right of the filter region at +400mV. This behavior suggests that this particular region of the channel structure is acting as a bottleneck for permeating ions. Not only does it form a narrow aperture but, additionally, the charged ring of salt bridges, formed between residues lysine147 and glutamate111, is located at the protein surface. Judging from the buildup of charge on either side of this region at each voltage bias, it is reasonable to conclude that a structural change at this location would have a significant effect on the overall current, which we found to be true.

A general trend that can easily be noted in the concentration profiles is that chloride ions are more likely to be found in the narrow parts of the channel. This includes the most constricted part of the channel, predominantly formed by (positively charged) lys147 and (negatively charged) glu111, which serves as a weak selectivity filter for α-HL since lysine has a longer side chain and thus extends further into the channel. This is indicated by the fact that chloride concentrations are consistently higher than the concentrations of sodium ions at this location in the pore as well as in rest of the stem region in general.

### 2.3.3 Diffusion Constant Data

MSD values were computed at 0V applied potential for both sodium and chloride ions and were used to calculate diffusion constant values by plotting MSD versus time, as explained in section **2.2.7** of this chapter. A summary of the calculations (Table 2.2) shows that for our system we find that the average decrease in the diffusion constant for each ion type is just over 50%, which is the same drop in diffusion constant that was estimated for other permeation studies (Misakian and Kasianowicz, 2003). For the ion types that we tested ($K^+$, $Na^+$, and $Cl^-$), the results obtained with the FACF methodology showed an average decrease of 45-50% from the bulk value for moving an ion from bulk solution to the stem region of the channel. The FACF results (Figure 2.9) were used for the pore diffusion constant values in our PNP and BD calculations, as it has been found in previous work (Mamonov et al., 2006) that FACF is a more accurate method for calculating local diffusion constants.

| Ion | External (Å^2/ps) | Internal (Å^2/ps) | Reduction (%) |
|---|---|---|---|
| Na+ at 0mV | 0.111 | 0.0507 | 54.3 |
| Cl- at 0mV | 0.0796 | 0.0381 | 52.1 |
| | | **Average** | **53.2** |

**Table 2.2** Diffusion values for ions in the α-HL system using MSD method.

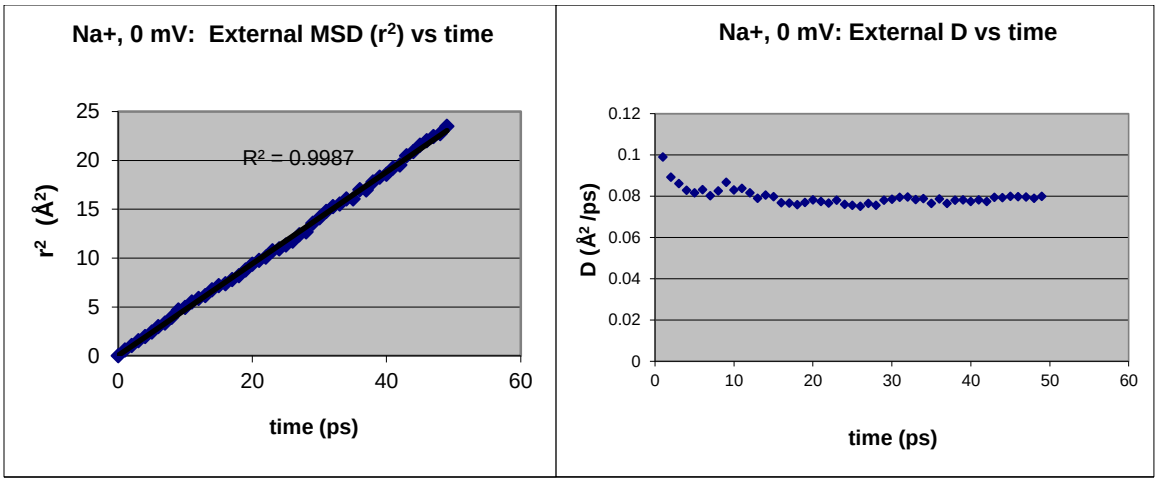


**Avg. D(External Na+, 0mV) = 0.111 Å²/ps**

**Figure 2.8.** A sample plot for the calculation of D for ions in the simulation system. The above graphs are for sodium cation at 0V applied potential in bulk solution (external to the channel). The left plot is mean squared displacement (MSD) vs. time, while the right plot is a calculation of D as determined by dividing MSD by 6*time. This calculation was carried out for sodium cation and chloride anion in bulk solution as well as within the α-HL pore, with and approximate reduction in D of 50% for each ion type.

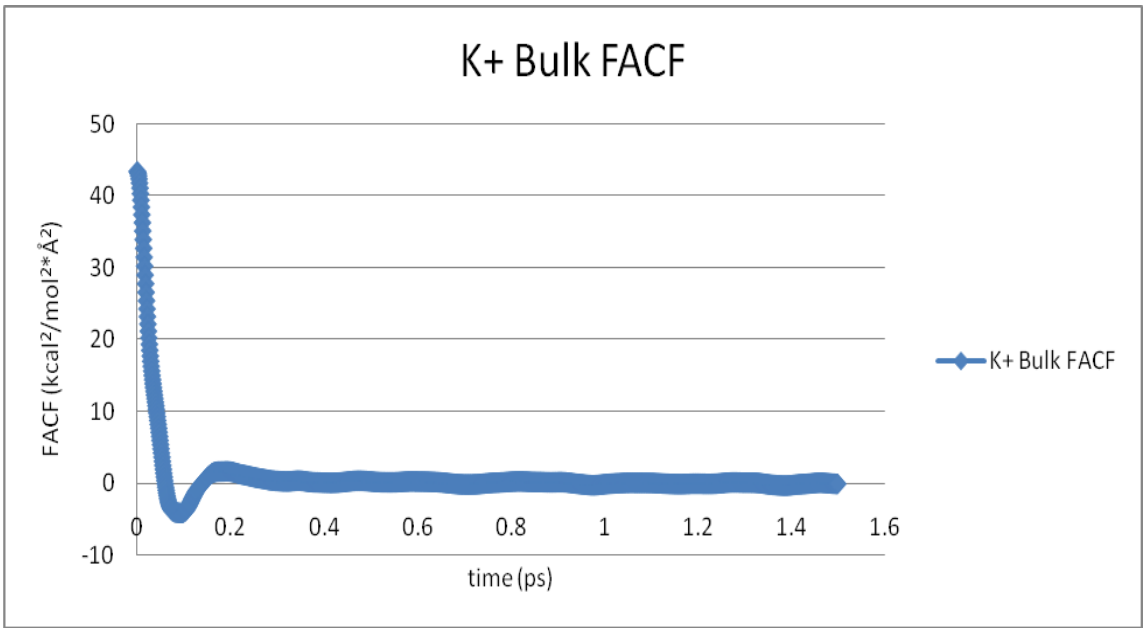


**Figure 2.9:** A graph of FACF vs. time, over a 10ns trajectory (K+ also in a box of 1077 water at 1Atm). Evaluation of the integral of this followed by the dividing of $(k_BT)^2$ (in $kcal^2/mol^2*Å^2$) by this value yields a D value of 0.19 $Å^2/ps$. Repeating this calculation for a K+ ion inserted into the narrow region, at z = -10Å, z = -25Å, and z = -40Å, of the a-HL channel yielded a value of approx. 0.10 $Å^2/ps$, or a reduction of about 47%; similar reductions were found for Cl- and Na+.

### 2.3.4 Mutation of lysine 147

Our initial attempt to alter the permeant properties of α-HL by a single point mutation was to mutate all seven lys 147 residues to glutamate, creating a concentrated region of acidic amino acids in order to provide a significant shift in structural charge at this location and making this region (and the channel) selective for cations instead of anions. This had a destabilizing effect on the channel structure as it began to push apart almost immediately upon equilibration in this region due to the presence of fourteen glutamate residues (in addition to the seven glu11 residues) forming a ring around the pore, all repelling one another. We found, however, that the mutation of lysine 147 to serine produced a stable protein structure, as the α-HL system retained its native form throughout equilibration in a POPC membrane. It is a possible source of concern that this lys147→ser mutation is negating the presence of the ring of salt bridges at this location, considering the central location of these residues in the pore structure, as well as the stability that salt bridges supply to native protein conformations in general. We suggest that the viability of this mutated structure be tested experimentally to see if the protein will appropriately self-assemble into functional form with this point mutation. It is important to note, however, that using serines instead of glutamate residues and the subsequent structural stability shows some promise that the mutant structure will be a functional form of this protein.

Our PNP as well as BD results (Figures 2.10 and 2.11) show that the selectivity favoring anions at 1.0M concentration is reversed when all seven lys147 residues are mutated to serine, supporting our hypothesis that lys147 is the key residue responsible for anion selectivity in this channel. Furthermore, the current rectification of the system is also reversed when the mutation is applied (Figures 2.10 and 2.11), following with our suggestion that shortening the side chain at

residue 147, and the subsequent change in the asymmetry of the pore diameter at opposite ends of the stem region would cause result in a shift in current rectification for the this channel. The change in selectivity (as well as a change in overall I-V values and current rectification) is much more apparent at a concentration of 0.10M, (Figure 2.12) where the charges of the protein channel have much greater effect on the mobile charges since the Debye radius is inversely proportional to the square root of the solute concentration.

When using PNP to test the reversal potential of the native and mutated α-HL structures (Figure 2.13), we find a change in selectivity of the channel, where it should be noted that the sign of the reversal potential reflects either cationic vs. anion selectivity, while the magnitude of the reversal potential indicates the strength of selectivity for that ion type. For the system, results show that, with an internal bath concentration of 1.0M NaCl and an external bath concentration of 0.1M, the native structure has a value of +2.8 mV (indicating slight anionic selectivity), while for the mutant structure this value was -9.2 mV (indicating somewhat stronger cationic selectivity). It has been shown (Choudhary et al., 2011) that, even though PNP may have some discrepancy from experiment with regard to the magnitude of I-V values, the calculated reversal potential is often close to the experimental value. As such our reversal potentials may be verified experimentally in order to validate our predicted changes in selectivity.

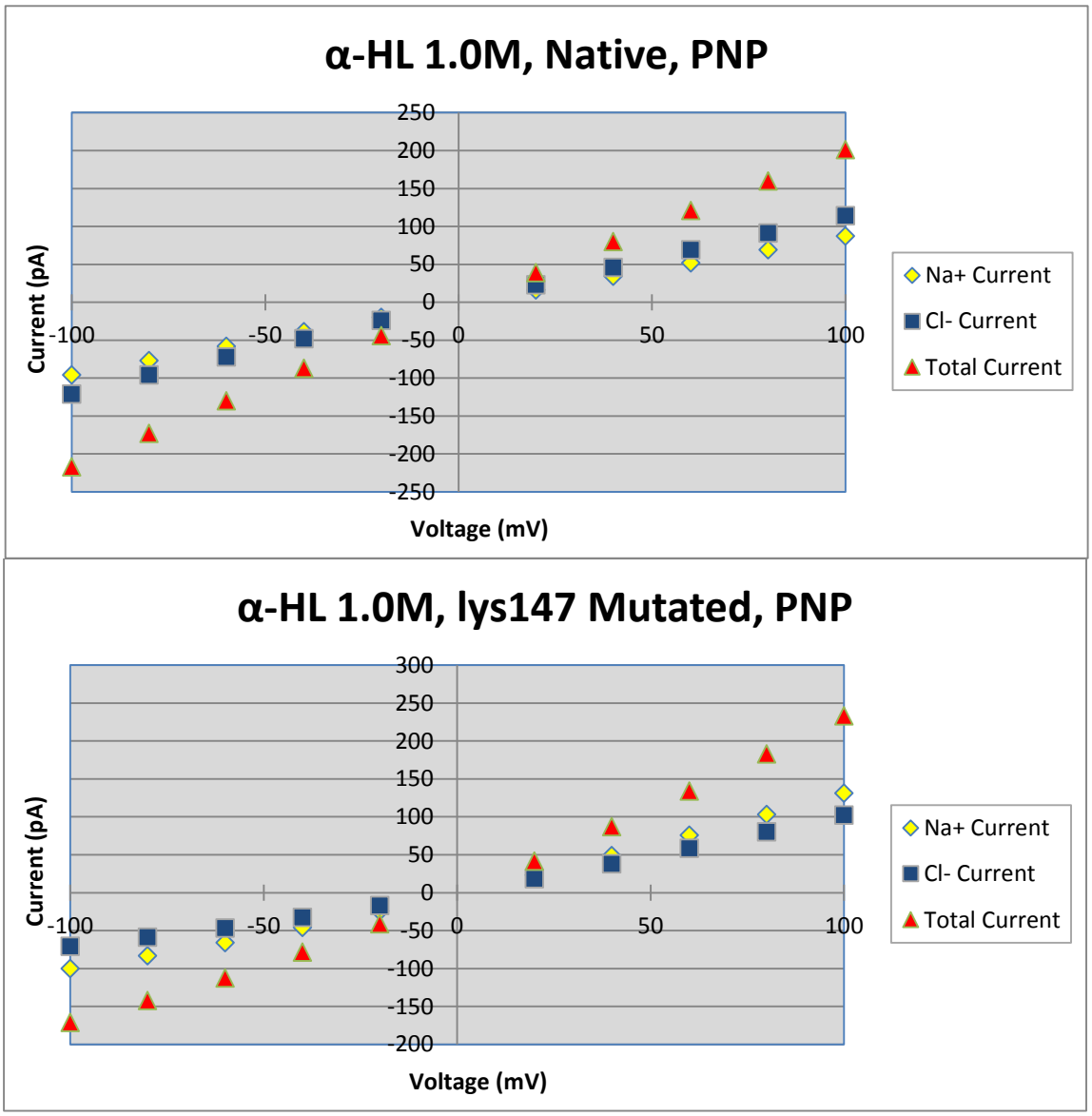


**Figure 2.10:** These charts show current-voltage (I-V) data for the native and mutated structures of α-HL, calculated using PNP. Note the change in selectivity as well as current rectification between the native and mutant structures.

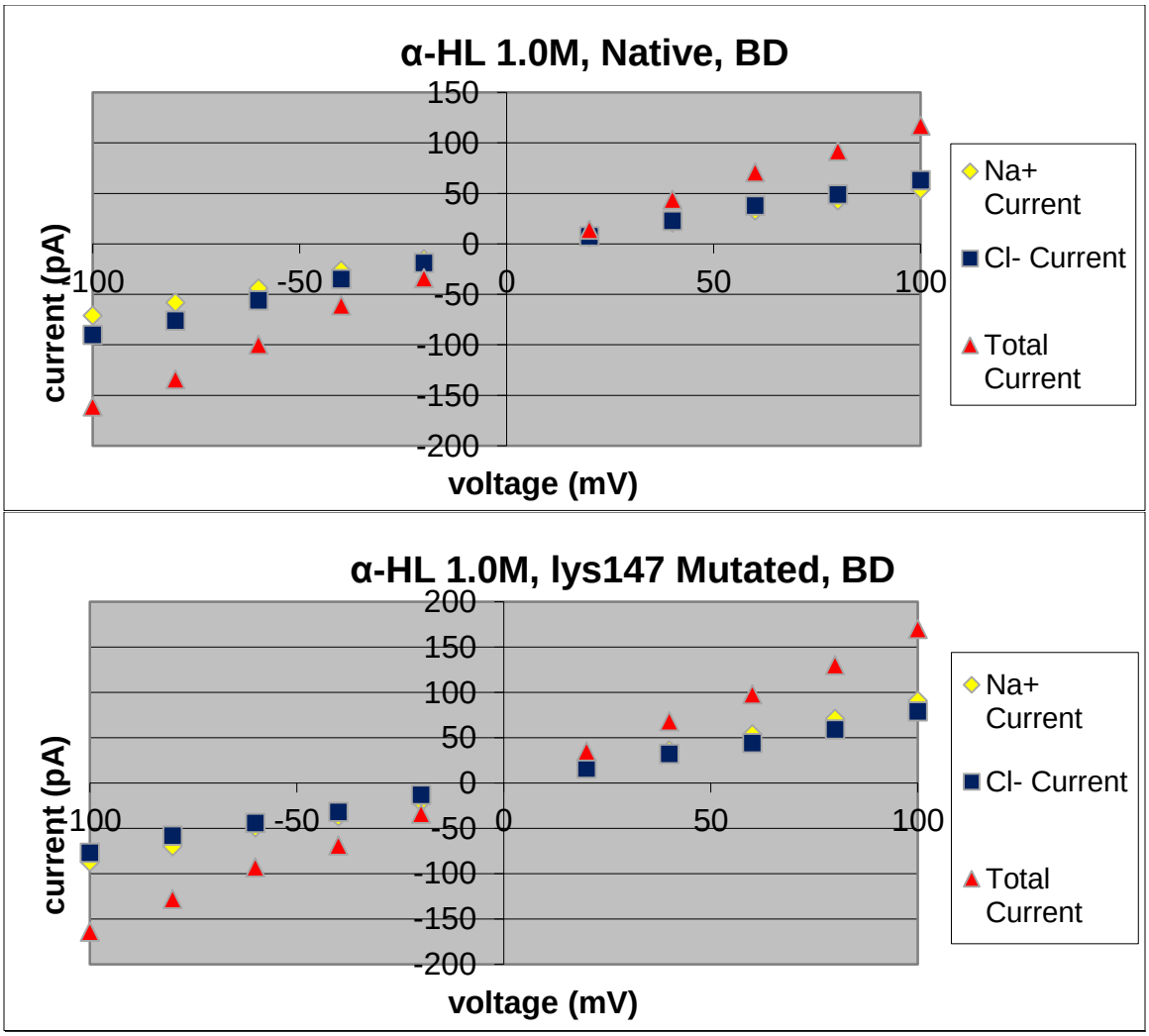


**Figure 2.11:** These charts show current-voltage (I-V) data for the native and mutated structures of α-HL, calculated using BD. Note the overall smaller numbers for current calculations as compared to PNP, but similar behaviors are observed in terms of the change in selectivity as well as current rectification between the native and mutant structures.

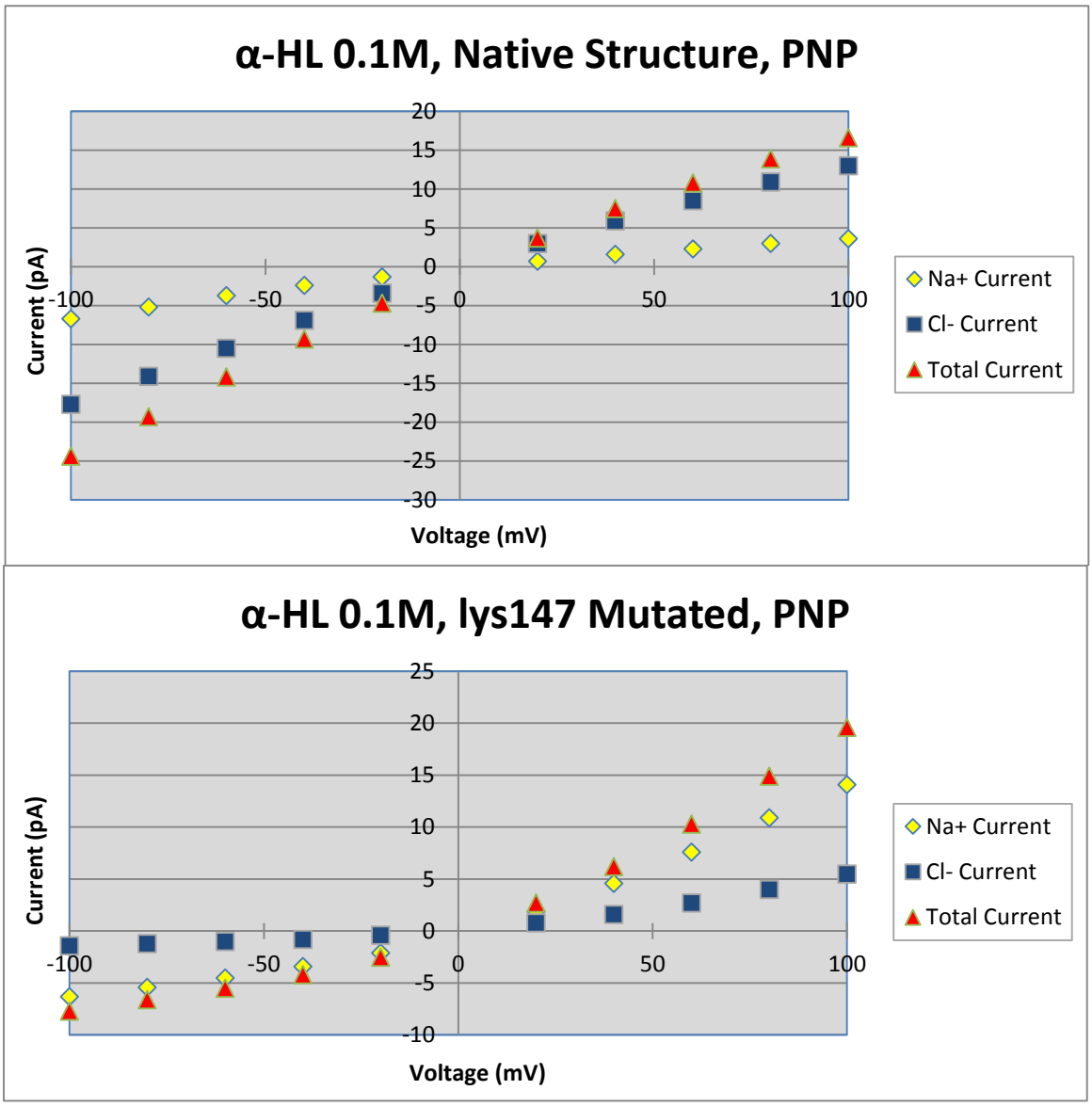


**Figure 2.12:** PNP I-V results with a solution concentration of 0.1M. Note that the change in selectivity as a result of the mutation, as well as the change in current rectification, is much more pronounced at a lower concentration.

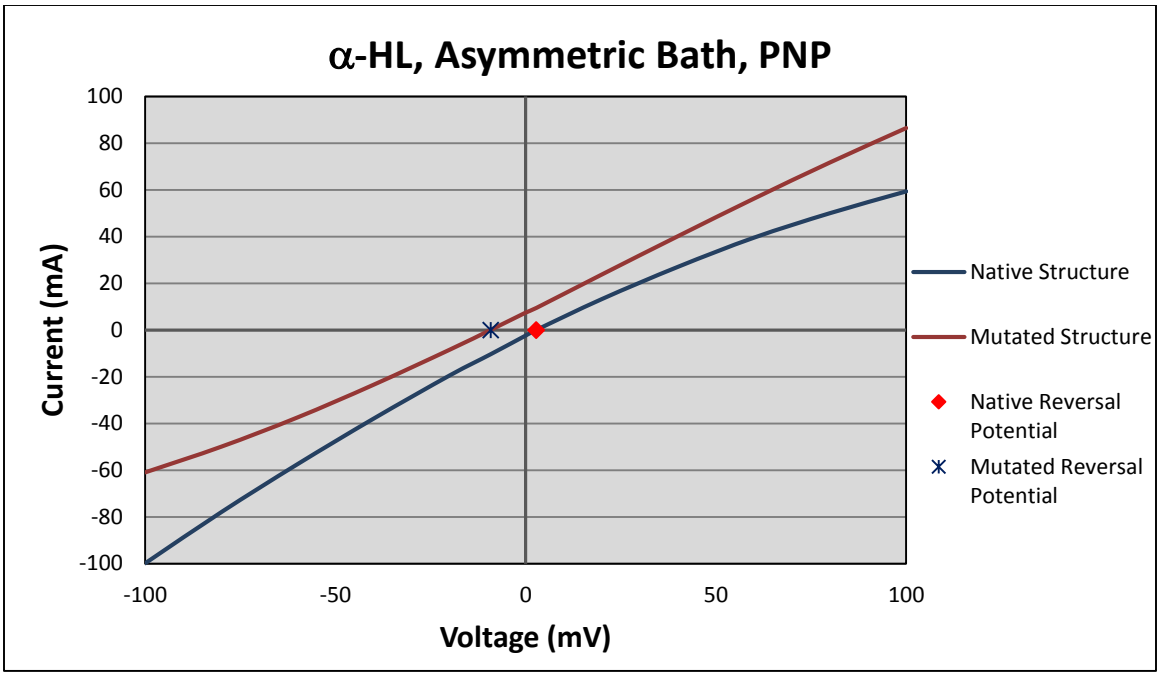


**Figure 2.13**: PNP I-V results using an asymmetric bath, with the stem side of the membrane at 0.1M and the cap side at 1.0M. The reversal potential, or the applied voltage where the system current is zero, is found where the I-V curves the horizontal axis. For the native structure, this value was calculated at at +2.8 mV, while this value for the mutant structure was at -9.2 mV. This change in reversal potential can be attributed to the change in channel selectivity as a result of the mutation.

## 2.4 CONCLUSIONS

This study, which used concentration profiles produced from NEMD simulations, suggests a single residue mutation may that significantly change the I-V characteristics of the α-HL channel. This serves as motivation to use these simulation techniques to explore whether structural changes in other ion channel systems control their permeant properties as well. Specifically, it may be useful in channels such as the inwardly rectifying potassium channel, KIR, where a few key residues are responsible for both selectivity as well as rectification. In comparison to other methods used, NEMD allows the investigator to monitor the explicit locations of every atom in the system and their movement throughout a simulation. In our NEMD simulations we were able to see an advantage of allowing the surface residues of α-HL to move, specifically in the situation where ions were migrating into the channel structure when the entire protein was frozen.

As for permeant properties of the channel, our NEMD, BD, and PNP data has shown rectification as well as selectivity in the I-V data, using a standard charge set corresponding to a neutral pH value. Of the three simulation methods, NEMD provided the most accurate I-V results as compared to experimental results (Misakian and Kasianowicz, 2003), and while the calculated current was consistently high for our BD and PNP calculations, both methods proved to be qualitatively accurate for all scenarios that we calculated for this system. Considering that PNP and BD have been shown to provide less reliable results for more narrow ion channels (Corry et al., 2000; Mamonov et al., 2003; Graf et al., 2004), NEMD becomes particularly important for examining I-V properties of such systems. Furthermore, we would like to perform additional NEMD and BD calculations of this system using assymetric bath conditions, as we now have sufficient calculated PNP data for comparison.

For the purposes of our calculations, it was sufficient to embed α-HL in a rigid matrix of dummy atoms for our MD simulations, considering the short time scales of the trajectories. However, it is likely important to include a fully atomistic membrane in future work dealing with other channels of interest, such as GlyR or KcsA, where the pore is narrower and small protein fluctuations and subtle differences in electric potential inside the channel may have much more significant effects. Even with a wide channel such as α-HL, further studies where the entire pore structure is allowed to move and is embedded in an atomistic membrane may be of interest, as large scale motions of the protein structure can be observed over times scales longer than what was done in this study.

# 3.0 EFFECTS OF PH DEPENDENCY OF TITRATABLE RESIDUES IN THE ION CHANNEL ALPHA-HEMOLYSIN, STUDIED BY THREE-DIMENSIONAL POISSON-NERNST-PLANCK THEORY

## 3.1 INTRODUCTION

Modeling the function of biological ion channels has progressed significantly over the past several decades, as a result of experimental as well as theoretical work (Bezanilla and Armstrong, 1972; Jordan, 1982, 1983, 1987; Levitt, 1985; Chen et al., 1992; Cardenas et al., 2000). With the availability of detailed atomistic structures of ion channels, various computational techniques have been applied in order to simulate the behavior of these channels, particularly the permeation of ions through the channel pore. The methodologies include Non-equilibrium molecular dynamics (NEMD) (Aksimentiev and Schulten, 2005, Kutzner et al., 2011), Poisson-Nernst-Planck (PNP) (Chen and Eisenberg, 1993; Kurnikova et al., 1999), and Brownian dynamics (BD) (Chung et al., 1998, Graf et al., 2000, Cheng et al., 2005). While there have been many publications calculating ion conduction, i.e., current-voltage (I-V), behavior of protein channels, to date there have been few theoretical works on pH-dependent I-V properties of ion channels. Existing work has been limited in scope by either describing an artificial channel (Borisenko et al., 2000), applying a simplified one-dimensional model to represent a real channel (Misakian and Kasianowicz, 2003), or only addressing charge states of a few residues within a channel structure (Aksimentiev and Schulten, 2005).

In this study, we propose to use 3-D PNP to calculate the pH–dependent current-voltage behavior of α-HL, previously described in experimental work for this system (Misakian and

Kasianowicz, 2003). We will use a fully atomistic structure of the channel, with charge states of all titratable residues modified corresponding to various pH values reported in the Misakian and Kasianowicz 2003 publication, investigating specific residues in the channel structure that have been suggested as molecular components responsible for pH-dependent behavior of the channel. As it is still a matter of debate how charge states of buried titratable residues (i.e. those residues that are internal to the protein structure) respond to changes in solution pH (Fitch et al., 2002; Pace et al., 2009, Di Russo et al., 2012), we will calculate I-V curves of α-HL with modified charge states of surface residues (those residues that are located at the protein-solvent interface) only, and also with modified charge states of surface as well as buried residues. Examining which of these scenarios result in ion permeation properties that most closely reproduce experimental results should provide insight into whether buried residues in the channel structure are indeed changing in charge state in response to bathing solution pH.

Additionally, α-HL has been shown to increase in anion selectivity as pH decreases from near neutral (pH 7-8) to low (pH 4) values (Menestrina, 1986, Gu et al., 2001). It has been suggested that this behavior can be explained by the changing titration states of two histidine residues (His144 and His259) within the channel structure (Aksimentiev and Schulten, 2005). Specifically, we will test this assertion by using our simulation methods to determine whether any changes in selectivity occur upon recalculation of charge states of these titratable residues at varying values of pH.

It has been shown in numerous works that changing the charge states of ionizable residues within an ion channel structure can affect its I-V properties (Prod'hom et al., 1987; Root and MacKinnon, 1994; Kasianowicz and Bezrukov, 1995; Rostovtseva et al., 2000). Changes in charge states of titratable amino acid side groups can be effected by changing the pH of the bathing

solutions on either or both sides of the membrane. In order to effectively simulate variable pH experimental conditions and subsequent effects on channel behavior, it is necessary to be able to accurately calculate the charge states of titratable residues at varying pH. If the pH environment of a residue is known, its protonation probability, and thus its most probable charge state, may be calculated upon the determination of the pKa of the titratable group by use of the Henderson-Hasselbach equation (Equation 3.1) ((Henderson, 1908, de Levie, 2003).

In recent years there have been numerous approaches to describe the charge states of titratable residues in proteins, where many use a combination of continuum electrostatics and statistical thermodynamics (Bashford and Karplus, 1990, 1991). Most of these methods are based on electrostatic continuum models that numerically solve the linearized Poisson-Boltzmann equation (Yang et al., 1993; Schaefer et al., 1997). In these methods solvent is typically treated as a uniform dielectric continuum (with dielectric constant of 80) and the volume occupied by the protein is assigned a uniform dielectric constant between 4 and 20. A pKa shift is calculated from the difference in electrostatic energy of a residue in its charged and neutral form and this shift is added to the residue's reference (solvated, neutral pH) pKa value. While being reasonably accurate, these models tend to overestimate charge–charge interactions within the protein structure (Forsyth et al., 1998; 2000) as well as underestimate influence of hydrogen bonding and desolvation, or Born, effects in calculating pKa shifts (Laurents et al., 2003). Considering this, we have decided to use the software utility PROPKA, which uses an empirical method of determining pKa values of all titratable residues in a protein structure (Li et al., 2005; Bas et al., 2008). It utilizes a combination of residue-specific parameters to accommodate for the most significant factors that would affect the pKa of titratable groups within protein structures, including hydrogen bonding, charge-charge interactions, and desolvation effects. PROPKA predicts side chain pKa

values with a root-mean-square deviation (RMSD) from experiment of less than 1 for most residues, providing similar or more accurate predictions than other current methods.

The model system under consideration for this work is the bacterial ion channel α-hemolysin (α-HL), a heptameric protein which is secreted from Staphylococcus aureus as a water soluble monomer and self-assembles into its functional form upon binding to a lipid bilayer (Gouaux, 1994; Song et al., 1996; Braha et al., 1997; Gouaux, 1998). This system is a good candidate for computational study since a great deal is already known about its 3-dimensional structure (Song et al., 1996) as well as its ion conduction properties (Menestrina, 1986; Bezrukov and Kasianowicz, 1993; and Kasianowicz and Bezrukov, 1995). Specifically, The I-V relationship of this channel is nonlinear and rectifying, and the nonlinearity is pH-dependent (Kasianowicz and Bezrukov, 1995). These characteristics were described with a one-dimensional Nernst-Planck analysis of a simplified model of the channel structure, containing fixed charges assigned to represent titratable amino acids at three locations along the length of the pore, near the center and each entrance (Misakian and Kasianowicz, 2003). The fixed charges in the model were varied according to bath pH values and I-V data was calculated, providing reasonable qualitative similarities to experimental data; but it was concluded that a more detailed simulation approaching, including a three-dimensional representation of the channel; should be carried out.

A limitation in using PNP methodology is that the protein structure remains fixed throughout the course of the simulation, which makes this particular channel system a good candidate to study with this method, as α-HL has been reported to remain in a fully open state indefinitely during I-V measurements (Kasianowicz, 1994). Additionally, a potential concern is changing pH conditions in the range observed in the comparison experimental measurements (between 4.5 and 7.5) has been shown to drastically alter protein structure (Fitch et al., 2002,

Platzer et al., 2014). However, the structure of α-HL is thought to be largely unaffected in this range of pH values and any changes in permeant properties of the systems would therefore be due to changes in fixed charges within the channel structure (Misakian and Kasianowicz, 2003). Even though PNP is not expected to produce quantitatively accurate results when compared to experimental I-V data, as it systematically over-estimates current measurements by as much as a factor of two (Im and Roux, 2002, Choudhary et al., 2010), as a method it is accurate with respect to qualitative aspects of permeation characteristics such as selectivity and rectification ratio (as discussed in chapters one and four of this document) in wide ion channels like α-HL. Thus, it is reasonable to expect that I-V data calculated using PNP will serve as an effective means of determining which titratable residues are responsible for determining the pH-dependent I-V behavior observed in experimental results.

## 3.2 METHODS AND CALCULATIONS

The crystallographic structure for α-HL (Song et al., 1996) was downloaded from the RSCB protein data bank (Berman et al., 2000) and initial coordinate and charge files were generated using the software package VMD (Humphrey et al., 1996). pKa values for all titratable groups were calculated using PROPKA and partial charges were assigned at varying pH conditions according to protonation probabilities calculated using the Henderson-Hasselbach equation:

$$\langle x \rangle = \frac{10^{pKa-pH}}{1+10^{pKa-pH}} \tag{3.1}$$

where $pH$ is the bathing solution pH, $pKa$ is the calculated pKa value of the residue, and $\langle x \rangle$ is the protonation probability of the residue ($0 < \langle x \rangle < 1$). In practical terms, considering that protonation probability of a titratable residue is found as a decimal value between 0 and 1, if given a population of that titratable residue, all able to exchange protons with their surroundings, the protonation probability is the likelihood than any randomly chosen residue in the population would be protonated at any given time.

Upon finding the protonation probabilities of titratable groups, most current techniques modeling protein behavior will use a structure with fixed protonation states, chosen according the most probable arrangement at a given pH, and leave all titratable residues in their protonation state (protonated or deprotonated) for the duration of the simulation. In order to account for reversible protonation at titratable sites during simulation, methods may either allow for proton exchange to occur at these sites during simulation (Warshel and Weiss, 1980; Day et al., 2002) or use a more crude method of assigning fixed fractional charges to residues according to their protonation probabilities (Spassov and Yan, 2008; Anufriev and Alexov, 2013). Descriptions of biological phenomena involving rearrangement/exchange of charges within the protein structure, such as

ligand binding reactions (Kozlov and Lohman, 2000), peptide insertion in membranes (Tamm and Han, 2000), and pH-dependent conformational changes (Dobson, 2003), would greatly benefit from a dynamic description of the protonation states. However, for our system, the structure is not undergoing any pH-dependent conformational changes, and mobile ions are not binding at any particular sites within the channel structure. As such, we are assigning fractional charges to titratable residues, proportional to their protonation probabilities, either at the carboxyl oxygen of acidic groups or the nitrogen of basic (amine) groups within the titratable residues. For acidic residues such as glutamatic acid (glu) and aspartic acid (asp), protonation values approaching 0 correspond to deprotonated, or negatively charged states, while protonation values approaching 1 correspond to uncharged states. For basic residues such as lysine, arginine, and histidine, protonation values approaching 1 correspond to protonated, or positively charged states, while protonation values approaching 0 correspond to uncharged states.

The experimental procedure from the Misakian and Kasianowicz 2003 study consisted of starting with solutions on both sides of the membrane at pH 7.5, reducing the pH of just one side of the membrane to 4.5 and then measuring I-V properties of the channel. To model this experimental setup in our calculations, we first calculated the partial charges of all titratable residues using pKa values calculated using PROPKA and a pH of 7.5. We then classified the residues within the $\alpha$-HL structure as being either surface (Table 3.1) or buried (Table 3.2) residues as well as being located on either the cis (intracellular) or trans (extracellular) side of the channel structure (Figure 3.1), and thus exposed to the pH of the bathing solution on that side of the membrane. Then, selecting residues on the side of the channel structure exposed to lowered pH, the fractional charges of titratable residues within the channel were calculated either **i.** just for

residues at the surface of the protein (residues that would be exposed to the lower pH environment at the protein/solvent interface) or **ii.** for both surface as well as buried residues.

Some residues were calculated to have only a negligible change in protonation probability changing between a pH environment of 4.5 and 7.5, and thus do not change in charge state across these pH values. These are indicated by N/A in the tables below. While most protonation probabilities of these residues at pH 7.5 using pKa values calculated with PROPKA are similar to what would be found by using bulk solution pKa values (which are also the default charges assigned by the force field parameter set used in VMD), there were some significant changes at pH 4.5.

| Residue | Bulk pKa | Calc. pKa | Region | pH 7.5 prot. prob. | pH 4.5 prot. prob. |
|---|---|---|---|---|---|
| Glu31 | 4.1 | 4.5 | Cis | 0.00099 | 0.50 |
| Glu70 | 4.1 | 4.3 | Cis | 0.00069 | 0.41 |
| Glu71 | 4.1 | 4.2 | Cis | 0.00054 | 0.35 |
| Asp92 | 3.9 | 3.6 | Cis | 0.00013 | 0.11 |
| Glu94 | 4.1 | 4.2 | Cis | 0.00049 | 0.33 |
| Glu111 | 4.1 | 4.1 | Cis | 0.00043 | 0.30 |
| Asp128 | 3.9 | 2.9 | Trans | 2.7E-05 | 0.026 |
| Asp183 | 3.9 | 2.9 | Cis | 2.5E-05 | 0.025 |
| Asp208 | 3.9 | 4.0 | Cis | 0.00030 | 0.23 |
| Asp212 | 3.9 | 2.7 | Cis | 1.6E-05 | 0.016 |
| Asp246 | 3.9 | 2.3 | N/A | 6.9E-06 | 0.0069 |
| Asp255 | 3.9 | 2.7 | Cis | 1.6E-05 | 0.016 |
| Glu287 | 4.1 | 4.5 | Cis | 0.00010 | 0.50 |
| Glu290 | 4.1 | 4.3 | Cis | 0.00065 | 0.39 |
| Tyr191 | 10.1 | 9.4 | Cis | 0.99 | 1.0 |
| Lys131 | 10.5 | 9.5 | Trans | 0.99 | 1.0 |
| Lys205 | 10.5 | 10.1 | N/A | 1.0 | 1.0 |
| His259 | 6.1 | 6.5 | Cis | 0.091 | 0.99 |
| His144 | 6.1 | 4.1 | Cis | 0.00037 | 0.27 |

**Table 3.1:** A list of titratable surface residues considered for pH-dependent calculations, pKa in bulk solution, pKa calculated using PROPKA, the bathing solution to which the residue would be exposed, and their protonation probabilities at either pH 7.5 or pH 4.5.

| Residue | Bulk pKa | Calc. pKa | Region | pH 7.5 prot. prob. | pH 4.5 prot. prob. |
|---|---|---|---|---|---|
| Asp13 | 3.9 | 6.2 | Trans | 0.047 | 0.98 |
| Asp108 | 3.9 | 6.0 | Cis | 0.028 | 0.97 |
| Glu289 | 4.1 | 5.2 | Cis | 0.0050 | 0.83 |
| Tyr182 | 10.1 | 9.6 | N/A | 0.99 | 1.00 |
| Lys50 | 10.5 | 9.7 | N/A | 0.99 | 1.00 |
| Lys58 | 10.5 | 8.2 | Cis | 0.83 | 1.00 |
| Lys154 | 10.5 | 8.6 | Cis | 0.92 | 1.00 |
| His48 | 6.1 | 5.2 | Cis | 0.0050 | 0.83 |

**Table 3.2:** A list of titratable buried residues considered for pH-dependent calculations, pKa in bulk solution, pKa values calculated using PROPKA, the bathing solution to which the residue would be exposed, and their protonation probabilities at either pH 7.5 or pH 4.5.

In order to assess if any significant changes in the channel structure result from these modified charge states we tested their stability using molecular dynamics by inserting the channel structure in a POPC membrane using VMD (Humphrey et al., 1996), solvating, and adding ions corresponding to a 1.0M NaCl bathing solution to produce a simulation box of dimensions 140×140×150Å, and then running 3000 minimization steps using NAMD (Kale et al., 1999). We then equilibrated the structure using NAMD as an NTP ensemble at 298K and 1.0 atm pressure applied in the z-dimension (along the channel axis), with the first ns of the simulation keeping the alpha carbons of the protein restrained and then in the following 4 ns allowing the entire protein to move. We checked the root mean-square deviation value of the alpha carbons from their initial positions throughout the equilibration and considered the structure to be stable if the deviation remained at a consistent value less than 2.0Å after the first ns of unconstrained equilibration. This was done for the system under three different conditions: (**i**.) all residues with standard (fully solvated, neutral pH) charges; (**ii**.) using pKa values calculated with PROPKA, internal residues with charge states corresponding to pH = 7.5 and surface residues charge states corresponding to protonation probabilities at pH 4.5; and (**iii**.) using pKa values calculated with PROPKA, all titratable residues (surface and buried) with charge states corresponding to protonation probabilities at pH 4.5. The overall structural integrity of the channel was maintained through all

equilibrations and there was no significant changes in pore dimensions, in accord with assertion to this in the works of Misakian and Kasianowicz 2003 as well as Aksimentiev and Schulten, 2005.

Current-voltage characteristics were calculated using 3-dimensional Poisson-Nernst-Planck continuum theory (Chen and Eisenberg, 1993; Kurnikova et al., 1999), described in Section **1.2**. The grid spacing for all PNP calculations was 1.2 grid points/Å and the grid size was 145Å×145Å×205Å, insuring that the entire crystal structure was contained within the simulation box, with room for bathing solutions at either end of the channel. The probe radius for these calculations, which determines the dielectric boundary between the protein and mobile charge continuum, was 1.4 Å (the radius of a water molecule), and volume occupied by the protein structure was assigned a dielectric constant of 4. The diffusion constant for mobile charge was the average of the bulk diffusion constant values of sodium cation and chlorine anion, except within the stem region of the channel, where this value is reduced by half, based on the calculations described in section **2.3.3** (Figure 3.1).

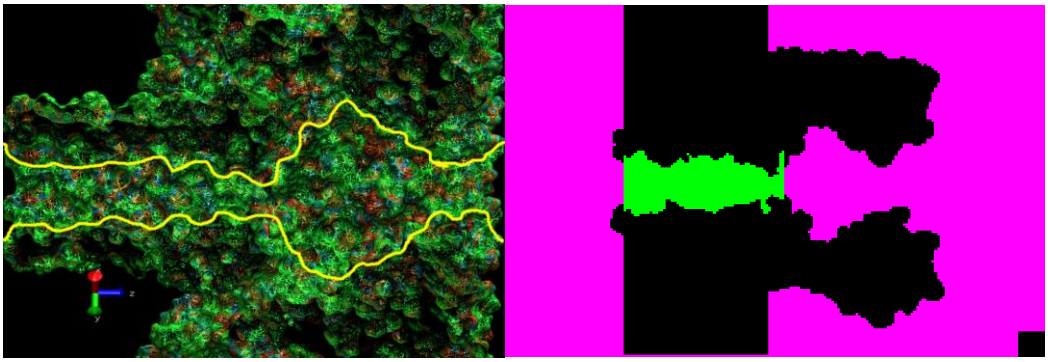

**Figure 3.1:** At left, the yellow lines indicate a sketch of the α-HL channel pore surface using VMD (Humphrey et al., 1996). At right, the diffusion profile for PNP caclulations, where the diffusion constant for mobile charge in the simulation box is as follows: green = 9.7 E -6 cm^2/s, pink = 1.95 E -5 cm^2/s, black = 0 cm^2/s. The right, or cap side of the channel is considered the cis side of the system, where the left, or stem side of the channel is considered the trans side of the system.

The membrane is represented as an uncharged rectangular slab with thickness of 45Å and dielectric constant of 2. Because the membrane is net neutral, fixed charges on the surface of the membrane, e.g. phosphate head groups, are not considered in the model proposed here, following methodology established in previous works (Lindemann, 1982; Krasilnikov & Sabirov, 1989; Kurnikova et al., 1999).

## 3.3 RESULTS AND DISCUSSION

### 3.3.1 pH 7.5 bathing solutions

Initial PNP calculations were done using the default charges from the CHARMM22 parameter set used in VMD to create the initial coordinate (.pdb) and charge (.psf) files, which assumes that all titratable residues are fully solvated and at pH 7.5 (Figures 3.2, 3.3). Overall, the data is qualitatively consistent with experimental observations, with a similar rectification ratio, defined as the ratio of current at a -120mV bias divided by the current measured at +120mV (Misakian and Kasianowicz, 2003). The experimental data shows a ratio of approximately 1.3 in 1.0M NaCl, where the PNP results provide a ratio of 1.24. The corresponding ratio for this system in 0.1M NaCl solution is approximately 1.5 in experimental data and is calculated as 1.56 using PNP. It has been suggested (Misakian and Kasianowicz, 2003) that there are two stable conformations of the α-HL channel at pH 7.5 and 1.0M NaCl, distinguished by different rectification ratios in 1.0M solution, 1.3 and 1.6, where the more prominently found conformation exhibits a rectification ratio of 1.3. As such, these initial PNP results indicate that the crystallographic structure of this channel used in these calculations is representative of this more prominent conformer. PNP calculations were repeated with the charge states of all titratable residues calculated using pKa values from PROPKA, at a pH of 7.5. This produced only very small differences in most protonation probabilities at pH 7.5 than what is found by using the standard solution pKa values, and re-running PNP using these adjusted charges and the I-V data was only negligibly different.

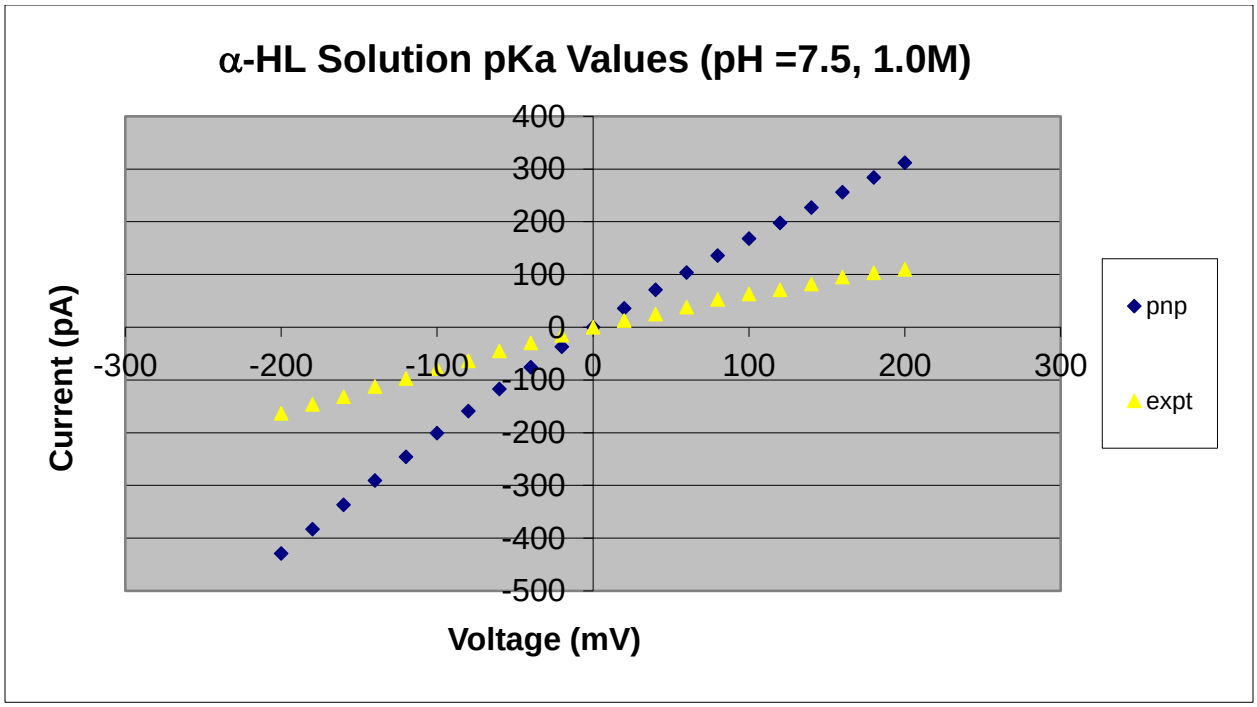


**Figure 3.2**: I-V results for a symmetric 1.0M NaCl bathing solution obtained via PNP, using standard charges from CHARMM22 force field parameters, and comparing to experimental data at pH 7.5. While current is over-estimated using PNP, semi-quantitative aspects of the channel's ion conduction behavior, such as current rectification, and rectification ratio are nearly the same as experimental observations.

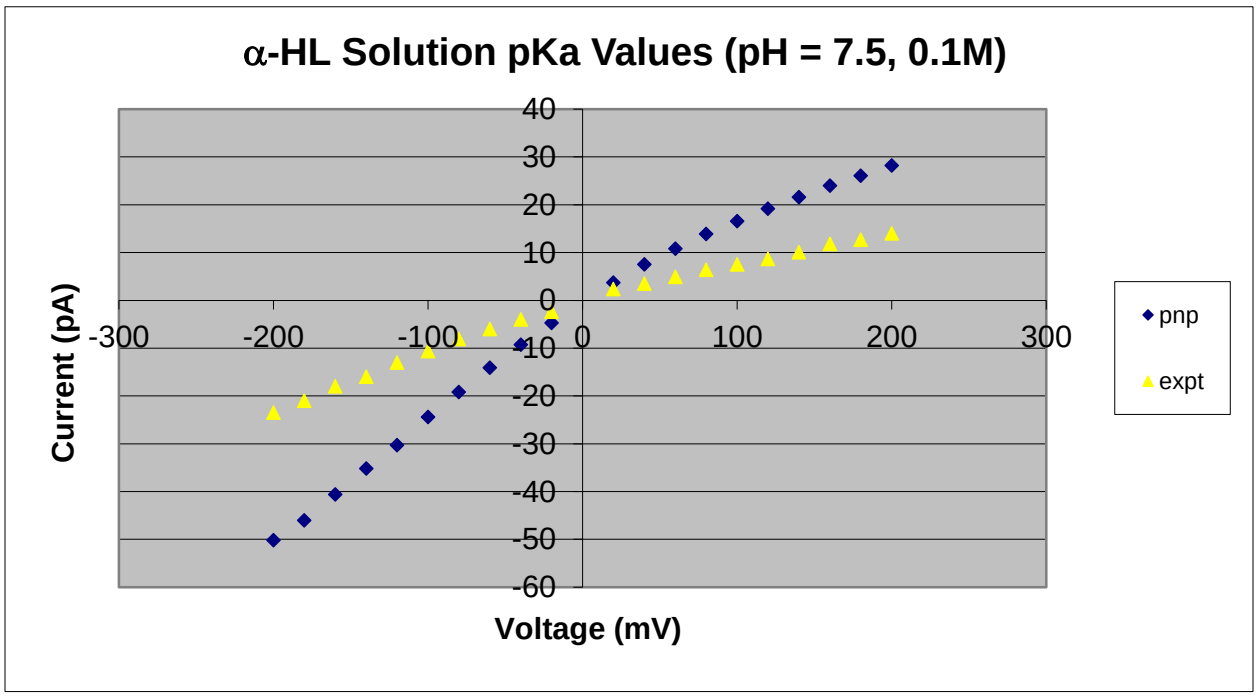


**Figure 3.3:** I-V results for a symmetric 0.1 M NaCl bathing solution obtained via PNP, using standard charges from CHARMM22 force field parameters, and comparing to experimental data at pH 7.5.

### 3.3.2 Histidine residues and pH-dependent selectivity

The reversible protonation states of His144 and His259 have been suggested as a way to vary ion selectivity as a function of pH (Aksimentiev and Schulten, 2005) in α-HL, specifically, that the channel system significantly increases in anion selectivity at lower pH. We examined the impact of altering the charge state of these two residues in pH environments of 7.5 and 4.5 and the subsequent effect on the permeant properties of this channel system (Figures 3.4 and 3.5). PNP results show that the changing protonation states of these histidine residues has only marginal effect on the I-V data, where the Cl- current is slightly increased and the Na+ current is slightly reduced at pH 4.5, with the effect being slightly more prominent at a lower concentration bathing solution. As such, this data indicates that other titratable residues within the structure likely have a greater responsibility for any changing selectivity properties of the channel as a function of pH, examined further in the following sections.

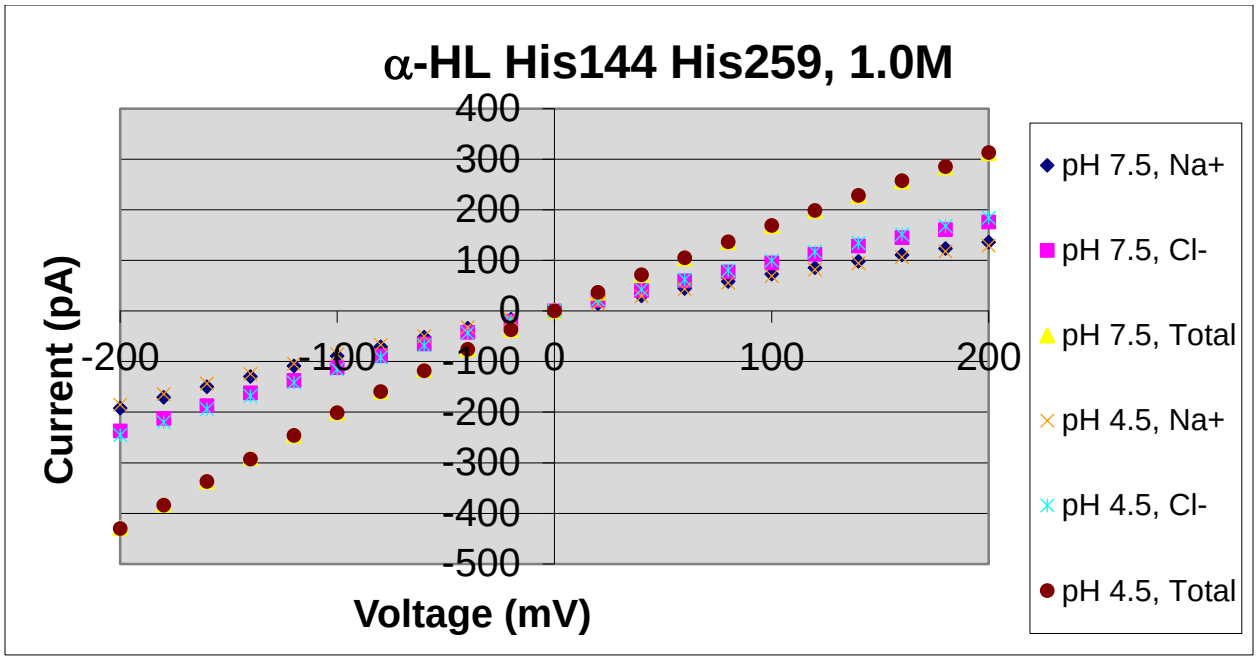


**Figure 3.4:** I-V data calculated using PNP for α-HL, where the charge states of two histidine residues, His144 and His259 are calculated at pH 7.5 and pH4.5 in a symmetric 1.0M NaCl bathing solution. All data points are nearly overlapping between pH 7.5 and pH 4.5 results, indicating that changing the charge states of just these two residues has little effect on channel selectivity and suggesting that other titratable residues in α-HL must contribute significantly to any pH-dependent changes in selectivity.

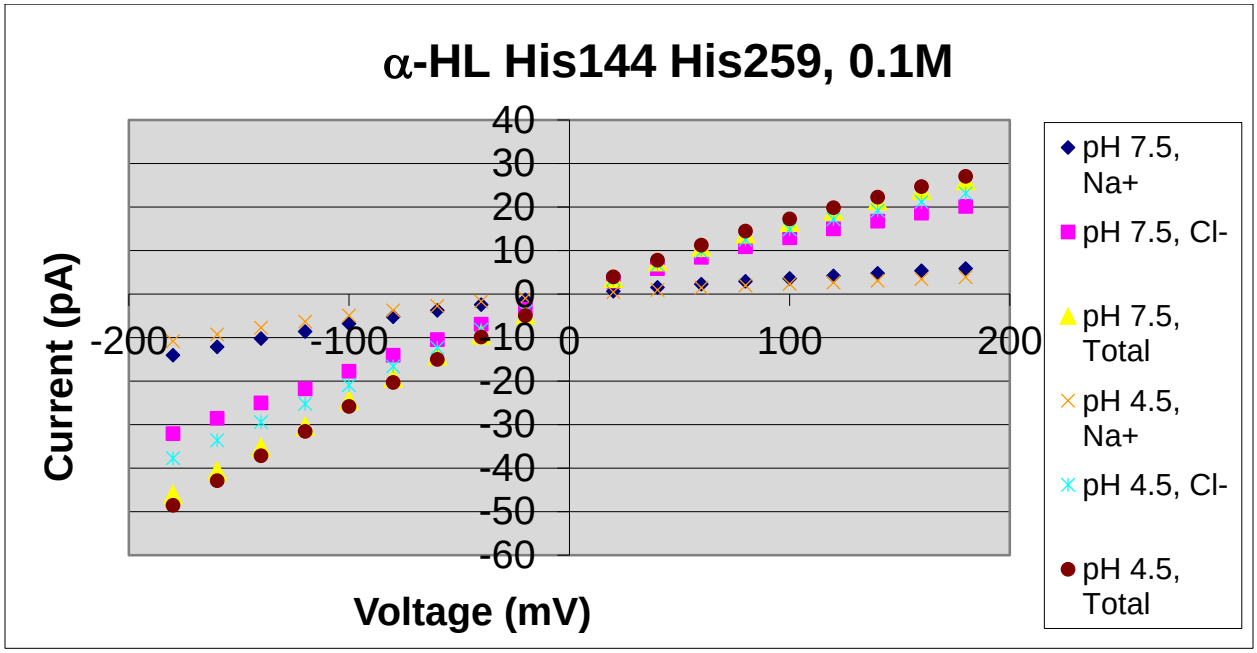


**Figure 3.5:** I-V data calculated using PNP for α-HL, where the charge states of two histidine residues, His144 and His259 are calculated at pH 7.5 and pH4.5 in a symmetric 0.1M NaCl bathing solution. There is marginal shift in selectivity of mobile charge type in this data, suggesting that other titratable residues in α-HL must contribute toward any pH-dependent changes in selectivity.

### 3.3.3 Variable pH bathing solutions

We performed a series of PNP calculations to simulate experimental conditions with variable pH on either side of the membrane. For all following calculations, bathing solutions on both sides of the channel have 1.0M NaCl concentrations, corresponding to the Misakian and Kasianowicz 2003 work. In our PNP calculations we tested whether it required a recalculation of partial charges on titratable residues just at the protein/solvent interface of the α-HL structure or if a recalculation of charge states in the interior of the protein was also required to produce I-V characteristics similar to experimental results. Details of the setup for our calculations are provided in Section **3.2**. The I-V data shown in Figures 3.6 and 3.7 correspond to the cis side of the system being at pH 4.5 and the trans side at pH 7.5. Experimental results for this configuration show that the total current rectification ratio of the system increases to nearly 1.5. PNP results indicate that, if only surface residues on the trans side of the channel shift their protonation state, there is only a marginal increase in current rectification over the symmetric pH 7.5 bath (rectification of approximately 1.37). However, if both surface as well as buried residues shift in charge state corresponding to a pH of 4.5, the current rectification of the system shifts to 1.48. Examining the charge-specific I-V data in Figure 3.7, this overall change in current rectification can be accounted for in that the $Na^+$ current is decreasing at positive voltage biases, while anionic current is increasing at negative voltage biases, further showing that the channel becomes more anion-selective upon recalculation of charge states throughout the structure as the pH is lowered.

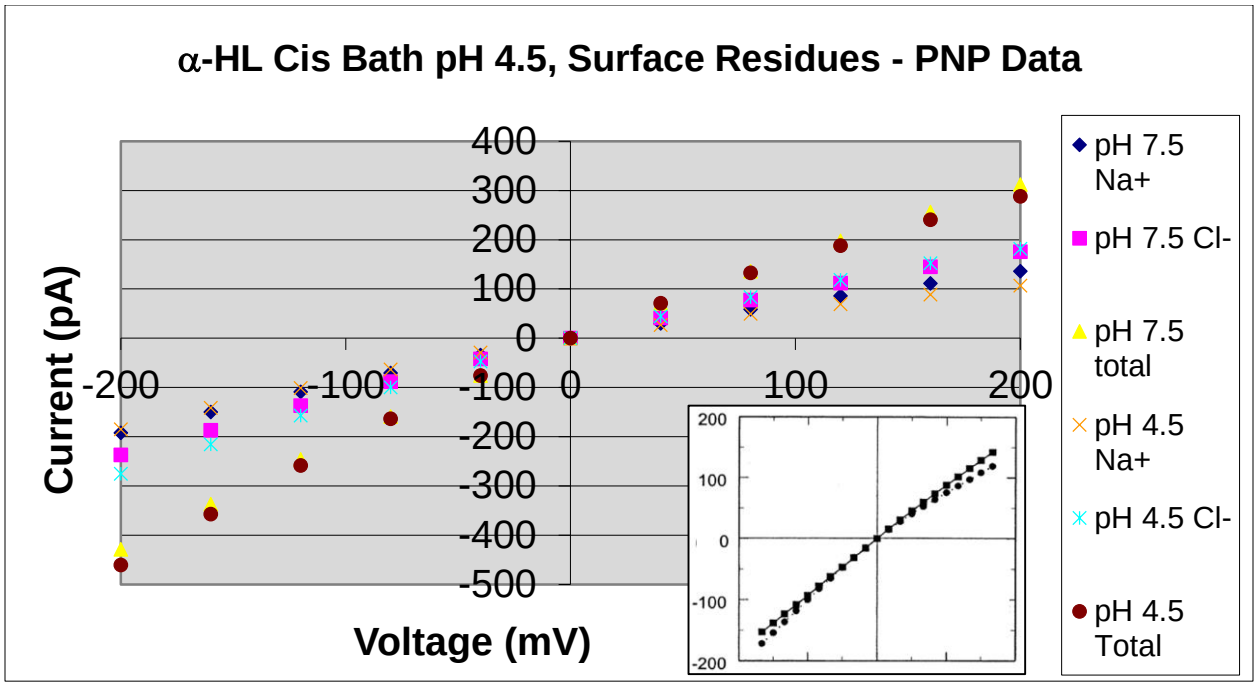


**Figure 3.6:** I-V data calculated using PNP for α-HL in 1.0M NaCl, where the cis bath is at pH 4.5 and the trans bath is at pH 7.5. Charge states of surface residues on the cis side of the channel structure correspond to protonation states calculated at pH4.5, while buried cis residues remain at charge states corresponding to pH 7.5. All residues on the trans side of the channel correspond to charge states corresponding to pH 7.5 **Inset:** Experimental I-V data where bathing solutions have pH values similar to simulated conditions. Squares correspond to both baths at pH 7.5 and circles correspond to cis bath at approx. pH 4.5 (Misakian and Kasianowicz, 2003).

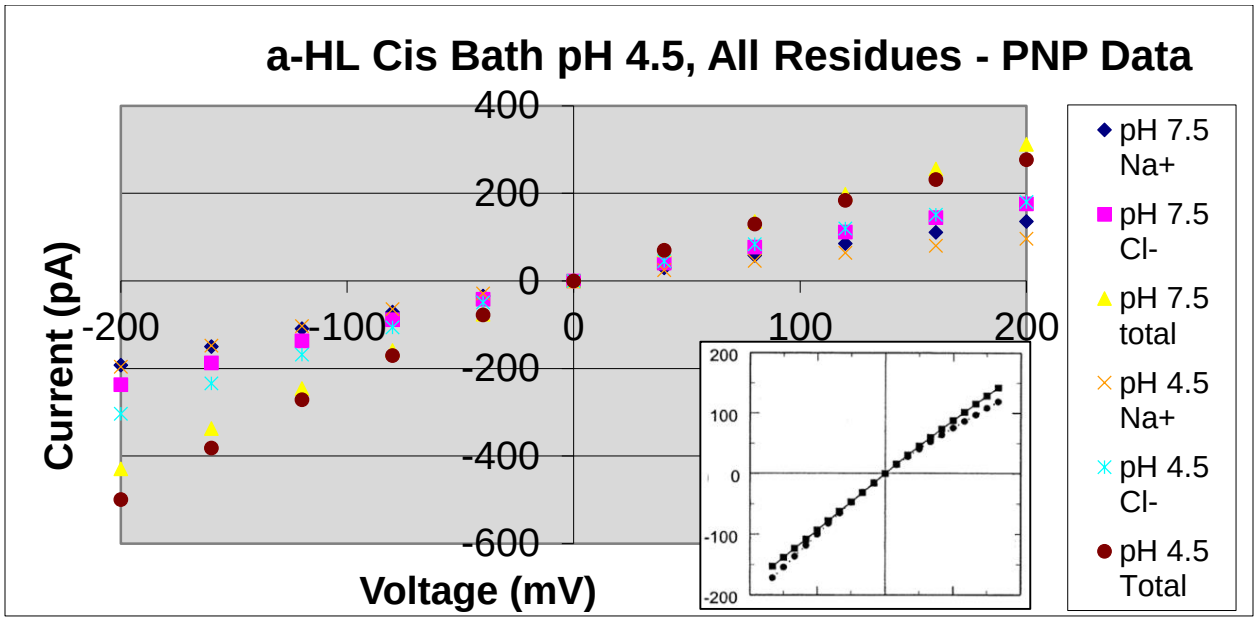


**Figure 3.7:** I-V data calculated using PNP for α-HL in 1.0M NaCl, where the cis bath is at pH 4.5 and the trans bath is at pH 7.5. Charge states of surface as well as buried titratable residues on the cis side of the channel structure correspond to protonation states calculated at pH4.5, while charge states of all residues on the trans side are corresponding to pH 7.5. **Inset:** Experimental I-V data where bathing solutions have pH values similar to simulated conditions. Squares correspond to both baths at pH 7.5 and circles correspond to cis bath at approx. pH 4.5 (Misakian and Kasianowicz, 2003).

Figures 3.8 and 3.9 are PNP results for the reverse bathing pH conditions where the trans bath has a pH of 4.5 and the cis bath has a pH of 7.5. Experimental data show that there is a marked reduction in rectification ratio for this scenario, to a value of approximately 0.90, meaning that the rectification ratio for α-HL has reversed for this asymmetric pH bathing condition. Changing the charge states of only the surface residues (Figure 3.8) results in an I-V curve with nearly symmetric current at positive and negative voltages, i.e. no rectification. Changing the charge states of both surface as well as buried residues results in a rectification ratio that is comparable to experimental results (Figure 3.9) and inspection of the ion-specific current shows that the channel has markedly reduced cationic current at negative voltage biases. This would be an expected observation in that the titratable residues on the trans side of the membrane would become more positively charged at lower pH, and positively charged ions would have a higher energetic barrier to overcome entering the channel from the trans side, resulting in an overall reduction in current at these values.

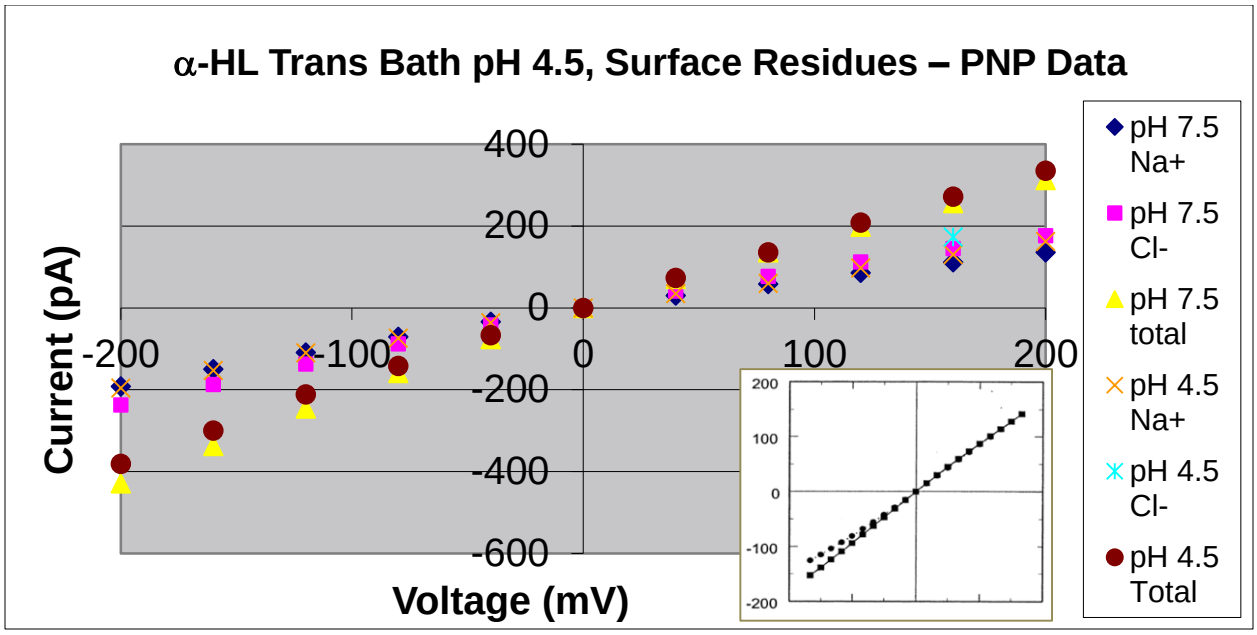


**Figure 3.8:** I-V data calculated using PNP for α-HL in 1.0M NaCl, where the trans bath is at pH 4.5 and the cis bath is at pH 7.5. Charge states of surface residues on the trans side of the channel structure correspond to protonation states calculated at pH4.5, while buried residues remain at charge states corresponding to pH 7.5. All residues on the trans side of the channel have charge states corresponding to pH 7.5. **Inset:** Experimental I-V data where bathing solutions have pH values similar to simulated conditions. Squares correspond to both baths at pH 7.5 and circles correspond to trans bath at approx. pH 4.5 (Misakian and Kasianowicz, 2003).

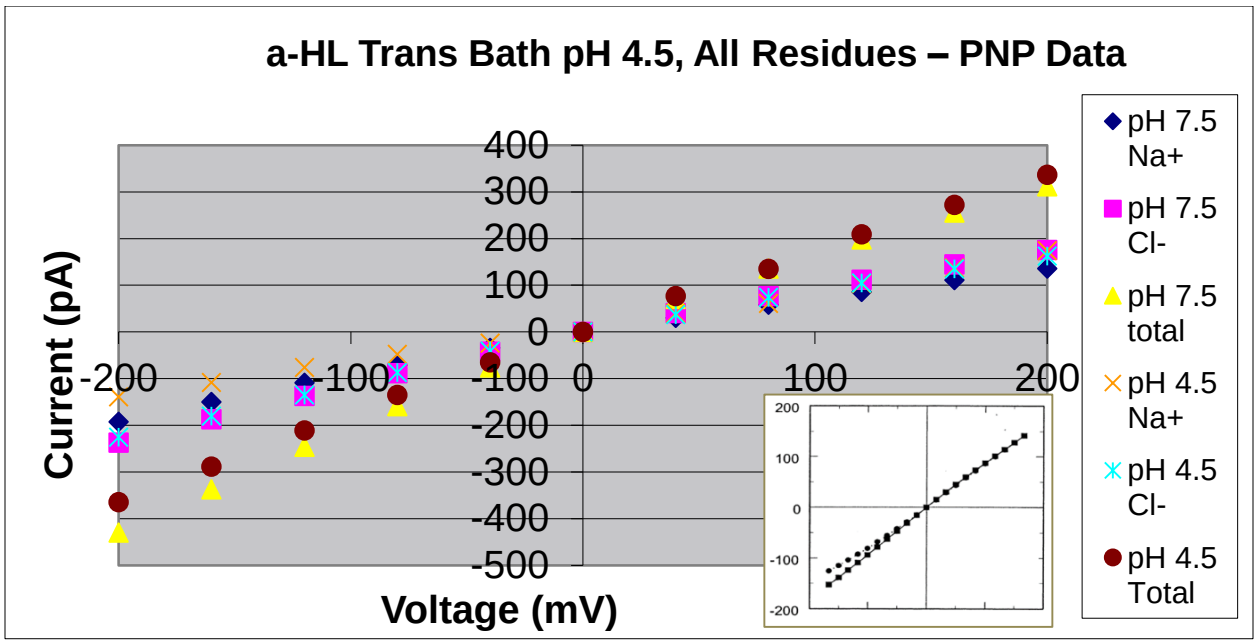


**Figure 3.9:** I-V data calculated using PNP for α-HL in 1.0M NaCl, where the trans bath is at pH 4.5 and the cis bath is at pH 7.5. The charge states of surface and buried titratable residues on the trans side of the channel structure correspond to protonation states calculated at pH4.5, and the charge states of all residues on the cis side are corresponding to pH 7.5. **Inset:** Experimental I-V data where bathing solutions have pH values similar to simulated conditions. Squares correspond to both baths at pH 7.5 and circles correspond to trans bath at approx. pH 4.5 (Misakian and Kasianowicz, 2003).

## 3.4 CONCLUSIONS

This work has shown evidence that the pH-dependent current-voltage behavior of the bacterial ion channel alpha hemolysin is most likely due to changes in the charge states of titratable amino acid side chains, both at the protein-solvent interface as well as within the protein interior. While it cannot be ruled out that overall changes in pore structure contribute to these pH-dependent features, it appears that this channel remains in a relatively stable structural form throughout this range of pH values. Calculating the titratable group pKa values using the software package PROPKA and calculating I-V properties using 3-D Poisson-Nernst-Planck theory resulted in a qualitatively successful comparison with experimental data.

It was noted in section **3.2** that the membrane is uncharged for these calculations. It has been shown that charges on the membrane surface can alter I-V properties of ion channels (Bell and Miller, 1984; Krasilnikov and Sabirov, 1989, Cárdenas et al., 2000). Thus, in future calculations, accounting for the charged head groups of the phospholipid bilayer may be an important factor to consider. Also not considered in this work is that the basic residues Arg200, Lys75, Lys266 and His259 are located on the exterior of the protein, where α-HL meets the phospholipid bilayer (Figure 3.10). For our initial calculations it was a reasonable assumption that these basic residues be considered surface proteins as solute is able to enter this interface. However, because the negatively charged phosphate head groups on the bilayer would favor the presence of positive charges on these residues, it would be useful to recalculate the pKa values for these residues in the presence of a fully atomistic membrane in the calculation.

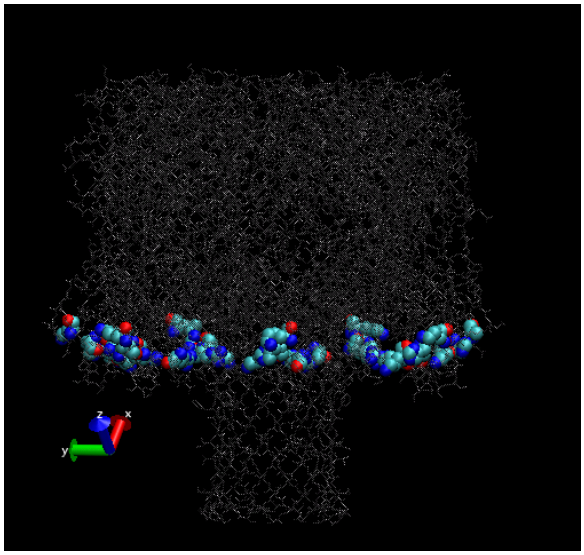

**Figure 3.10:** Numerous titratable amino acid residues, Arg200, Lys75, Lys266, His259, are found at the cap domain of α-HL. The pKa values of these groups would likely be influenced by the presence of charged phosphate groups in the lipid bilayer.

It would be a logical extension of this work to calculate pH-dependent I-V characteristics of a narrower ion channel where the permeant properties of the channel should be more sensitive to charge states of residues within the channel structure, e.g. the ASIC1 channel (Baconguis and Gouaux, 2014). Additionally, our results using PNP to calculate I-V properties of α-HL with modified charges at varying pH values could be verified using other computational methods such as Brownian dynamics and/or non-equilibrium molecular dynamics. In particular, recent developments in NEMD include a method of simulating protonation/deprotonation events of titratable sites according to protonation probability during the course of simulation (Donnini et al., 2016), providing a more realistic treatment of charge states of titratable residues. A simulation using this methodology, as compared to using fixed fractional charges on titratable residues, may provide a useful comparison to our results.

# 4.0 THE ELECTROSTATICS OF A VOLTAGE-DEPENDENT ANION CHANNEL (VDAC): IMPLICATIONS FOR SELECTIVITY AND GATING

The work** presented in this chapter was published in:

Om P. Choudhary, Rachna Ujwal, William Kowallis, Rob Coalson, Jeff Abramson, and Michael Grabe. 2010. Journal of Molecular Biology. 396(3): 580–592.

**Contributions from W. Kowallis consist of PNP simulations, electrostatic calculations of the channel structure, and discussion of overall channel behavior based on results of these calculations.

## 4.1 INTRODUCTION

Voltage-dependent anion channels (VDAC) are the dominant protein in the mitochondrial outer membrane (MOM), where they facilitate the flow of adenosine triphosphate (ATP), adenosine diphosphate (ADP), and other metabolites between the cytosol and the intermembrane space (Schein et al., 1976; Rostovtseva et al., 1997). The efficient flow of materials into and out of the mitochondria is critical to cell survival in all eukaryotic systems, and it is not surprising that VDAC exhibits a large conductance, 0.45-0.58 nS in 0.1 M KCl, compatible with this task (Colombini, 1999). Experiments in reconstituted bilayers have shown that the channel is maximally open at 0 mV and that it enters a lower-conductance state above +30 mV and below -30 mV resulting in a bell shaped current-voltage relationship (Schein et al., 1976). Here, we refer to the high-conductance state as the open state and the lower-conductance state, or possibly states, as the partially closed state. While the open state facilitates the flux of ~ $2\times10^6$ ATP molecules per

second, this value drops to near zero in the partially closed state despite the persistent flow of small ions (Rostovtseva et al., 1997). Additionally, as the name implies, VDAC is weakly anion selective in the open state, but switches to weakly cation selective in the partially closed state (Colombini, 1999).

In addition to its energetic role, VDAC appears to have a more complex purpose, serving as a scaffold for proteins and molecules that modulate mitochondria permeability, and thereby its function (Adams, et al., 1998; Shimizu et al., 1999). This cell death/survival role has implicated VDAC in the metabolic stresses of cancer and cardiovascular disease specifically as well as mitochondrial-dependent apoptotic cell death in general (Galluzi et al., 2008). Thus, the ability to manipulate VDAC's function in a rational manner will have important implications for novel therapeutics to modulate cell survival in different diseases.

In mammals, there are three VDAC isoforms (VDAC1, VDAC2, and VDAC3) with VDAC1 being the prototypical channel common to all eukaryotes. These three isoforms share greater than 80% sequence homology, yet they have distinct physiological roles, electrophysiological properties, relative abundance and distribution between cell types (Sampson et al., 2001; Hinsch et al, 2004; Xu et al., 1999). VDAC2 is the dominant isoform expressed in the brain (Cesar et al., 2004) displaying normal gating patterns relative to VDAC1, but there is an additional population with lower conductance (Xu et al., 1999). VDAC3 is less well characterized but appears to have distinct gating properties and reduced metabolite permeability (Xu et al., 1999). VDAC1 is by far the most well-studied isoform in the family, and many of the fundamental electrophysiological properties including single-channel conductance, selectivity, and voltage dependence, are remarkably conserved across different organisms ranging from yeast to mammals (de Pinto et al., 1987; Colombini, 1989). In spite of this basic conservation, there are species related

differences resulting in some variations when reconstituted in planar phospholipid membranes (Colombini, 1989).

Up until now, direct structural insight into the operation of VDAC has come from low-resolution electron microscopy (EM) (Manella, 1982; Guo et al., 1995) and atomic force microscopy (AFM) (Hoogenboom et al., 2007); however, recently three mammalian structures have been reported (Ujwal et al., 2008; Bayrhuber et al., 2008; Hiller et al., 2008) making it possible to ask unprecedented questions concerning VDAC1's molecular workings. All three structures show that VDAC1 is a β-barrel formed by 19 β-strands with an ~ 3 nm pore diameter in excellent agreement with previous EM (Manella, 1982; Guo et al., 1995) and AFM (Hoogenboom et al., 2007). Mouse VDAC1 (mVDAC1) is the highest resolution structure (2.3Å) revealing an N-terminal helix situated in the pore domain where it adheres to the wall of the barrel (Ujwal et al., 2008). At both mouths, the pore is ~ 27 Å wide, but it narrows to 14 Å near the center of the channel at the helix. The long dimension of ATP is also about 14 Å, which would allow metabolites to pass through the channel sterically unhindered. This observation suggests that mVDAC1 may represent the open state of the channel. However, it is possible that permeation is not controlled through steric interactions, but rather by the electrostatic field in the channel created by the ~ 30 charged residues that line the pore. Structural changes could alter this field thereby drastically altering the permeation properties of ATP and ADP, which carry a formal charge of -4 and -3, respectively. With regard to gating, the helix is flanked by two proline residues on the N- terminal side and three glycine residues at the C-terminal end, making it ideally suited to be a mobile element. The helix position was not resolved in the NMR structure, which is consistent with a high degree of mobility (Guo et al., 1995; Hiller et al., 2008; Stanley et al., 1995). Therefore, it is quite

possible that the N- terminal helix, which has four basic and two acidic residues, is the voltage sensor and metabolite gate as suggested by past work (Colombini et al., 1996; Koppel et al., 1998).

Despite this windfall of structural information, there are still numerous outstanding questions concerning the mechanism by which VDAC1 differentiates between ions, how it conducts ATP at high rates, and how the membrane voltage regulates its conduction state. The most pressing question is whether the latest high-resolution structure represents the open state or the partially closed state of the channel. To better understand VDAC1's biophysical properties, we have carried out a number of continuum electrostatics calculations on mVDAC1. As we describe below, the channel is anion selective, and it has a large single-channel conductance that is most consistent with the open state. A key aspect of any computational model is the ability to address a wide range of experimental data. Continuum electrostatic calculations provide a rapid means to compute the current-voltage characteristics for a number of mutant channels, and our results are in good agreement with experimental trends. The molecular rearrangements that accompany voltage gating are not known. We examined two hypothetical models that involve motions of the N-terminal helix, and our calculations indicate that neither motion fully accounts for the channel's observed voltage sensitivity. Thus, we were able to rule out some of the proposed molecular motions, but to gain an understanding of the true mechanism will require extensive probing by a number of different techniques.

## 4.2 RESULTS

### 4.2.1 Cation and anion energy profiles suggest that the mVDAC1 structure is open

The mVDAC1 structure has been proposed to be in an open conformation (Ujwal et al., 2008), which is known to be anion selective. We wanted to quantitatively probe this claim by determining if ion passage through the channel was more conducive to anions or cations. Poisson- Boltzmann (PB) electrostatic calculations are a fast, effective way of calculating such ion transfer free energies and for understanding the role of the protein architecture in the process (Roux and MacKinnon, 1999; Grabe et al., 2006). We computed the energy required to transfer a chloride-sized monovalent anion from bulk water through the central pore of mVDAC1. The total free energy of transfer consists of a Born solvation term, which corresponds to stripping waters away from the ion as it passes through the channel, and an electrostatic term, which corresponds to the interaction of charges on the channel with the charge on the ion. The proximity of the ion to the low dielectric of the membrane could drastically affect the permeation energetics, so we embedded the channel in a water-impermeable, uniform slab of dielectric 2, which closely mimics the properties of the membrane.

The geometry of the system is depicted in Figure 4.1c,d. The ion (green sphere) was translated from -40 Å to +40 Å, and the total electrostatic energy was calculated every 1 Å. The channel was centered at the origin, and z = 0 and ±20 Å are indicated by arrows in panel C. While included in all of the calculations, the membrane is not pictured but its extent is indicated by grey bars in Figure 4.1c. Our choice of orientation along the z-axis is arbitrary since the orientation of VDAC in the membrane is still under debate (see below). For consistency, we define the negative

direction to be the side of the membrane that contains the N and C-termini. This convention is held throughout.

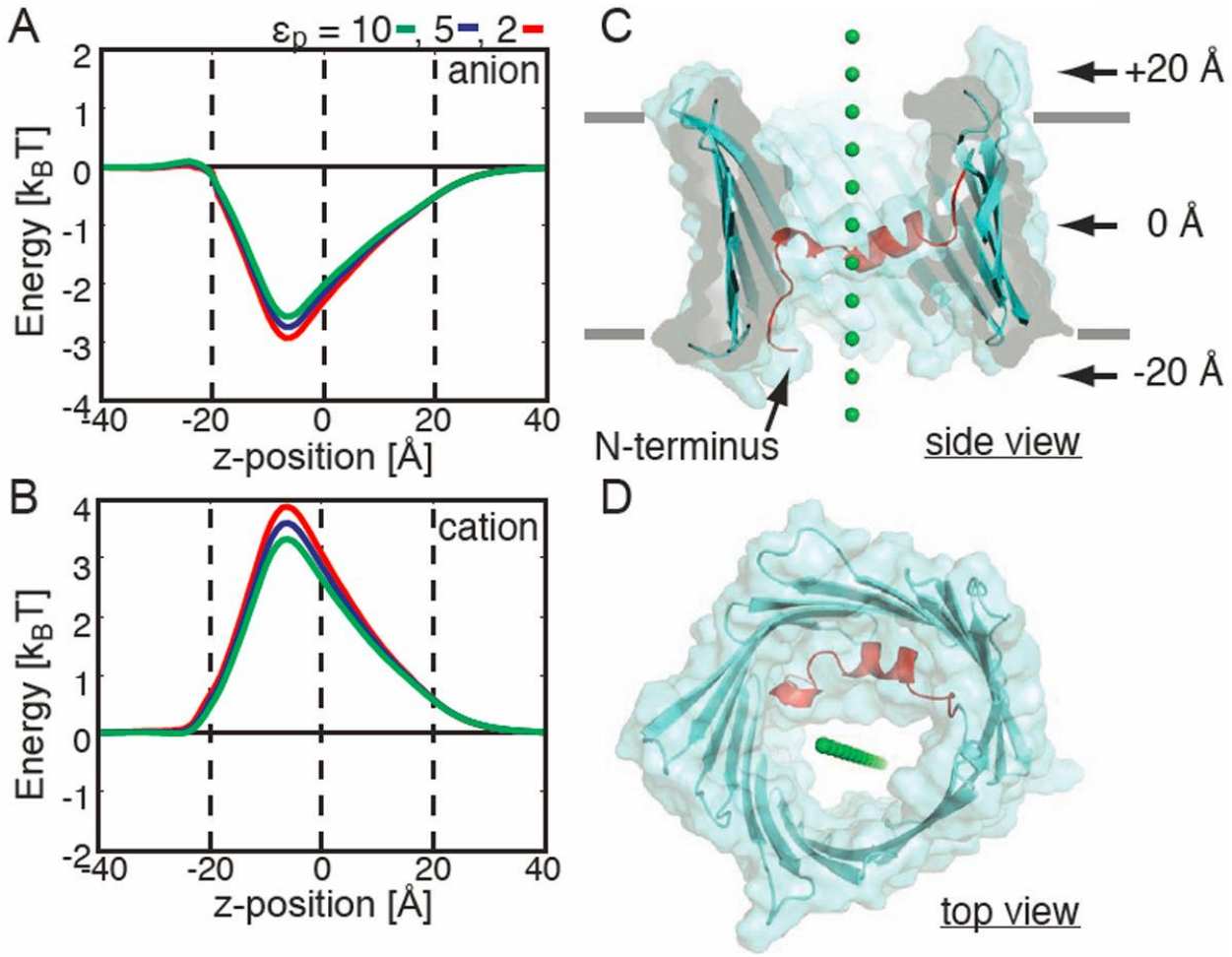


**Figure 4.1:** mVDAC1 is selective for anions. Ion transfer free energies calculated through mVDAC1 for a chloride-sized anion (a) and a potassium-sized cation (b). Energies were calculated using the Poisson-Boltzmann equation after embedding mVDAC1 in a low dielectric, εm= 2, slab corresponding to the membrane. The path for both ions through the channel is pictured in panels c (side view) and c (top view). Varying the protein dielectric constant, εp, had little effect on the free energy profiles. For all calculations, z = 0 corresponds to the center of the channel, and the channel extends from -20 to +20 Å. These positions are indicated by dashed lines in panels a and b.

We see from the set of curves in Figure 2.1a that the transfer free energy is energetically favorable resulting in a ~ 2.5 kBT stabilization of the anion when it is at z = -7.5 Å (1 kBT ~ 0.6 kcal/mol at room temperature). Interestingly, the profile is not symmetric with respect to the center of the channel. The N-terminal helix occupies the lower half of the channel very close to the energy

minima. It is generally thought that the dielectric constant of protein ranges from 2 to 20 (Cohen et al, 2002), but it is also understood that proteins are heterogeneous (Schutz and Warshel, 2001). We explored the effect of the choice of protein dielectric constant, $\varepsilon_p$, on our results by varying it from 2 to 10. Paradoxically, increasing the protein dielectric value destabilizes the negative ion by 0.5 kBT (red curve compared to green curve in panel a). While this is only a small change, it results from the decreased electric field in the center of the channel that accompanies increasing the protein dielectric value. In Figure 4.2a, we show that the membrane has very little effect on the permeation energetics since the ion remains surrounded by a significant amount of water during penetration due to the large pore size.

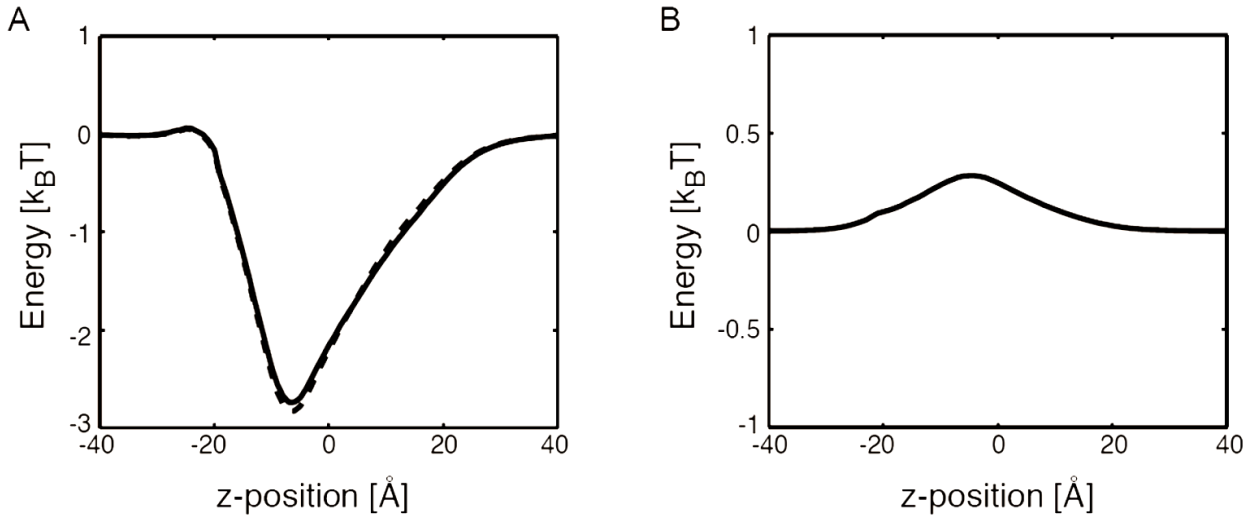


**Figure 4.2:** Protein charges dominate the ion transfer free energy. (a) Ion transfer free energy profiles through mVDAC1 for a chloride-sized anion in the absence (dashed curve) and presence (solid curve) of the membrane. The membrane has very little effect on the permeation energetics. (b) Born solvation energy for anion permeation. The energy peaks near the N-terminal helix (-7.5 Å) at 0.25 kBT. Such a small value indicates that ions remain largely solvated during the transfer from one side of the pore to the other. Panels a and b indicate that the electrostatic interactions of the permeant ions with the permanent charges on mVDAC1 dominate the ion transfer free energy. In both panels that protein dielectric, $\varepsilon_p$, was set to 5.

Next, we carried out all of the free energy calculations using a potassium-sized monovalent cation. Interestingly, the channel presents a free energy barrier to cation movement (Figure 4.1b).

The maximum energy difference between the curves in panel A and B is 5.5-7 kBT, which is energetically significant and shows that the channel is selective for anions. This result corroborates the claim that the x-ray structure is indeed the open state (Ujwal et al., 2008), and that it is not the cation-selective partially closed state. The anion and cation energy profiles in panels A and B are nearly mirror opposites of each other suggesting that the Born solvation energy is very small, which we verified in separate calculations in Figure 4.2b. Therefore, the free energy profile is dominated by the electrostatic interaction with charged groups on the channel. For a narrow pore like the KcsA potassium channel, the Born solvation term is very important since all the water molecules are essentially stripped away during translocation (Rous and MacKinnon, 1999). In our case, the pore is large enough that ions can retain their hydration shell as they move through the channel resulting in a negligible Born energy.

### 4.2.2 The permeation energetics of mutant channels is in accord with experimentally measured changes to selectivity

VDAC has an open-state chloride to potassium ion selectivity ratio of 1.7-1.9 in a 1.0 M to 0.1 M asymmetric salt gradient (Colombini, 1989). These selectivity values are modest compared to ion channels like the Shaker voltage-gated potassium channel (1000:1) (Hille, 2001), which has a selectivity filter – a narrow stretch made up of a handful of residues responsible for selecting one ion over another via interactions of the carbonyl backbone with the permeating ion (Doyle et al., 1998). Blachly- Dyson and co-workers showed that mutations throughout the primary sequence of VDAC from Saccharomyces cerevisiae (scVDAC1) could affect channel selectivity and the largest changes involved charge mutations (such as lysine to glutamic acid) (Blachly-Dyson et al.,

1990). Additionally, the effects from multiple mutations were additive, which is suggestive of an electrostatic mechanism in which the electric fields from multiple residues add linearly at the site of the permeating ion. This mechanism is in stark contrast to those of potassium channels, which are believed to depend on the details of packing geometry and fluctuations of the channel around the ion (Valiyaveetil et al., 2006; Noskov et al., 2004).

We investigated those residues that were previously shown to contribute to anion selectivity. Blachly-Dyson et al. carried out site directed mutagenesis and identified 14 sites that affect selectivity and 12 that, when mutated, showed little or no change in selectivity (Blachly-Dyson et al., 1990). We aligned mVDAC1 to scVDAC1 and found that 11 of the 14 residues implicated in selectivity are on the bottom half of the channel (the overall sequence identity is 25% and the sequence similarity is 51%). Interestingly, the bottom half of the channel is the most favorable location for anions in the pore as shown by the energy minimum in Figure 4.1a. As can be seen in Figure 4.3c, we made in silico mutations to some of the homologous residues in mouse VDAC1 using VMD (Humphrey et al., 1996), and then we recalculated the free energy of ion transfer to compare against calculations on the wild-type structure.

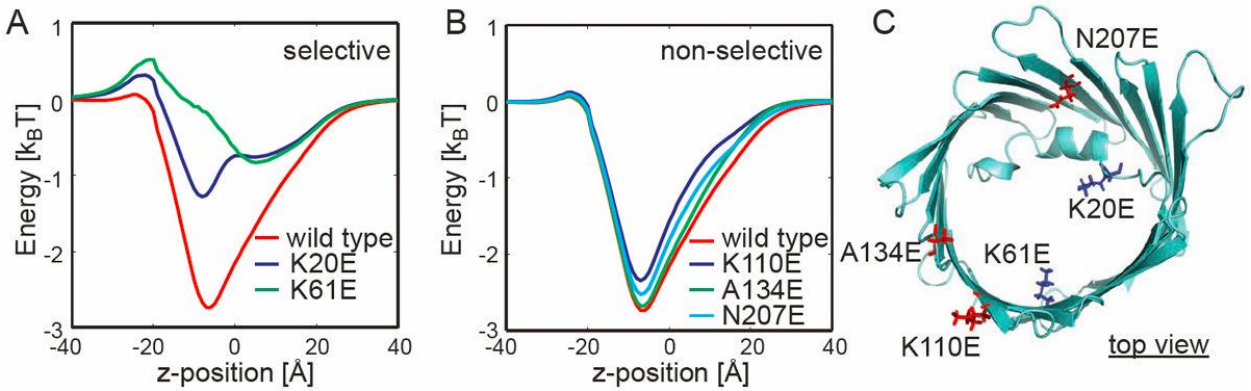


**Figure 4.3:** Altered ion transfer free energies through mVDAC1 match measured changes to selectivity. (a) Free energy profile for a chloride anion moving through the wild-type (red) and two mutant channels: K20E (blue) and K61E (green). K20E and K61E significantly destabilize the anion in the channel, and this is consistent with experimental measurements. (b) Mutations K110E, A134E, and N207E have little effect on the free energy profile, which is in excellent agreement with experiment. (c) All residues are pictured. The selective positions (blue) are much closer to the permeation pathway, while the nonselective positions (red) are farther away.

Experimentally, mutating scVDAC1 residues K19E (meaning mutating lysine, at residue 19 in the structure, to glutamic acid) or K61E elicits changes in the reversal potential, which is directly related to a decrease in the channel's selectivity (Table 4.1). We mutated the corresponding residues in mVDAC1, K20E, and K61E, and plotted the change in the free energy profile compared to wild type (Figure 4.3a). The changes in the free energy profile are striking. The free energy minimum near -7.5 Å is decreased by 1.5 and 2.5 kBT relative to the wild-type curve (red) for K20E (blue) and K61E (green), respectively. Moreover, both mutations present a slight barrier to permeation along the chosen path at z =-20 Å.

Summary of mutant channel properties.

| Mutation (*S. cerevisiae*) | Mutation (Mouse) | $\Delta V_{rev}$ [mV] (ref. (27)) | $\Delta V_{rev}$ [mV] (Fig. 5A) | $\Delta V_{rev}$ [mV] (Fig. 5B) | $\Delta\Delta G$ [$k_BT$] (Fig. 3) |
|---|---|---|---|---|---|
| K19E | K20E | -12.3 | -6.4 | -7.0 | 1.5 |
| K61E | K61E | -8.4 | -4.1 | -5.5 | 2.6 |
| K19E/K61E/K95E | K20E/K61E/K96E | NA | -13.4 | -19.0 | NA |
| K108E | K110E | -0.8 | -2.5 | -0.8 | 0.4 |
| K132E | A134E | -0.1 | -1.4 | ~ 0.0 | 0.2 |
| K205E | N207E | -1.0 | -1.8 | -0.3 | 0.05 |

**Table 4.1:** We considered 3 mutations that affected selectivity (green) and 3 that did not (blue). The original mutagenesis was carried out on scVDAC1, and we present the homologous mouse VDAC1 residues mutated for the present study. The change in reversal potential, ΔVrev, under 1.0 M to 0.1 M KCl conditions are based on experiments from Sampson et al., 2001, PNP calculations with the channel orientation in Figure. 4.5a, and PNP calculations with the orientation in Figure 4.5b. While Blachly-Dyson et al., 1990 studied K19E, K61E, and K95E separately, the triple mutant was not studied; hence, this value is listed as not available (NA). The final column is the change in the minimum energy for the mutant channels compared to the wild-type channel based on the transfer free energies in Figure 4.3.

Blachly-Dyson and co-workers also reported 12 non-selective sites where mutating basic residues to acidic ones, or vice versa, had little effect on the channel's selectivity. Our electrostatic calculations on a few of the corresponding mouse mutants (K110E, A134E, and N207E) resulted in very small changes to the free energy profile, less than 0.4 kBT in each case (Table 4.1). All of the ion transfer free energies in Figure 4.3b are very similar to the wild- type curve indicating that these mutations do not alter the biophysical properties of the channel. Thus, our calculations, like the experiments, show that these residues play a minor role in VDAC1 selectivity.

### 4.2.3 Electrostatic calculations identify anion and cation pathways through the channel

The ion paths shown in Figure 4.1 were chosen as straight lines that passed approximately through the middle of the channel. However, the pore is wide, and it is likely that the local electric fields guide anions and cations along different paths that are not straight. PB calculations were used to determine the electric field in the pore, and in Figure 4.4, the potential contours were plotted at different heights along the channel: z = +10 Å (panel A), 0 Å (panel B), and -10 Å (panel C). Contours were drawn in 35 mV intervals between -35 mV and 70 mV. At all levels, the pore is dominated by positive potentials showing that the respective anion and cation transfer free energies along single paths in Figure 4.1 are representative of the true energetics of ion permeation. For instance, at z = -10 Å the potential is 70 mV or greater throughout 90% of the pore indicating that the anion minimum and cation maximum in Figure 4.1 are present for nearly all paths through the channel. For reference, a 60-75 mV potential corresponds to a 2-3 $k_BT$ energy for a monovalent anion at room temperature, in excellent accord with the values in Figures 4.1-3. Interestingly, panels A and B indicate that cations will flow along the side of the channel opposite the helix (negative y values), while anions will occupy a larger space closer to the helix (positive y values). The 0 mV contour forms the dividing line between favorable and non-favorable positions for both types of ions.

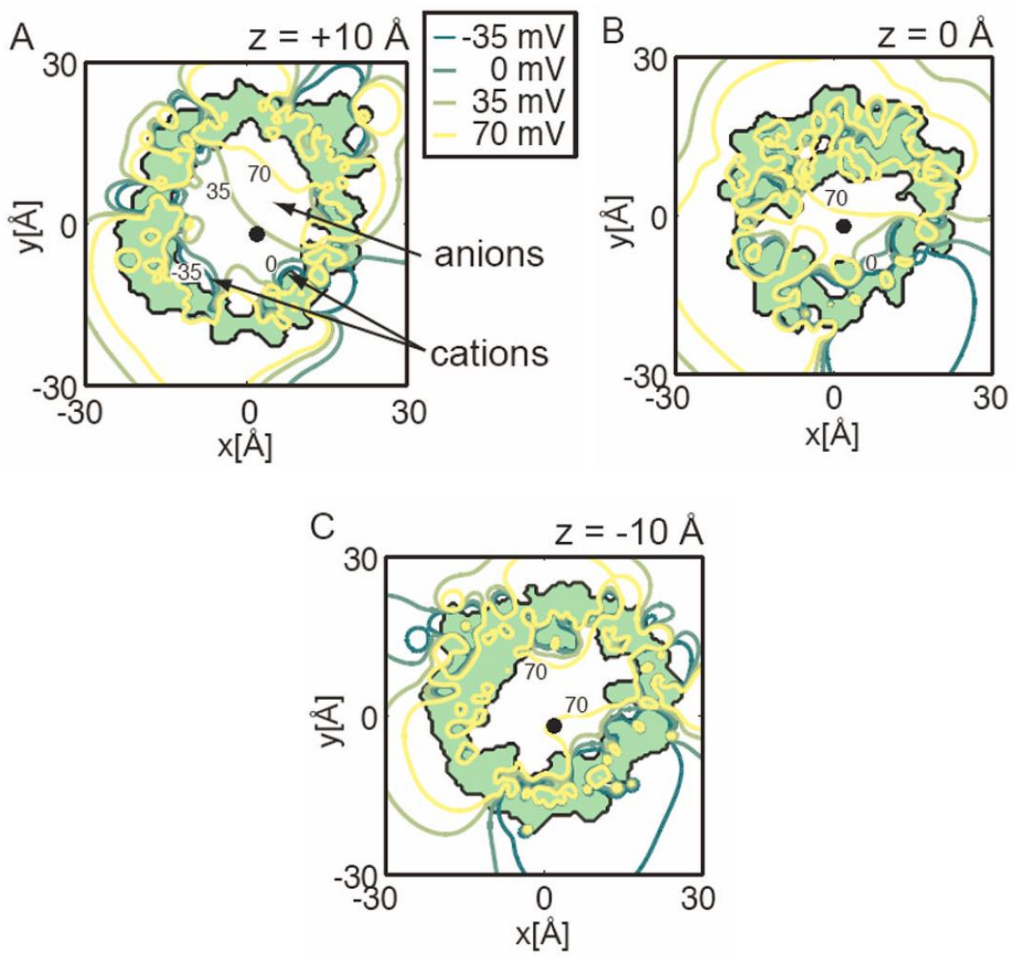


**Figure 4.4:** The electrostatic potential at three different heights in the pore. The potential contours due to the protein charges were calculated as in Figure. 4.1 and then plotted at z = +10 Å (A), z = 0 Å (B) and z = -10 Å (C). Each view is along the pore's long axis, and the protein interior is shaded light green. The ion path used for all calculations in Figures 4.1-3 is indicated by a black dot in each panel. Five equally spaced isocontours were chosen with the blue representing negative potential values and the red values representing more positive values. The contour at 0 mV is indicated in panels a and b, while the +70 mV contour is shown in each. The 0 mV contour divides the region favorable to anions (positive values at positive y values) and cations (negative values at negative y values). The pore is dominated by positive potential values at all heights, especially at z = -10 Å. The ion path falls along contour values that are representative of the average value at each height. At z = +10 Å the value is ~ +30 mV, near the middle of the full range of values. In panel B, the positive potentials occupy more of the cross-sectional area, and the electrostatic potential at the ion pathway increases to +50 mV. In panel c, close to the N-terminal helix, the potential is entirely positive. This is in accord with the anion free energy minimum and cation barrier observed in Figure 4.1a,b.

### 4.2.4 PNP theory suggests a large single-channel conductance most compatible with the open state

Relating our calculated changes in ion free energy profiles to changes in selectivity is not straightforward; however, a change of more than 1 $k_BT$ should bring about a macroscopic change in measured currents. To probe aspects of conductance and selectivity more deeply, we turned to a related continuum approach known as Poisson-Nernst-Planck (PNP) theory. PNP computes the steady state concentration profiles of each ionic species based on the net electrical potential distribution, which depends in a self-consistent manner on the ion concentration profiles. From the computed concentration profiles, the ionic flux through the channel in different physiological conditions can be calculated (Kurnikova et al., 1999). Since the ionic concentration profiles are 3-dimensional densities, these calculations do not suffer from picking a single arbitrary pathway, but rather the ions occupy the most favorable positions in the pore during permeation.

We first calculated the ionic flux through wild-type mVDAC1 for a wide range of voltages in symmetric salt conditions corresponding to a 0.1 M KCl solution. Throughout this work, all membrane voltages refer to the value in the lower bath with respect to the upper bath. The current-voltage relation predicted a single-channel conductance of 1.06 nS, and the experimental open-state value is 0.45-0.58 nS in 0.1 M KCl (Colombini, 1989). It has been found from previous studies that PNP theory yields conductance values that are typically 1.5-2 times higher than experimental values for large pores (Im and Roux, 2002; Noskov et al., 2003). Therefore, given the limitations of this theory, our calculations again suggest that mVDAC1 resides in the open state.

### 4.2.5 A closer look at VDAC1 selectivity

Next, we solved the PNP equations under asymmetric conditions with the 0.1 M KCl in the upper bath and 1.0 M KCl in the lower bath. In this situation, a net current will result if the channel selects one ion type over the other. The applied voltage required to oppose this current is termed the reversal potential, and it is a direct measure of the channel's selectivity (Hille, 2001). The solid black curve in Figure 4.5a shows that mVDAC1 is indeed anion selective as suggested by the curves in Figure 4.1. The reversal potential is 11.9 mV, and the ratio of the anion to cation conductance is about 1.75. This is in excellent agreement with the experimental value of 10.2 mV determined for scVDAC127. Since the charges on the channel are asymmetric, it is possible that the channel's selectivity could depend on its orientation in the membrane. This concern is particularly relevant since the orientation of the channel in the MOM is debated (Stanley et al., 1995; de Pinto et al., 1991; McDonald et al., 2009). We flipped the channel in the membrane and recalculated the current-voltage curve (solid black curve in Figure 4.5b). In this configuration, the reversal potential increases to 14.1 mV indicating a slight gain in anion selectivity. Thus, mVDAC1 is more selective when the energy minimum in Figure 4.1a is facing the low concentration bath, but what this means for channel function in the MOM is difficult to say at this time.

We also calculated the current-voltage curves for the point mutants investigated in Figure 4.3 using both channel orientations. These curves are plotted on the respective panels in Figure 4.5. Both K20E and K61E produced a leftward shift in the reversal potential indicating that they reduce the channel's anion selectivity (red curves in both panels); however, these changes are more pronounced for the orientation in panel B. Our calculations predict that K20E evokes a shift 1.5 times larger than K61E, and this is exactly what is observed experimentally (Blachly-Dyson et al.,

1990). In general, K110E and A134E produced small changes in the reversal potential, as observed experimentally, but there are orientation dependent differences (see Table 4.1). One should note that the homologous sites for A134 and N207 in scVDAC1 are K132 and K205, so acidic substitution results in an overall change in charge of -2, but only -1 for the present calculations. This difference will have very little effect on the reversal potential shifts reported using the orientation in Figure 4.5b, but it would make the shifts calculated using the configuration in Figure 4.5a even larger. Finally, we wanted to convert mVDAC1 into a cation-selective channel. We created a triple mutant channel, K20E/K61E/K96E, based on three of the highest impact mutations identified by Blachly-Dyson and coworkers (Blackly-Dyson et al., 1990). As can be seen from the blue curves in Figure 4.5a,b, this hypothetical channel has a negative reversal potential showing that we were able to convert the anion channel into a cation channel through electrostatic manipulation of the pore residues. An obvious test of our modeling efforts would be to create and experimentally measure the reversal potential of this mVDAC1 mutant channel.

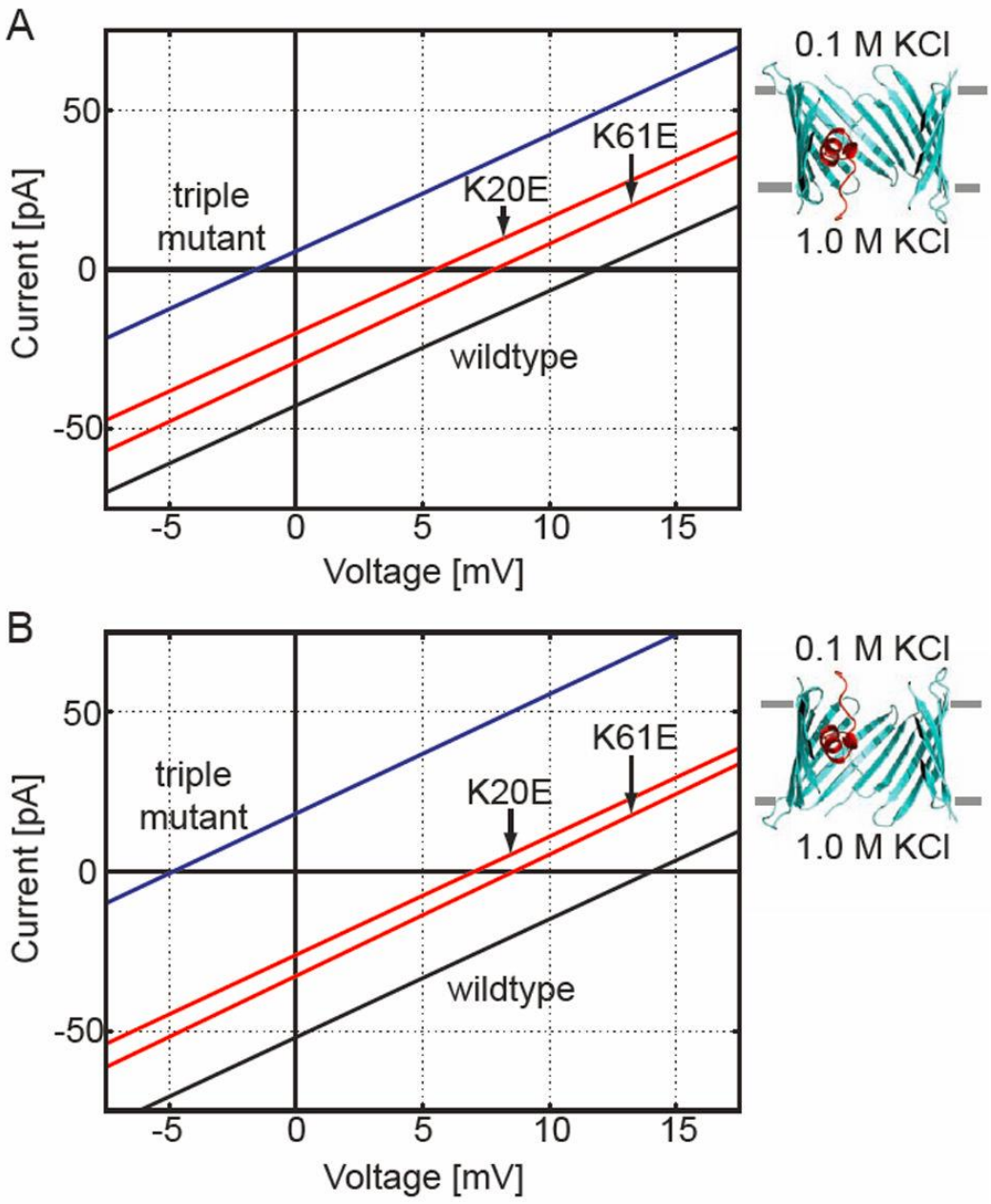


**Figure 4.5:** Wild-type and mutant current-voltage curves calculated using PNP theory. The upper bath was held at 0.1 M KCl and the lower bath at 1.0 KCl. The applied voltage is the value in the lower bath relative to the upper bath. Under these conditions, positive reversal potentials indicate that the channel is anion selective. (a) The channel was embedded in a dielectric slab with the N and C-termini facing the lower solution. The black line is the wild-type curve, and the red curves correspond to K20E and K61E. The leftward shift of both red curves indicates that both mutants reduce the anion selectivity of mVDAC1. The blue curve corresponds to the K20E/K61E/K96E triple mutant. This curve has a negative reversal potential indicating that the channel has been engineered to be cation selective. (b) The orientation of the channels in the membrane were reversed compared to panel A. In this case, the N and C-termini face the upper bath. Interestingly, the reversal potentials are all shifted compared to those in panel A demonstrating that the channel's selectivity depends on its orientation in the membrane.

### 4.2.6 What is VDAC1's voltage sensor and how does it move?

Next, we hoped to gain deeper insight into the operation of mVDAC1 by considering the gating motion and its dependence on membrane voltage. Voltage biases VDAC between an open state that allows ATP passage and a partially closed state that does not (Restovtseva and Colombini, 1997). Moreover, the channel becomes slightly cation selective in the closed state (Colombini, 1989). Several studies imply that VDAC1's voltage sensor is the N-terminal helix (Guo et al., 1995; Colombini et al., 1996; Koppel et al., 1998) while other studies indicate that the residues involved in gating are distributed throughout the primary sequence (Song et al., 1998). Our work above suggests that the mVDAC1 structure represents the open state. If this is true, how does the channel rearrange to occlude ATP passage? To our knowledge, the most specific gating models involve movement of the N-terminal helix, but even within this subclass of models, the degree of motion and exact molecular position of the helix is highly debated (Guo et all, 1995; Manella et al., 1998; Ujwal et al., 2008). We used computational methods to ask whether N-terminal helix movement could account for the channel's voltage sensitivity and changes in ion selectivity.

A signature of the closing motion is the 'gating charge' or 'sensor valence' associated with the movement. The sensor valence is equal to the fraction of the membrane electric field that the charges on the voltage sensor pass through during gating. 1 charge moving through the entire membrane electric field would contribute a valence of 1, but since the voltage-sensor charges need not pass through the entire field this value often takes on non-integer values. The voltage dependence of the channel is directly proportional to its valence, with a high sensor valence corresponding to a steeply voltage-dependent protein. The valence of the VDAC voltage sensor varies slightly with the subtype, but it is estimated to be between 2.5 and 4.5 charge units based

on single-channel recordings (Colombini, 1989; Hiller et al., 2008) compared to 12-14 for Shaker voltage-gated potassium channels (Schoppa et al., 1992).

We considered two hypothetical gating motions that have been suggested in the literature. First, looking at the surface representation of mVDAC1 along the channel axis, as in Figure 4.1d, it is clear that an ATP molecule can pass through the channel sterically unhindered (Törnroth-Horsefield and Neutze, 2008; Ujwal et al., 2008). However, moving the N-terminal helix into the center of the pore would obstruct this pathway. Ujwal and co-workers proposed a hypothetical partially closed state model in which the N-terminal helix was rigidly rotated by pivoting about the C-terminus of the helix just before the beginning of the first β-strand (Ujwal et al., 2008). While this movement is speculative, electrostatic interactions between the N-terminal helix and charged residues on the wall of the β-barrel opposite the helix might account for such a rearrangement. These two states can be seen in Figure 4.6a. The theory for using continuum electrostatic calculations to determine the voltage-dependence of such movements was developed previously (Roux, 1997). Briefly, a modified PB equation is solved to account for the transmembrane potential, and a series of calculations are carried out to isolate the interaction energy of the charges on the protein with this field (Roux, 1997). Several studies have applied this theory to particular channels (Islas and Sigworth, 2001; Chanda et al., 2005; Grabe et al., 2004), and here we implement the procedure using the electrostatics package APBS (Baker et al., 2001) to determine the sensor valance of this motion (gating motion 1). Figure 4.6c shows the energy difference between the hypothetical state and the starting x-ray structure, $\Delta E = E_{hypo.\ state} - E_{mVDAC1}$. This is only the energy difference due to the interaction of the protein charges with the membrane electric field. The switch between the states in panel A shows absolutely no voltage dependence (blue curve in Figure 4.6a). The slope of this line determines the corresponding

voltage-sensor valence, which is ~ 0 in this case. This strongly supports the notion that gating motion 1 is not correct. Second, N-terminal antibody studies on native MOM indicate that gating involves the helix exiting the β-barrel (Colombini, 1989, Manella, 1998), so we considered a second motion (gating motion 2) in which the helix moves into the upper bath as pictured on the right side of Figure 4.6b. This situation is equivalent to removing the helix from mVDAC1 since the electrostatic potential of the outer bath is nearly zero everywhere. Figure 4.6c shows that positive potentials stabilize the helix in the outer bath whereas decreasing the membrane potential stabilizes the x-ray crystal structure (red curve). This happens because the helix has a net charge of +2. Decreasing the membrane potential from +50 to -50 mV results in a 6 $k_BT$ stabilization of the x-ray structure compared to the hypothetical state. The sensor valence of gating motion 2 is only 1.5, which is again too weak to be the true motion, but it could form part of the motion as discussed below (Colombini, 1989; Hiller et al., 2008).

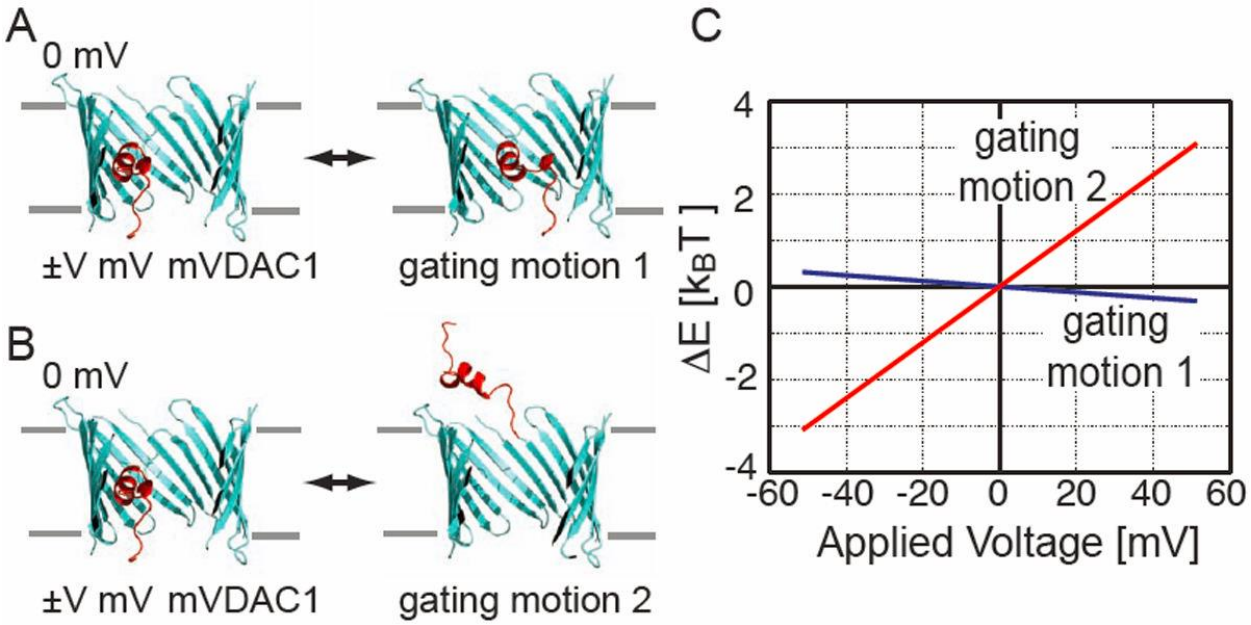


**Figure 4.6:** Voltage dependence of the mVDAC1 x-ray structure compared to two hypothetical gating motions. (a) mVDAC1 is pictured on the left and a hypothetical partially closed state suggested by Ujwal et al., 2008 is on the right (gating motion 1). (b) mVDAC1 is pictured on the left and the N-terminal helix (red) has been removed from the pore on the right (gating motion 2). (c) Poisson-Boltzmann calculations were carried out to determine the membrane potential's contribution to the energy difference between these sets of structures ($\Delta E = E_{hypo.\ state} - E_{mVDAC1}$). The outer bath was held at 0 mV and the inner bath was varied from -50 to +50 mV. To represent the hypothetical state in panel b, the helix was deleted from mVDAC1 as discussed in the text. The energy difference between the states in a is represented by the blue curve, and the difference between the states in b is represented by the red curve. Gating motion 1 shows no voltage dependence, while gating motion 2 has a voltage-sensor valence of 1.5.

### 4.2.7 The hypothetical closed states are still anion selective

We showed in Figure 4.6 that the hypothetical gating motions do not generate the observed gating charge; however, a second additional property of the closed state is whether it is cation selective. To determine this, we computed the electrostatic potential in the pores at two different z values (-3 and +10 Å). Figure 4.7a,b shows that the protein interior (light green) is identical for both models at the outer slice; however, the pore of hypothetical closed state 1 is noticeably more positive (left panel) suggesting that it would be more anion selective. At the inner slices, we can see that the helix occupies the pore in the Ujwal model (panel C), but that the pore is less obstructed

in hypothetical closed state 2 (panel D). As with the x-ray structure, positive potentials dominate at the inner slices for both models. These positive values are due in part to the preponderance of basic residues lining the inner half of the β-barrel.

PNP calculations carried out on the hypothetical closed states show that they are both anion selective (solid lines require positive voltages to stop ion flow in Figures 4.7e,f). In accord with the electrostatic potentials, hypothetical closed state 2 is less anion selective than state 1 and the mVDAC1 x-ray structure. Moreover, the conductance of state 2 is greater than hypothetical closed state 1 and the mVDAC1 structure as indicated by the steeper current-voltage curve. This is to be expected since model 2 no longer has the helix occupying the pore domain. Thus, these hypothetical models fail to reproduce the selectivity, voltage dependence, and conductance changes required for the closed state.

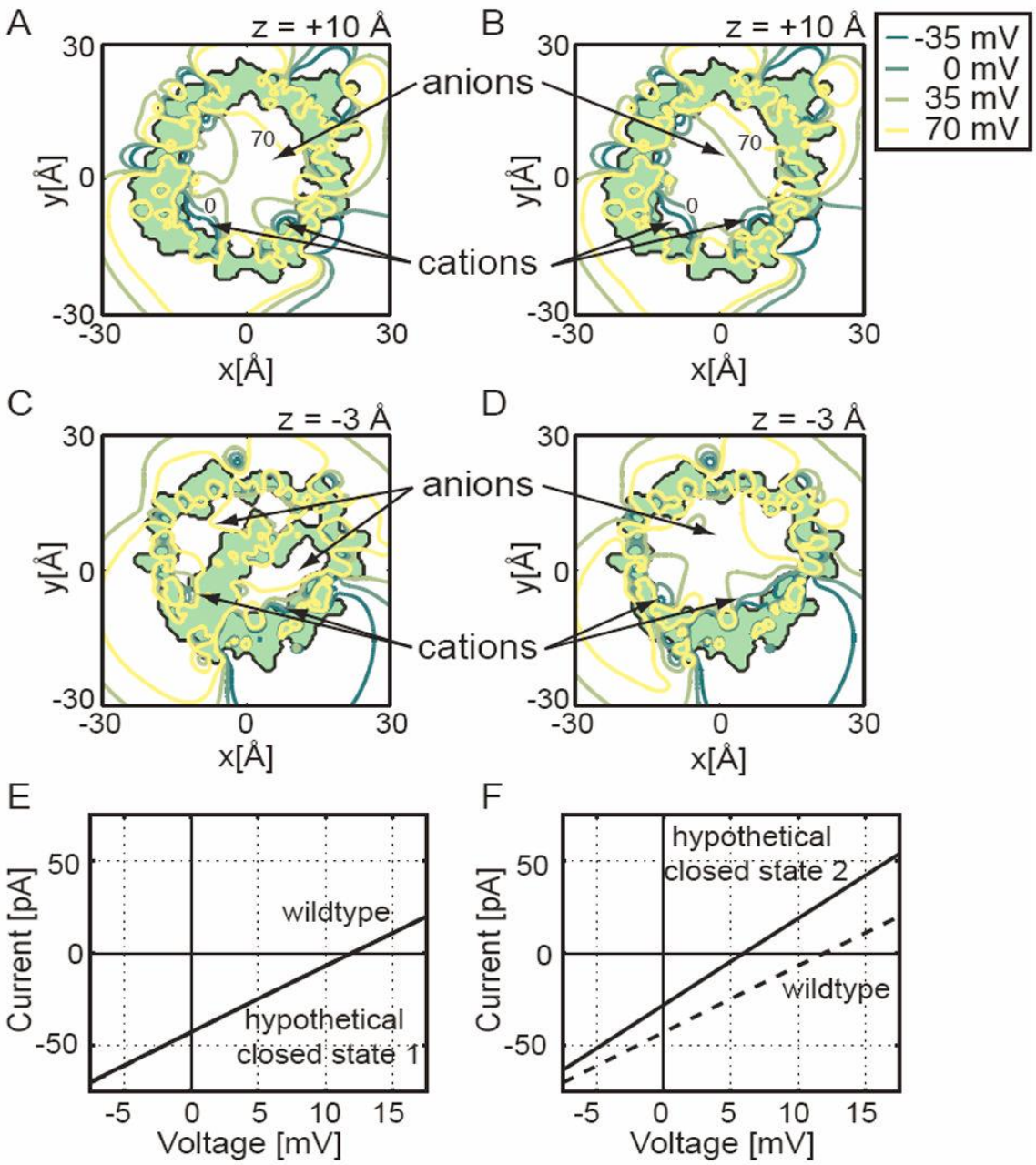


**Figure 4.7:** Biophysical properties of the two hypothetical closed states. The electrostatic potential of hypothetical closed state 1 was calculated and plotted at z = +10 Å (a) and z = -3 Å (c), and the isocontours for hypothetical closed state 2 were plotted at z = +10 Å (b) and z = -3 Å (d). Each channel is viewed along the pore's long axis, and the protein interior is shaded light green. We see in panel c that the N-terminal helix occludes the middle of the pore of hypothetical closed state 1, but panels b and d show that hypothetical closed state 2 has an unobstructed pore at all levels. As in Figure 4.4, four equally spaced isocontours are depicted with dark green curves representing negative potentials and yellow curves representing more positive potentials. From panel c we see that closed model 1 has only a very small portion of the pore favorable to cation passage. Current-voltage curves for closed state 1 (e) and closed state 2 (f) were also carried out using PNP calculations. The conductance of hypothetical closed state 1 (solid) is so similar to wild type (dashed) that it is hard to distinguish both curves. Due to the larger pore diameter, hypothetical closed state 2 has an increased conductance, indicated by a steeper slope (solid curve) compared to the wild type (dashed). Since the current-voltage curve in panel F crosses the x-axis at a positive potential, the channel is anion selective as is the wild-type channel.

## 4.3 DISCUSSION

### 4.3.1 Identification of open state of channel

Both the PB and PNP electrostatic calculations show that the mVDAC1 x-ray structure is anion selective suggesting that the structure is open. While the transfer free energy profile in Figure 4.1a has a clear minimum in the electrostatic component of the free energy, its depth is very weak, ~2.5 $k_BT$. However, this might be exactly what we would expect of a channel whose primary role is to quickly shuttle high-valence negatively charged metabolites across the membrane. An ATP molecule, with a charge of -4, will experience a well depth 4 times deeper than a chloride anion implying that a shallow minimum for chloride would be much deeper for ATP. Close coordination by magnesium or other cations could reduce this well, but if too deep, it could lead to increased ATP dwell times and decrease the channel conductance. The true test of the channel's conduction state will come from a detailed study of ATP and ADP permeation energetics. Unfortunately, due to the increased complexity and conformational flexibility, continuum approaches are not appropriate for studying ATP's interactions with the channel. Fully atomistic simulations will be required to properly address this question.

### 4.3.2 Current-Voltage measurements

The theoretical conductance values presented here are larger than those predicted by experiment for the open channel. PNP is a mean field theory that neglects dynamical ion-ion correlations, and it is generally thought that this can lead to a larger current flux through the pore (Im and Roux, 2002; Graf et al., 2004). Despite being inflated with respect to experiment, our calculations are in

good agreement with other researchers' findings that PNP theory overestimates the experimental values. For instance Im and Roux calculated a conductance value for OmpF that was 1.8 times higher than experiments carried out in 0.2 M KCl, while our value is 1.8-2.3 times higher than values reported for VDAC in 0.1 M KCl (Colombini, 1989). Nevertheless, such a large conductance value is even more incompatible with the partially closed-state conductance found to be 0.22 nS in 0.1 M KCl46. If the mVDAC1 structure truly represents the partially closed state, this would imply that our PNP calculations are off by a factor of 5, and to our knowledge, such a large discrepancy between theory and experiment has never been reported. Thus, we feel that our conductance calculations suggest that mVDAC1 represents the open structure. Interestingly, while PNP overestimates the flux, it appears to do a better job of determining the relative ratio of the anion to cation flux. In our case, we predict reversal potentials within 2 to 4 mV of the value reported for scVDAC1, and Im and Roux determined a value within 2 mV of the recorded value for OmpF.

### 4.3.3 Channel residues contributing toward selectivity

Our analysis illustrates that not all pore-facing residues contribute equally to channel selectivity. This was first apparent from our observation that most residues that affect selectivity in the Blachley-Dyson et al. 1990 study are on the lower half of the channel. From Figure 4.3c one can see that A134 and N207 are both pore-facing residues, but they are at the outer mouth of the channel near the upper solution. Acidic substitution of these residues has a modest effect on the reversal potential when the channel is in the configuration in Figure 4.5a, but it has almost no effect on selectivity when the channel is in the opposite orientation. Meanwhile, K20E and K61E impact selectivity regardless of the orientation of the channel. We believe that these results can

be explained by the proximity of the mutated residue to the channel's natural energy minima at z= -7.5 Å (Figure 4.1a). Residues that increase or decrease the depth of this minimum appear to have the largest effect on selectivity. Interestingly, the calculated reversal potential shifts elicited by point mutations found to affect selectivity, while significant, are still smaller than the experimental shifts (see Table 4.1). We feel that there are two primary reasons for this inconsistency. First, the charged, pore-facing residues on scVDAC1 and mVDAC1 are not strictly conserved, which could lead to a different electrostatic profile in the pore of mVDAC1. Second, we do not know the true, predominant rotamer conformations of the point mutants, and incorrectly modeled side chains could heavily influence the electrostatics along the permeation pathway. Additionally, nonmutated residues may adopt new rotamer conformations in response to a point mutant, and this could not be accounted for. All of these effects could explain the differences between theory and experiment. Nonetheless, there is a clear delineation between the selective mutants and the non-selective ones, especially when considering the channel orientation in Figure 4.5b.

### 4.3.4 Channel orientation in the membrane

Our results show that VDAC1 selectivity depends on the orientation of the channel in the membrane. The channel is slightly less selective when the N and C-termini face the high concentration bath (equivalent to ~ 2 mV shift in reversal potential compared to both termini facing the low-concentration bath). Since the orientation of VDAC1 in the mitochondria is currently debated (de Pinto et al., 1991; Stanley, et al., 1995; McDonald et al., 2009; Ujwal et al., 2009), the physiological relevance of this result is unclear. However, it is obvious that our calculated reversal potential shifts correspond most closely to the experimental results when the N and C-termini face the low-concentration bath (see Table 4.1). We believe that this finding could have consequences

for our understanding of VDAC's topology in the MOM. Theory could be used to predict mutant channels that produce large shifts in the reversal potential when the N- and C-termini are presented to the cytoplasm and very little shift when presented to the inner membrane space. Conversely, a set of mutant channels could be engineered that have the opposite property. Expressing and carefully recording these mutants directly from the mitochondrial outer membrane may provide a means to test the channel's orientation in vivo. Experimentally, we would expect large reversal potential shifts for one orientation and negligible shifts for the opposite arrangement. The control experiments would come from the point mutations that predict the opposite result.

### 4.3.5 Suggested gating motions

We investigated two hypothetical gating motions in an attempt to better understand the molecular determinants of VDAC1's voltage dependence. In both cases, the motions resulted in a sensor valence below experimentally reported values. With regard to motion 1, it is attractive to imagine that the N-terminal helix moves into the middle of the channel to block metabolite passage; however, this motion has no voltage dependence. Nonetheless, it is possible that a similar final state does result in channel closure. The N-terminal helix is amphipathic due to a distribution of both basic and acidic residues along its length, and therefore, simply rotating the helix in the membrane electric field could produce a sizable gating charge. Thus, the true motion could involve swinging the helix out into the pore and rotating it. Meanwhile, gating motion 2 also has some very attractive features despite producing only about half of the observed sensor valence. The reactivity of antibodies to the N-terminus increases with the lysis of the outer membrane indicating that the N-terminus is exposed or accessible from the inner surface of the MOM (de Pinto et al., 1991). Therefore, a model of gating has been suggested that involves the helix leaving the pore

prior to entering the partially closed state (Mannella, 1998). The helix may then associate with the lipid bilayer as suggested by immunoelectron microscopy (Guo et al, 1995). This second step would require the helix to move partially through the membrane electric field, and it may produce enough charge movement to account for the missing 1-2 fundamental charge units in gating motion 2. As further confirmation that neither of these motions is correct, we calculated the electrostatic properties of the end configurations in Figure 4.7. Both models are still anion selective, while the true partially closed state is cation selective. This suggests that neither of the proposed structural models is correct.

### 4.3.6 Voltage-Dependent behavior of the channel

Lastly, VDAC1's voltage dependence is more complicated than our analysis has suggested because the channel closes at both negative and positive membrane potentials. Energetically, it seems unlikely that both partially closed states are the same since the membrane potential would bias the channel in different states at different voltages. It is entirely possible that the closed state(s) involve a more complex rearrangement than simply moving the N-terminal helix, as suggested by functional work (Popp et al., 1996; Song et al., 1998). Computationally, it is more difficult to determine these alternate conformations if they involve rearrangements of the β-barrel itself, but such a scenario cannot be ruled out. Moreover, if gating involves the N-terminal helix, it is doubtful that it moves as a rigid body. All of these factors complicate the determination of the partially closed states from the known mVDAC1 structure. Fortunately, the partially closed and open states exhibit different selectivities and conductances, so future studies can judge the likelihood of any given hypothetical state based on sensor valence calculations as well as selectivity calculations using PNP theory as we have done in Figure 4.7.

## 4.4 MATERIALS AND METHODS

### 4.4.1 Poisson-Boltzmann calculations

We used the program APBS (Baker et al., 2001) to carry out continuum electrostatic calculations on the mVDAC1 structure (PDB ID 3EMN). Calculations were carried out using the Poisson-Boltzmann (PB) equation in the linearized limit in the presence of 100 mM salt concentration. The equation was solved using a finite difference method on a 161 × 161 × 161 grid with two levels of focusing. The grid spacing at the finest level of focusing was 0.56 Å. The PARSE parameter set was used to assign partial charges to the protein (Sitkoff et al., 1996) using the PDB2PQR web server with standard protonation states for all residues (Dolinsky et al., 2004). The influence of the membrane was included as a low-dielectric slab of dielectric value $\varepsilon m = 2$ (Grabe et al., 2004). Water was assigned a dielectric value of $\varepsilon w = 80$, and the protein dielectric constant was assigned values of $\varepsilon p = 2$, 5, and 10 in separate calculations. Based on the structure, a suitable path for the ion through the pore was selected (see green path in Figure 4.1c,d). We have adopted the convention that the N- and C-termini face the lower bath; this is represented by negative z values in Figure 4.1. The center of the channel is always positioned near z = 0 Å. Ion transfer free energies are calculated by first computing the total energy of the ion plus protein system and then subtracting the energy of the solo ion in bulk solution and the energy of the channel without the ion (Roux and MacKinnon, 1999; Grabe et al., 2006).

The voltage dependence of the hypothetical gating motions in Figure 4.6 was calculated using the same setup described above; however, the far-field boundary conditions were manipulated to impose an applied membrane potential in the program APBS as described previously (Baker et al., 2001). The interaction energy of the protein charges with the field due to

the membrane potential is calculated as follows. First, the electrostatic potential profile across the membrane-protein system is determined in the absence of any protein charges by calculating the PB equation with all of the protein charges set to zero. In this case, a uniform charge density is added to the lower bath to give rise to the desired membrane potential. Second, the protein charges are reintroduced and overlaid on the calculated electrostatic map. The interaction energy is given by the sum over all of the protein partial charge multiplied by the local membrane potential value calculated from APBS.

### 4.4.2 Poisson-Nernst-Planck calculations

We used PNP calculations to compute the steady-state ionic flux through mVDAC1 using code written in the Coalson lab (Kurnikova et al., 1999, Cardenas et al., 2000). Current-voltage curves were computed under bi-ionic conditions with the upper bath and lower bath maintained at 0.1 M and 1.0 M KCl, respectively, and curves were also computed under symmetric 1.0 M KCl solutions. The PNP equations were solved on a 135 × 135 × 185 grid with a grid spacing of 0.83 Å. The channel structures and spatial orientations were identical to those used in the PB calculations; however, the channels were flipped 180° to simulate the insertion with the opposite topology. As with the PB calculations, a low-dielectric slab representing the membrane extended from -14 to +14 Å along the z-axis, and it was assigned a dielectric value of 2. The protein dielectric value was set to 5. A membrane potential was imposed across the membrane, and the value was varied from -5 mV to +15 mV to construct the current-voltage relation. The bulk diffusion coefficient for potassium and chloride ions was set to $19.5\times10^{-6}$ $cm^2/s$, and the value in the channel was reduced by 40% based on our MD results. The zone of reduced diffusion was defined by a cylinder of radius 18.5 Å centered on the channel and extending 36 Å along the axis

of the channel from z = -19 to +17 Å. For each imposed membrane potential value, the PNP equations were solved via relaxation methods using anywhere from 36,000-47,000 iterations. Solutions under both symmetric and asymmetric conditions exhibited excellent convergence.

### 4.4.3 Molecular Dynamics Simulations

We used the CHARMM-GUI to align mVDAC1 along the z-axis, embed the protein in a DMPC lipid bilayer, and then solvate the entire system in a hexagonal cell (Jo et al., 2008). We enforced electroneutrality by adding 0.15 M KCl (14 positive ions and 17 negative ions). The approximate system size was 75 Å × 75 Å × 66 Å, and it consisted of 34,228 atoms. Simulations were carried out using NAMD with the CHARMM27 parameter set and TIP3P water molecules (Kale et al., 1999). Initially, a conjugate gradient minimization was carried out for 3,000 steps on the full system. During equilibration, the temperature was increased every 50 steps by 1 K until it reached 303 K using Langevin dynamics. The time step was 2 fs, and a 10 Å cut-off was used for van der Waals interactions. All electrostatic energies were calculated using the Particle Mesh Ewald summation. After reaching 303 K, an additional 1 ns of simulation was carried out using the NPT ensemble with a Langevin piston set to 1 bar. We equilibrated a chloride ion in the channel pore at two positions: z = 0Å and z = +2Å. From each set-up we ran a 2 ns simulation and recorded positions every 100 fs. For both simulations, the ion remained in the channel. For each ion trajectory we calculated $R^2(t) = (r(t) - r(t=0))^2$ for t = 0 to 1 ns, where r is the chloride ion's vector position in time. We then stepped through the time series data and recalculated $R^2(t)$ to arrive at an average squared displacement $\langle R^2(t) \rangle$. The slope of this curve was set equal to 6D to estimate the chloride diffusion coefficient in the channel, D (data not shown). We repeated this process for a potassium-chloride ion pair in a cubic water box of length 20 Å to estimate D in bulk solution.

Our calculations in the channel were ~ 40% smaller than our estimate of the bulk value, and this 40% reduction was used to model the diffusion coefficient of the ions in the channel for the PNP calculations. This amount of reduction is very close to the value used in previous studies of porin channels (Im and Roux, 2002).

## 4.5 ACKNOWLEDGEMENTS

We thank Carmen Mannella for critically reading the manuscript, and we are grateful to Seungho Choe for his help throughout this project. We also thank the Center for Molecular and Materials Simulations and Richard Christie for computational support. This work was supported by a grant to M.G. from the Myrtle Forsha Memorial Trust and the Lloyd Foundation through the PNC Charitable Trust Grant Review Committee. M.G. is an Alfred P. Sloan Research Fellow. The work of W.K. and R.C. was supported by NSF grant CHE-0750332.

# 5.0 CALCULATION OF IRON TRANSPORT THROUGH HUMAN H-CHAIN FERRITIN

The work** presented in this chapter was published in:

Rozita Laghaei, William Kowallis, Deborah G. Evans, and Rob D. Coalson. 2014. Journal of Physical Chemistry A. 118 (35), pp 7442–7453.

**Contributions from W. Kowallis consisted of setup of FACF calculations, PNP simulations, and discussion of overall channel behavior based on results of these calculations.

## 5.1 INTRODUCTION

Ferritins play a central role in iron storage in most forms of life, ranging from vertebrates through plants to microorganisms (Andrews, 2010). They control iron levels in organisms through the sequestration and release of iron from hydrated ferric oxide minerals stored in their inner cavity (Ebrahimi et al., 2012) and protect the cell against oxidative stresses (Bou-Abdallah,2005; Bou-Abdallah, 2010; Theil, 2011; Watt, 2011; Theil et al., 2013; Watt, 2013). Iron homeostasis and regulation is essential because iron is required in many cellular redox processes and electron transfer reactions. However, in high concentrations, iron can react to form toxic radicals and other chemical species (Zhao et al., 2006), and consequently its activity in cells needs to be strictly regulated.

Ferritins in vitro have also been used for several material science (Yamashita et al., 2010) and biomedical applications (Zhen et al., 2013). Ferritins have been successfully used to synthesize

nanoparticles using a variety of metals, e.g., Au, Ag, Pt, Co, Cr and Zn (Polanams et al., 2005; Kasyutich et al., 2010; May et al., 2010). Wild type and mutant ferritin nanocages allow for the synthesis of monodisperse nanoparticles less than 8nm in diameter and often incorporating novel mineral types (Kim et al., 2010; Kang et al., 2011; Keyes et al., 2011; Kasyutich et al., 2012; Zheng et al., 2012; Harada and Yoshimura, 2013). Given the ability for bioassembly onto surfaces, ferritin can be used to create ordered arrays of paramagnetic nanoparticles with applications in the computer industry (Kim et al., 2007; Yuau et al., 2007; Zhang et al., 2007). Ferritins have also been used as delivery vehicles for diagnostic and therapeutic agents (Zhen et al., 2013). Recent research on nanobatteries based on the ferritin structure has clearly demonstrated the potential for using ferritins for novel nanoscale applications (Zhang et al., 2006; Shin et al., 2010).

Mammalian ferritins have a nearly spherical shell-like structure, with 432 octahedral symmetry, and are composed of 24 subunits (Hempstead et al., 1997; Crichton et al., 2010). The subunits are comprised of 4-α helix bundles (with an additional fifth short helix at 60° to the bundle), usually of two different types, H (~21,000 Da) and L (~19,500 Da). Heteropolymers of H- and L-subunits are normally found in mammals, and the ratio of these is tissue-specific (Hempstead et al., 1997). The protein coat composed of these assembled subunits is approximately 20Å thick and surrounds an approximately 80Å wide central cavity, where iron is stored in mineral form.

The first steps to sequestration of iron as a mineral in the core consist of the uptake of $Fe^{2+}$ through the protein and then oxidation to $Fe^{3+}$ at the ferroxidase sites. The ferroxidase sites (found only in the H subunits) have been well characterized through a variety of spectroscopic and crystallographic studies (Zhao et al., 2005; Bertini et al., 2012). The binding sites at the ferroxidase site are comprised of highly conserved residues in animal ferritins, and are found in the center of

the α-helix bundles of the H-subunits (Theil et al., 2006; Theil, 2011). Recently, NMR techniques have been used to elucidate the pathway followed from these ferroxidase sites to incorporation of iron in the biomineral core (Turano et al., 2010). $Fe^{3+}O$ multimers move about 20Å along the inner core to nucleate at the fourfold channel openings on the inside of the protein coat before moving to the interior.

The entry of iron ions occurs through eight hydrophilic channels located along the three fold axes (Liu et al., 2007; Theil et al., 2008; Tosha et al., 2010). $Fe^{2+}$ enters the pores of these channels created at the vertices of 3 subunits. These channels are 15-20Å in length, and exit pores open into the internal cavity about 15Å from the ferroxidase site residues. The hydrophilic channels are highly conserved in animals and are lined with a number of carboxylated residues, notably Glu and Asp. Site specific mutagenesis and crystallographic data point to at least three possible binding sites along the three fold channel (Treffry et al., 1993; Theil et al., 2008; Tosha et al., 2010; Tosho et al., 2012). Crystallographic evidence shows the capture of $Zn^{2+}$ (an $Fe^{2+}$-like surrogate) in three specific sites along the three-fold channels (d'Estaintot et al., 2004; Toussaint et al., 2007). Mutations of the Asp and Glu in the channels of ferritins result in significant changes in the uptake of iron (Treffrey et al., 1993; Haldar et al., 2011), and blocking of the outside pore opening by a $[Cr(Tren)(H_2O)(OH)]^{2+}$ complex (Barnes et al., 2002) or peptides (Liu et al., 2007) also significantly alters the entry of iron. Opening of the pores by chaotropic agents (Liu et al., 2003) or site directed mutagenesis (Takagi et al., 1998; Jin et al., 2001) also leads to increased uptake and effusion of iron. The Asp131 and Glu134 residue structure in human H-chain is highly conserved in animals. The channel is funnel-shaped with a negative electrostatic potential on the outer opening and a negative gradient between the outside and the internal portion of the channel (Douglas et al., 1998; Tosha et al., 2010; Ceci et al., 2011). About halfway down the channel, a

triad of E134 residues (one from each subunit making up the three-fold pore) and a similar triad of D131 residues form the constriction in this funnel-shaped channel. Crystallographic data from a variety of ferritin structures show that these residues are about 5-6Å apart and form a constriction about 4-5Å wide in the crystal structure (Tosha et al., 2010). The hydrated octahedral complex $[Fe(H_2O)_6]^{2+}$ has a radius of about 5.6Å (Aguilar et al., 2007) and it is not known whether ligand exchange is required to move iron through the channel. Recent crystallographic studies have identified several hydrated $Mg^{2+}$ ions captured in the three-fold channels near these binding sites (Behera et al., 2012; Tosha et al., 2012).

While crystallographic data, mutagenesis and spectroscopic studies have elucidated the path of divalent ions into the ferritin structure through the three-fold channels, the rate of diffusion of iron in these channels is important for understanding the energetics and kinetics involved in uptake of iron (Bou-Abdallah et al., 2005). The rate constant for the kinetics of $Fe^{2+}$ from solution into the core of ferritin has been measured using horse spleen ferritin (Zhang et al., 2006). The rate of $Fe^{2+}$ penetration was measured spectroscopically by the formation of Prussian Blue in the ferritin core. The rate of reaction of $Fe^{2+}$ in solution to form Prussian Blue in the ferritin core evidenced a lag time in comparison to the formation of Prussian Blue in solution. This lag time is indicative of the rate of iron diffusion from solution to the ferritin core. The study concluded that the rate constant from solution to the inner core of ferritin is $0.4s^{-1}$, and estimated the diffusion constant to be about $5x10^{-20}$ $m^2/s$. A stopped flow fluorescence and absorption study was conducted on a series of fluorescent variants of human H ferritins (Bou-Abdallah et al., 2008). These studies were able to demonstrate that the three-fold and not the one-fold channels provide access for $Fe^{2+}$ to the ferritin core. In addition the rate constant was determined by stopped flow fluorescence quenching data. This rate constant of 216 $s^{-1}$ and a half-life of 3 ms is estimated to

correspond to the diffusion of iron through the three-fold channels to the ferroxidase site. An estimate of the apparent diffusion constant in the three-fold channels from this data is $5x10^{-16}$ $m^2/s$, which is considerably slower than that of the hydrated $Fe^{2+}$ ion in solution of $7x10^{-10}$ $m^2/s$.

Neither the crystallographic nor kinetic data can provide a more complete model of the dynamics of migration of iron as it moves through the three-fold channel. In particular, the effects on the rate of iron of diffusion through the channel due to random thermal motion, electrostatic gradients on the protein surface and fluctional changes in the three-fold channel due to protein motion in solution are not easily extracted. In this regard classical molecular dynamics simulations (MD) can be used to provide insight into the dynamics and energetics as an ion permeates an ion channel. Molecular level simulations have provided insight on the atomistic scale of ion transport through many transmembrane ion channels. A recent classical MD simulation of ferritin in the presence of iron has corroborated previous experimental observations and provided new insight into the dynamics of this process (Laghaei et al., 2013). These molecular dynamics simulations of human H-chain ferritin have confirmed that iron enters primarily through the three-fold channels and that iron binds strongly to the sites created by Asp131 and Glu134, and binds weakly to two other sites around His118 and Cys130, closer to the pore opening. The simulations also indicate a pathway for the iron after exiting the pore on the interior surface to the ferroxidase site through a sequence of residues, namely Thr135, His136 and Tyr137. In addition, these simulations provide dynamical information of how the iron moves through the channels and capture the response of the protein to the ion as it does so. Mechanistically, the simulations suggest that an $Fe^{2+}$ ion remains in the three channel binding sites until displaced by another entering $Fe^{2+}$ ion, whereupon the ion closest to the interior exits the channel and moves to the ferroxidase site.

Experiment suggests at least millisecond timescales for $t_{1/2}$ in the channel under physiological conditions (Bou-Abdallah et al., 2008). Given the long timescales involved, classical molecular dynamics cannot be used to determine the rate of permeation in this system. However, Poisson-Nernst-Planck (PNP) theory (Eisenberg, 1996), which has been shown to provide an efficient and generally effective method of determining transport of ions through standard membrane spanning ion channels (Coalson and Kurnikova, 2007), does not rely on explicit dynamical simulation, and is thus a more promising candidate for initial investigation of the kinetics of ion flow through threefold ferritin pores.

It is the goal of the present study to use the PNP method to obtain an estimate for ion transport rates through the three-fold channels in ferritin. PNP theory requires as input spatial diffusivity profiles of the permeant ions throughout the pore region. Here we use short-time all-atom simulations to calculate the appropriate diffusivity profiles, and then feed this information into a 3D PNP calculation of $Fe^{2+}$ flux through a three-fold pore. The inverse of the ion current thus extracted is used as an approximate measure of the transit time of a single $Fe^{2+}$ ion through the channel. This allows for direct comparison with previous kinetics experiments. Validation obtained by comparing such simulation models to experiment would be extremely useful. With the accuracy of the simulations confirmed, they could be used for future studies of ions other than $Fe^{2+}$ permeating through the ferritin structure and for calculating transport rates of other species (even oxo- and chloro- anions of metals) through the channel (Hilton et al., 2012). In the case of $Fe^{2+}$ ions, these simulations also provide insight into why the diffusion of the ions is so slow compared with the free hydrated ion in solution, and provide a picture of the uptake of iron into ferritin at atomic resolution. The theoretical approach used here provides insight into the different factors affecting transport rates: diffusion, electrostatics, and protein conformation in solution.

## 5.2 METHODS

### 5.2.1 Molecular Dynamics Simulation of Ferritin

Molecular dynamic simulations in the NPT ensemble were performed using the NAMD Molecular Dynamics (MD) simulation program (Phillips et al., 2005) with the CHARMM22 force field (MacKerrell et al., 1998) for the human H-ferritin protein (2FHA) which consists of 24 subunits. Simulations of the three-unit hydrophilic channel forming part of ferritin (Figure 5.1a-inset) comprising 50465 atoms in total were run for 20 ns. The TIP3W model was used for water solvent molecules. The MD simulation systems were electrostatically neutralized, with Asp and Glu residues taken to be deprotonated (-1 charge) and His deprotonated (neutral). To set the temperature at 300 K we used a Langevin thermostat. The thermostat damping coefficient was taken to be 5 $ps^{-1}$ and the time step was 1 fs per step. The external helices of each unit were fixed to prevent the dissociation of the three units during the simulations while the inner helices which form the channel were free to move. The interaction potential and size of $Fe^{2+}$ were obtained from Aguilar et al., 2007).

Extensive details of these MD simulations were presented in Laghaei et al., 2013, where they were used to elucidate mechanistic details of the influx of iron through 3-fold pores in ferritin. Here we use the same simulations to provide input data for a course-grained model of ion permeation kinetics, namely 3D PNP theory. In particular, we use the MD simulations to generate the protein structural details needed to set up the PNP simulation system. This includes a set of atomic coordinates for the atoms in the 3-fold region of the protein, from which the geometric structure of the flow region through the channel was constructed. Visual inspection of the channel and binding sites was done using the visualization programs VMD (Humphrey et al., 1996) and

PyMOL Molecular Graphics (Schrödinger LLC). The channel radius and center line were computed using the HOLE (Smart et al., 1996) program. Furthermore, in order compute the internal diffusivity of $Fe^{2+}$ ions as a function of their distance along the channel axis according to the Force Autocorrelation Function method described in the next subsection, the net force on an $Fe^{2+}$ ion fixed at a specified position along the channel axis was calculated every 5 fs.

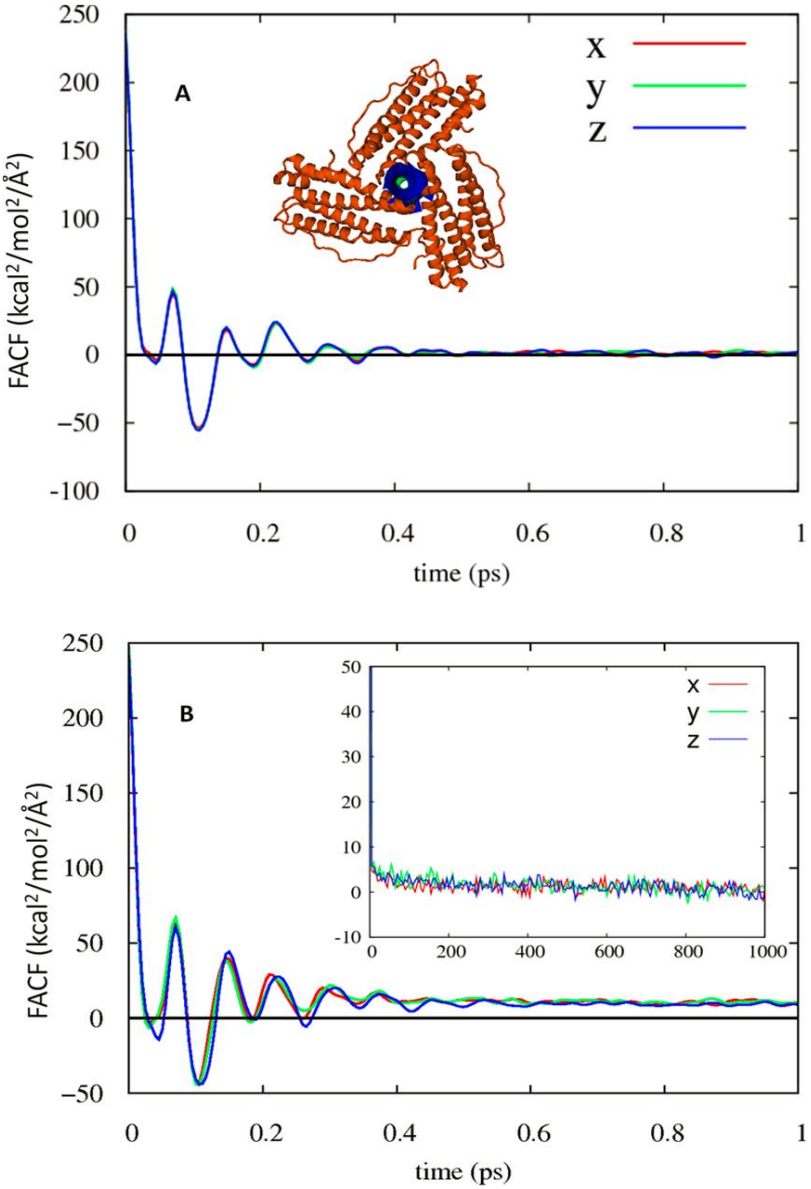


**Figure 5.1:** (a) FACF of $Fe^{2+}$ in bulk water solution. Inset: arrangement of helices to form a 3-fold pore through the ferritin shell. (b) FACF of $Fe^{2+}$ inside the ferritin channel (z = 13.5 Å). Inset: long-time tail of this FACF. For both locations of the $Fe^{2+}$ ion, x, y, and z components of the FACF are presented.

### 5.2.2 Force Autocorrelation Function (FACF) Method for calculating ion diffusivity coefficients

Calculation of the diffusion coefficient for an ion bulk water solution via all-atom MD simulation is straightforward. If r(t) is the distance the particle has moved at time t from its location at t=0, then direct calculation of the ensemble average $\langle r^2(t)\rangle$ for the ion gives a curve which is linear in time, and the slope of this curve can be read off to extract the diffusion constant $D$ acccording to the Einstein relation $\langle r^2(t)\rangle = 6Dt$. Calculating an effective diffusion constant for a drift-diffusion process occurring in the interior of a narrow ion channel is more challenging. The ion is now subject to systematic forces (e.g., electrostatic forces due to interaction with charges on pore-lining amino acids). In analyzing the intrinsic diffusion constant relevant to the ion motion in a specified region of the channel, one must carefully subtract the average systematic force on the ion. Temporal fluctuations in the force on the ion about this average value then serve as the random force function in a Langevin Equation level description of the process (Straub et al., 1987; Roux and Karplus, 1991).

One appealing way to account for these effects is provided by the (random) force autocorrelation function (FACF) method. In this procedure, the ion is placed somewhere in space and held fixed (*in silico*) while all other atoms in the system (protein and water in this case) are allowed to evolve in an MD simulation brought to Boltzmann equilibrium. The time averaged force $\langle\vec{F}\rangle$ on the ion is calculated. The temporal fluctuations about this average, i.e., $\vec{R}(t) = \vec{F}(t) - \langle\vec{F}\rangle$, are identified as the random force on the ion. From this time series the random force autocorrelation function (FACF) can easily be constructed. Then, using the 2nd Fluctuation

Dissipation theorem (Kubo, 1966; Koneshan et al., 1998) (and assuming Markovian friction), the friction constant associated with the ion is calculated as:

$$\gamma = \frac{\int_o^\infty \langle R_z(0) R_z(t) \rangle dt}{k_B T} \tag{5.1}$$

Where $R_z(t)$ is z-component of the random force vector. Finally, using the Stokes-Einstein relation, $D = {k_B T}/{\gamma}$ we assume here that diffusion is isotropic, so that $D_x = D_y = D_z = D$. We have checked that this isotropy holds to a good approximation for $Fe^{2+}$ inside ferritin, as described in the Results section.) We expect that the diffusion constant characterizing a particular ionic species will vary with the location of the ion inside the channel, reflecting the different molecular environment there. In particular, we expect D to decrease below its bulk solution value as the ion enters the channel, due to the geometric confinement supplied by the latter, as well as the imposition of large additional electrostatic forces on the ion by charged or partially charged chemical groups on the protein which are in close proximity to the aqueous pore. Indeed, our calculations on ions inside the ferritin channel show large effects of this type, leading to a significant reduction in ion diffusivity compared to bulk values (cf. Section **5.3.1** below).

### 5.2.3 Summary of Poisson-Nernst-Planck (PNP) Theory as Implemented via a 3D PNP Solver

Ions are assumed to execute Brownian Dynamics in the overdamped limit, i.e., according to the Smoluchowski Equation (Chandrasekhar, 1943). If the local concentration of the $k^{th}$ species of ions is $c_k(\vec{r})$ and its local diffusion constant is $D_k(\vec{r})$, then the local flux of this ion species is given by:

$$\vec{j}_k(\vec{r}) = \vec{D}_k(\vec{r})\left[-\vec{\nabla}c_k(\vec{r}) + \beta\vec{F}_k(\vec{r})c_k(\vec{r})\right] \quad (5.2)$$

Here, $\beta = [k_B T]^{-1}$ and $\vec{F}_k(\vec{r})$ is the local force acting on an ion of species k. PNP is an electro-diffusion model, i.e., the relevant force is taken to be the electrostatic force provided by all other charges in the system (Kurnikova et al., 1999). This force depends on the local electric field, or equivalently, on the electrostatic potential profile $\phi(\vec{r})$. Specifically: $\vec{F}_k(\vec{r}) = -q_k\vec{\nabla}\,\phi(\vec{r})$, where $q_k$ is the charge of an ion of species k. (Note: In addition to this electrostatic force, there is a strong repulsive force that prevents ions from moving through the "walls" of the channel or the membrane. These excluded volume interactions can be incorporated into boundary conditions for the Nernst-Planck Equations introduced below.) In general $c_k(\vec{r}), \phi(\vec{r})$ evolve in time. Here we will concern ourselves only with steady state ion flow, so that ion concentration and electric potential profiles are time-independent. For steady state concentrations to obtain, we must have $\vec{\nabla}\vec{j}_k(\vec{r}) = 0$. Thus, the following drift-diffusion equation, designated as the Nernst-Planck (NP) Equation, must be satisfied for each of the K ionic species in the system:

$$0 = \vec{\nabla}\cdot\left\{D_k(\vec{r})\left[\vec{\nabla}c_k(\vec{r}) - \beta\vec{F}_k(\vec{r})c_k(\vec{r})\right]\right\}\ ,\ k = 1,2,\ldots,K \quad (5.3)$$

The electric potential depends on the location of fixed charges in the system as well as the mobile ion charge distributions. Charges fixed on the protein arise due to deprotonation of acidic residues or protonation of basic residues; electronic polarization of neutral moieties within the protein can also lead to effective partial charges on certain atoms. Although the electrolyte solution must be overall charge neutral, the positive and negative ions in general adjust differently to the electric fields within the system, leading to local imbalance of mobile charge at a given point in space. Adopting a mean-field approximation based on the presumed steady state mobile ion distributions, we solve the Poisson Eq. to determine $\phi(\vec{r})$:

$$\vec{\nabla} \cdot \left(\varepsilon(\vec{r})\vec{\nabla}\phi(\vec{r})\right) = -4\pi \left[\rho_{fixed}(\vec{r}) + \sum_{k=1}^{K} q_k c_k(\vec{r})\right] \tag{5.4}$$

where $\varepsilon(\vec{r})$ is the static dielectric coefficient profile and $\rho_{fixed}(\vec{r})$ is the local density of fixed charge. We discretize the NP equations (one for each ion species), i.e., Equation 5.3, and also the Poisson Equation 5.4 onto 3D rectangular grids. Supplemented by appropriate boundary conditions, these equations can then be updated self-consistently to convergence. The relevant boundary conditions for the NP equations are, for each ion species, the prescribed ion concentrations in the reservoir on either side of the channel/membrane system (or ferritin shell, in case of interest here) and zero flux boundary conditions at the boundaries between the aqueous flow system and the protein pore and membrane (or ferritin shell). For the Poisson Equation 5.4, if there are no externally applied electric fields we set $\phi = 0$ on the boundaries of the electrostatic simulation box. While this is clearly the appropriate boundary condition for a standard membrane spanning ion channel, the situation could in principle be different for the 3-fold pores in ferritin because the internal cavity reservoir is not infinite in size and there are other charged species (especially, the other 3-fold channels in the ferritin shell) in close proximity to the pore selected for PNP analysis. To ascertain whether there is any significant intrinsic difference between the electric potential in the central cavity vs. that infinitely far from the protein in the cytoplasm, we inserted the entire 24-subunit ferritin molecule into the APBS Poisson-Boltzmann Equation solver (Baker et al., 2001). Following a similar analysis on ferritin-like molecules by Ceci et al., 2011, we set the salt concentration to 0 for this calculation, i.e., solved the Poisson Equation. We found an intrinsic potential difference of only ~0.1 $k_BT/e$, which justifies the $\phi = 0$ boundary condition noted above. Figure 5.2 shows the electrostatic potential of the entire ferritin molecule. The

following features merit emphasis: i) Charges distributed throughout the ferritin molecule generate a weak negative potential at its cytoplasmic edge. ii) Only the 3-fold channels are strongly (negatively) charged. Moreover, the 3-fold channels are far enough apart that each 3-fold channel can be considered in isolation from the rest of the ferritin molecule as far as electrostatic forces are concerned. This provides justification for the PNP model developed, which includes only one 3-fold channel (neglecting any electric fields generated by other charged atoms in the protein).

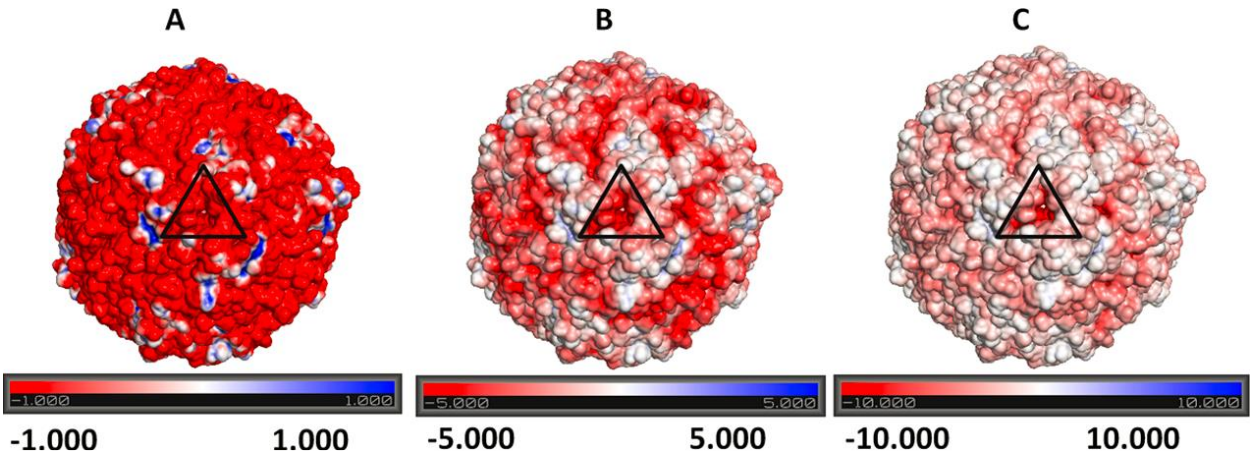


**Figure 5.2:** Electrostatic potential map for human H-chain ferritin, calculated by solving the Poisson equation (no mobile electrolyte ions) in APBS (Baker et al., 2001). Negative potential is shown as red; positive potential, as blue. (The potential goes to zero far outside the ferritin molecule.) The black triangle highlights the location of one three-unit channel. Note the different potential scales in panels a, b, and c (units of potential are $k_BT/e$).

Once converged ionic concentration profiles and electric potential profile have been obtained after numerical solution of the PNP equations, we appeal to Equation 5.2 for the steady state ion fluxes to extract the ion current of each species moving through the aqueous channel.

## 5.3 RESULTS

### 5.3.1 FACF calculation in the $Fe^{2+}$ ion diffusivity profile

Of primary interest here is the spatial diffusivity profile of $Fe^{2+}$. In Figure 5.1a we show the $\langle R_\alpha(t)R_\alpha(0)\rangle$, $\alpha = x.y.z$ for an $Fe^{2+}$ ion in bulk water and in Figure 5.1b for an ion at the position z=13 Å inside the channel. (See Figure 5.3 for the orientation of the ferritin pore w.r.t. the z axis.) Importantly, we find that the correlation functions for x,y,z components of the $Fe^{2+}$ ion diffusivity coefficient at a given value of channel axis coordinate z are very similar, thus giving credence to our assumption in the PNP analysis outlined above that ion diffusivity, while spatially dependent, is isotropic everywhere. For an ion bulk water the FACF exhibits damped oscillation, and quickly decays to zero (in less than 1 picosecond; cf. Figure 5.1a). In the case where the $Fe^{2+}$ ion is located well inside the channel, after an initial period of oscillation and partial decay, the correlation function reaches a regime where it decays monotonically but very slowly to 0. The full decay of this correlation function tail can take as long as 1000ps (cf. Figure 5.1b). This slow temporal decay, gives rise to a large time integral of the FACF and hence a large local friction constant (or, equivalently, a small local diffusivity constant).

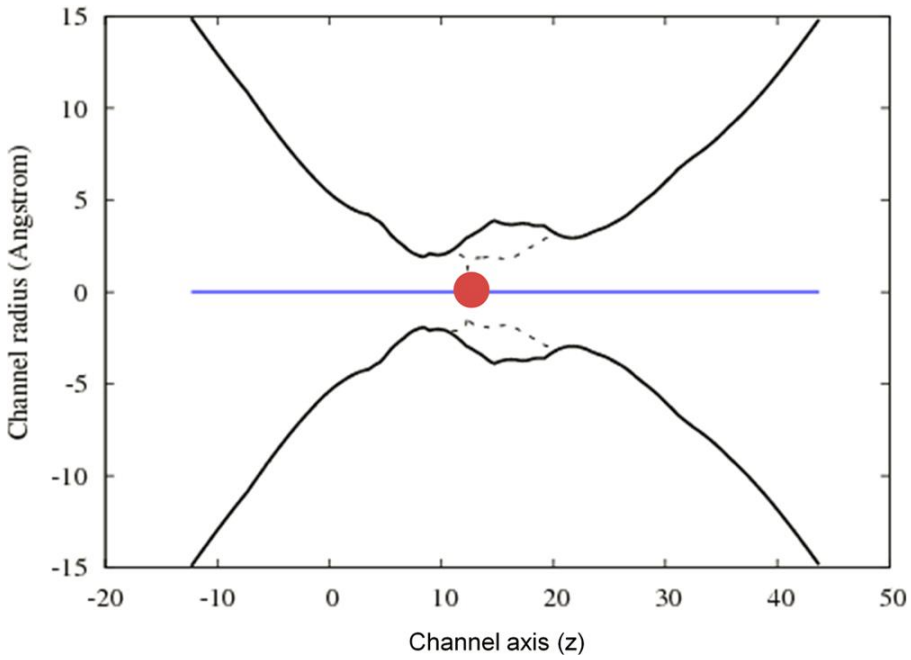


**Figure 5.3:** Black solid line: channel radius obtained from the HOLE program (Smart et al., 1996) when an ion is not inside the channel. Black dotted line: channel radius when a Na+ ion (red circle) is inside the channel.

Using the procedure described above, we obtained a value of $7x10^{-6}$ $cm^2/sec$ for the bulk diffusion constant of $Fe^{2+}$ in water at room temperature and 1 atm pressure. This compares well with the experimentally measured value of $7x10^{-6}$ $cm^2/sec$ (Bou-Abdallah et al., 2005). Figure 5.4 shows the spatial diffusivity profile of an $Fe^{2+}$ ion along the channel axis, extracted using the FACF method. Note the large reduction of D for an ion residing inside the pore relative to its bulk solution value. The reduction factor depends on the location of the ion within the channel, with a maximum reduction factor of ca. 900 times and an average reduction factor (based on rough channel length indicated in the figure) of ca. 400 times smaller.

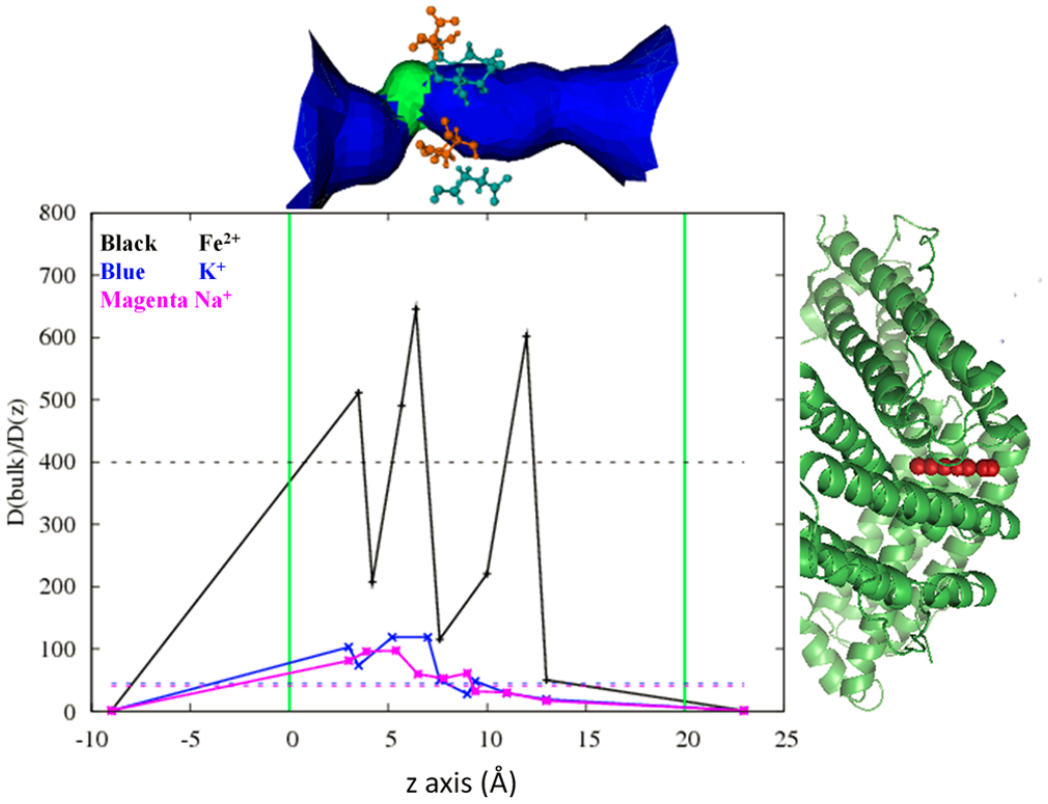


**Figure 5.4:** Top: ion channel surface obtained from the Hole program. The blue color denotes a region where the pore radius is >2.30 Å, and the green color denotes a region where 1.15 Å < pore radius < 2.30 Å. Glu (cyan) and Asp (orange) residues are indicated. Right: 3-fold channel and the positions of $Fe^{2+}$ (or other positive ions, shown with red balls) inside the channel used in FACF calculations. Left: diffusivity coefficient along the channel obtained using the FACF method. (The bulk diffusion constant calculated via the FACF method is $7 \times 10^{-6}$ $cm^2/s$.) Key: black, $Fe^{2+}$; magenta, $Na^+$; blue, $K^+$; vertical green lines at z = 20 Å, cytoplasmic entrance; vertical green lines at z = 0 Å, exit to inner cavity. The average over all data points of the internal $Fe^{2+}$ diffusion coefficient (i.e., the data points at values of z between the two vertical green lines) is ca. 400 times smaller (dashed black horizontal line) than the bulk diffusion constant. The corresponding average for the internal $Na^+$ and $K^+$ diffusion coefficients is ca. 40 times smaller (dashed magenta horizontal line for $Na^+$; dashed blue horizontal line for $K^+$) than the corresponding bulk diffusion constant.

To explore and calibrate the large reduction in the internal diffusion constant for $Fe^{2+}$, we performed similar calibration for two monovalent ions $Na^+$ and $K^+$. Previous calculations of the internal diffusion constant for narrow ion channels (Mamonov et al., 2006; Cheng et al., 2010) have found a reduction of less than x10-20 for monovalent ions inside a narrow channel (sufficiently narrow to require single file ion motion through the pore). Here we first computed the diffusion constant for $Na^+$ and $K^+$ in bulk water using the FACF method described above. We obtained values of 11 $\times 10^{-6}$ $cm^2/s$ and 15.5 $\times 10^{-6}$ $cm^2/s$ for $Na^+$ and $K^+$, respectively, which are in

good agreement with experiment ($13.3\times10^{-6}$ $cm^2/s$ and $19.6\times10^{-6}$ $cm^2/s$ for $Na^+$ and $K^+$, respectively (Passiniemi, 1983; CRC Handbook, 1994). Then we computed the internal D(z) diffusivity profile for a $Na^+$ along the channel axis. The results are shown in Figure 5.4. The reduction in diffusion constant relative to the bulk value is not as large as for $Fe^{2+}$, but it is still striking: there is a maximum reduction factor of 65 and an average reduction of ca. 40. Our goal in studying the diffusivity profile of monovalent ions in this work is to calibrate against the corresponding $Fe^{2+}$ results, and against previous results for monovalent ions inside ion channels. The fact that we obtain essentially the same results for $Na^+$ and $K^+$ provides a consistency check on our calculations in ferritin.

What is the source of the large internal friction constant reduction factors calculated for both $Fe^{2+}$ and $Na^+$? The six negatively charged side chains along the narrow channel form two rings almost 5Å apart which provide electrostatic binding sites that stabilize cations in the pore. Such binding sites have in fact been observed in several previous crystallographic studies (Treffry and Harrison, 1984; Wardeska, 1986). Furthermore, the channel forms a kink at its point of narrowest construction (cf. Figure 5.5) that further hinders the escape of the permeant ions.

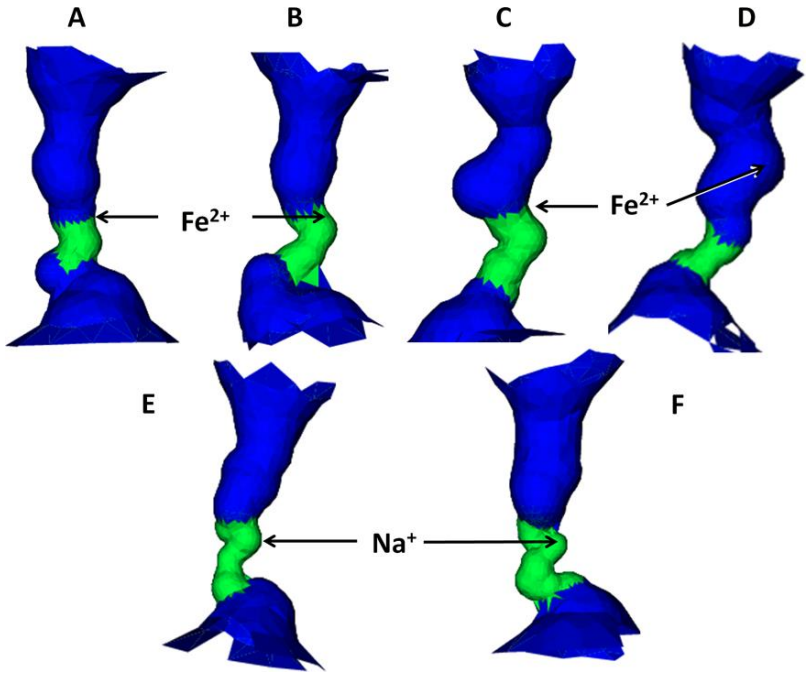


**Figure 5.5**: HOLE program rendering of 3-fold pore channel snapshots taken from several different MD simulation runs with an $Fe^{2+}$ ion (a)−(d) or an $Na^{+}$ ion (e), (f) fixed at various positions inside the channel as indicated. Key: blue, pore radius > 2.30 Å; green, 1.15 Å < pore radius < 2.30 Å. Note that some amount of kinking is always present.

### 5.3.2 Construction of the PNP simulation system

X-ray structures of the ferritin protein indicate that there are multiple pores connecting the external (cytoplasmic) region and the inner core (inside the ferritin protein shell). Most are formed at the boundaries of subunits of the proteins, and can be classified by the symmetry of these boundaries, namely: 2-fold, 3-fold and 4-fold symmetric sites. There are also direct conduits through a single subunit, designated as 1-fold pores. Experiments have shown that the 3-fold pores provide the primary conduction pathway for $Fe^{2+}$ ions entering the ferritin interior from the cytoplasm (Pacques et al., 1979; Wardeska et al., 1986; Treffry et al., 1993; Yang et al., 1996). Indeed, our own prior MD simulations support this finding (Laghaei et al., 2013). Hence we will focus here on calculating the rate of $Fe^{2+}$ influx through a typical 3-fold channel, using 3D PNP theory as implemented via the finite-difference solver described above.

A snapshot of the 3-fold pore taken from our MD simulations is shown in Figure 5.6. 3D PNP theory was developed for computing ion currents through an ion channel protein embedded in a lipid bilayer membrane. Ferritin is not a standard ion channel in this regard. There is no lipid bilayer. Instead the remainder of the protein shell serves as an effective membrane in that it prevents $Fe^{2+}$ ions from flowing freely into the ferritin interior – the ions must traverse the narrow 3-fold pores in the shell. To utilize our 3D PNP solver to compute $Fe^{2+}$ flux into ferritin, we constructed a simulation system as depicted in Figure 5.7. The pore region is based directly on a snapshot from our MD simulation, which is rendered onto a spatial simulation grid just as we would with a standard transmembrane ion channel (Kurnikova et al., 1999; Cardenas et al., 2000; Hollerbach et al., 2000; Mamonov et al., 2003; Noskov et al., 2004). We then impose an artificial membrane, i.e., a low dielectric slab outside of the pore structure which is impermeable to ions. (In previous studies of standard ion channel systems (Kurnikova et al., 1999; Cardenas et al., 2000; Mamonov et al., 2003; Choudhary et al., 2010) we have found that precise details of the bilayer membrane outside the channel pore do not critically affect ion flow through the channel beyond the properties just noted, namely blockage of ion flow through the channel and low dielectric constant.) We assigned a width of 20 Angstroms to the dielectric slab representing the artificial bilayer, consistent with the width of the ferritin protein shell. For initial conditions, we set a non-zero value of bulk $Fe^{2+}$ concentration in the cytoplasmic reservoir. (This is balanced, electrostatically, by including twice this concentration of $Cl^-$ ions in the cytoplasmic reservoir. However, no anions permeate into the channel due to the very large electrostatic energy barrier generated by the 3 Glu and 3 Asp residues that line it.) An $Fe^{2+}$ ion which reaches the internal edge of the ferritin shell after traversing the 3-fold pore quickly diverts to one of the ferroxidase centers, where it combines with hydrogen peroxide or $O_2$ to eventually form inert $Fe_2O_3$. The latter

is incorporated as a mineral at the center of the ferritin interior core. Here we represent this sequence of events by placing an absorbing boundary condition at the internal entrance to the 3-fold ferritin pore. Within the drift-diffusion model that underlies PNP theory, this is accomplished by setting the concentration of [$Fe^{2+}$] (and [$Cl^{-}$]) to 0 in the interior reservoir.

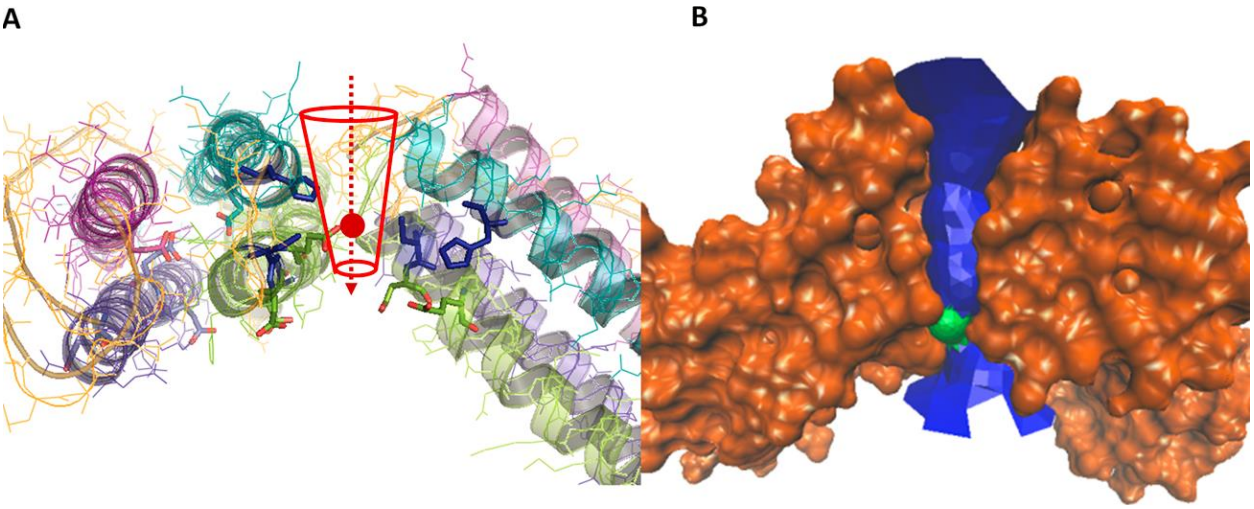


**Figure 5.6:** (a) and (b) 3-fold channel via two different representations. Panel a shows the pathway of ions (red arrow). Panel b shows the shape of the pore (ion flow space). In panel b, blue indicates pore radius >2.30 Å and green denotes 1.15 Å < pore radius < 2.30 Å.

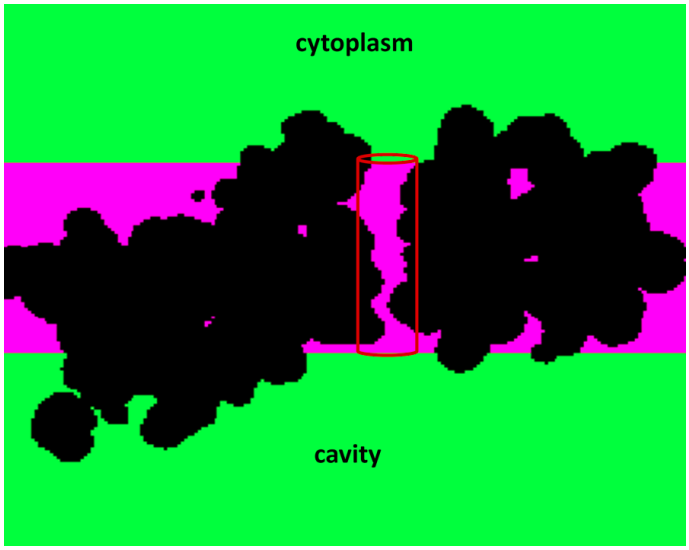


**Figure 5.7:** Initial ferritin conformation selected for PNP calculations. Black: 3-unit channel. Green: cytoplasmic and inner cavity bathing solutions. The magenta region is analogous to the bilayer membrane in a standard ion channel. The red cylinder is generated by the PNP solver algorithm to place the membrane slab relative to the protein pore. The ion flow region extends from the cytoplasmic bath through the magenta region contained within the red cylinder inside the pore. (Ions reaching the cap of the red cylinder that abuts the cavity reservoir are subjected to an absorbing boundary condition for the calculation of $Fe^{2+}$ influx currents.)

For completeness, we have also calculated $Fe^{2+}$ flux for the reverse process, i.e., $Fe^{2+}$ ions inside the ferritin interior core and none (or a negligibly small number) outside. This situation presumably occurs when $Fe^{+3}$ in the mineral core is converted back to $Fe^{2+}$ in order to re-inject it into the cytoplasm. Interestingly, we find similar $Fe^{2+}$ ion currents under similar driving conditions for the $Fe^{2+}$ influx and efflux processes, as described in detail below.

Given the PNP simulation system outlined above, the lattice-discretized PNP partial differential equations are iterated to self-consistency. As output we obtain 3-D grid representations of the electric potential and the concentration profiles of both ionic species ($Fe^{2+}$ and $Cl^{-}$) everywhere in space. A 2D slice of the 3D electric potential and the associated cation and anion concentrations obtained from a typical PNP calculation are shown in Figure 5.8. One sees immediately that $Cl^{-}$ ions do not permeate into the interior of the ferritin shell, for reasons discussed above. We also present 1-D plots of the electric potential and $Fe^{2+}$ density profiles along the channel axes in Figures 5.9 and 5.10, respectively.

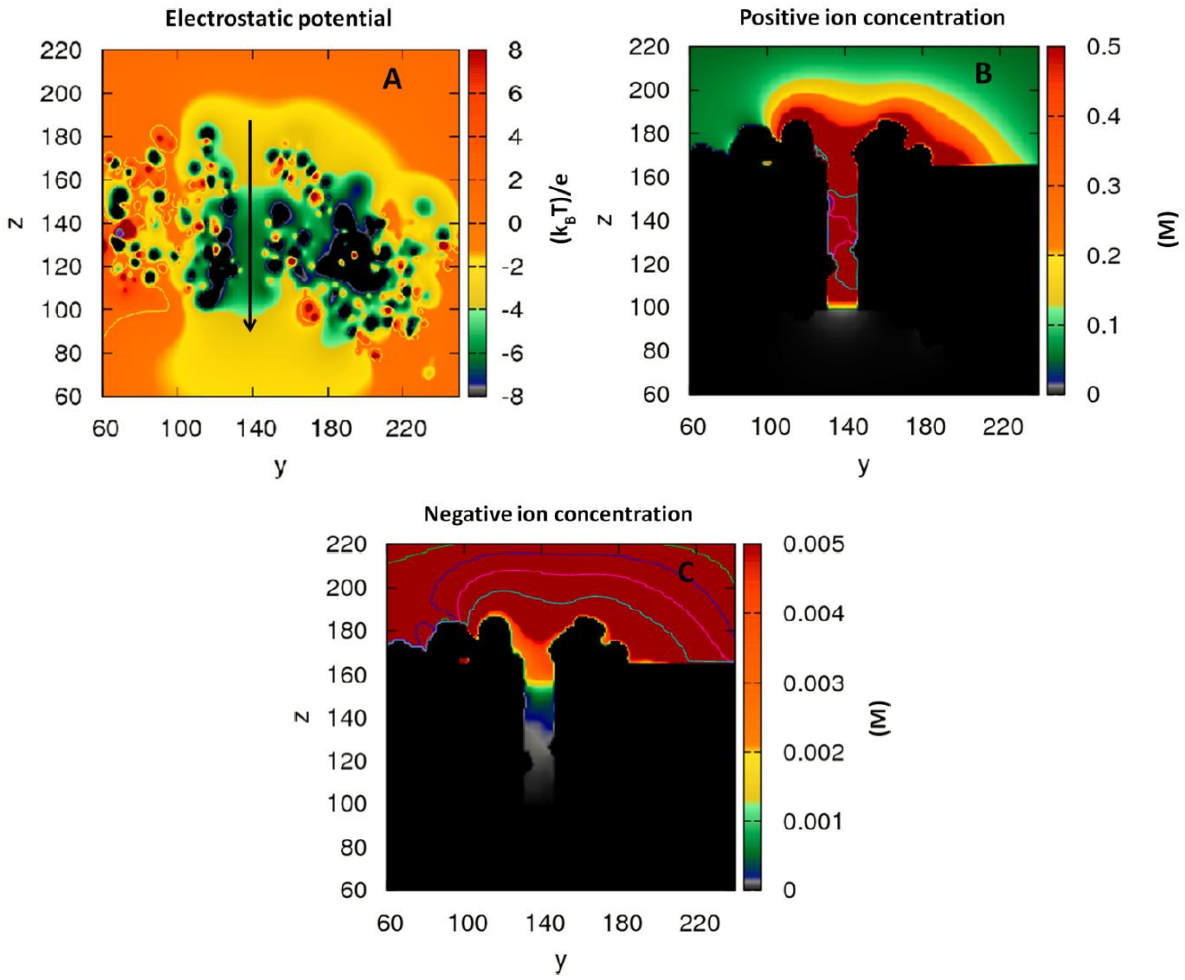


**Figure 5.8.** Two-dimensional slice of the (three-dimensional) electrostatic potential (panel a) and mobile ion concentration of cations (panel b) and anions (panel c) for the 3-fold channel calculated via PNP. y and z axes show the grid points used in the PNP calculation (grid point spacing = 1/3 Å); the channel spans from grid points 100 to 160.

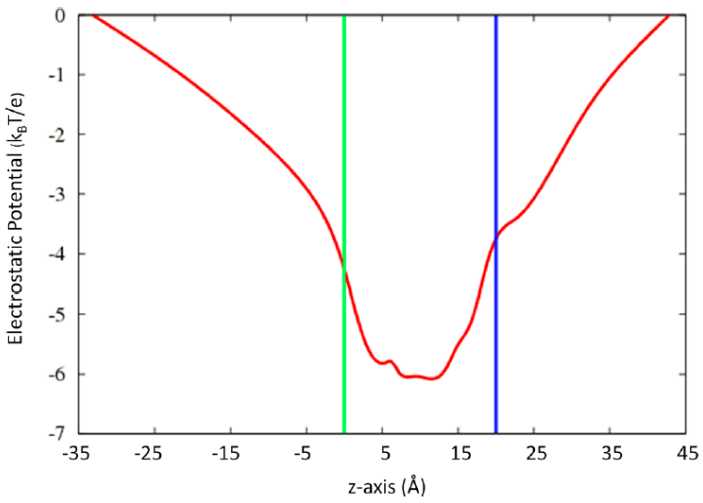


**Figure 5.9:** Electrostatic potential along the channel axis: blue vertical line, cytoplasmic entrance of the channel; green vertical line, exit to the inner cavity region.

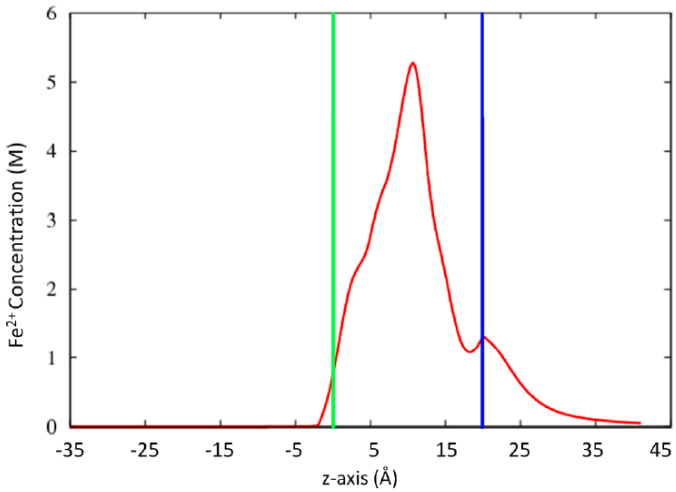


**Figure 5.10:** Red: $Fe^{2+}$ concentration along z-axis (channel axis). Blue vertical line: cytoplasmic entrance of the channel. Green vertical line: exit to the aqueous cavity inside the ferritin protein coat. The bulk cytoplasmic concentration of $Fe^{2+}$ is 0.05 M.

As noted above, the PNP equations directly specify the current density of each ion species everywhere in space in terms of the electric potential and ionic concentration profiles at steady state (Equation 5.2). These current densities can be integrated over an appropriate surface (e.g., a transverse patch of surface area within the channel pore) to obtain the net flux of ions through the pore, and hence the net electric current.

The physiological concentration of $[Fe^{2+}]$ in the cytoplasm is very low, ca. $2\times10^{-5}$ M. This renders infeasible direct simulation of the kinetics of $Fe^{2+}$ influx by all-atom Non-equilibrium Molecular Dynamics (NEMD) (Aksimentiev and Schulten, 2005; Kutzner eta l., 2011) or even by coarse-grained Brownian Dynamics (Allen et al., 1999; Graf et al., 2000; Noskov et al., 2004), as the number of ion permeation events would be far too low to extract an ion current with statistical reliability. PNP is more flexible in this regard, because it does not track real time molecular trajectories. Rather it solves coupled nonlinear partial differential equations, with their solution (electric potential and mobile ion concentration distributions) representing the desired steady state, including predictions for ion currents through the system as described above. However, the PNP

equations become difficult to converge numerically at very low ionic concentration. In practice, with our PNP solver we are limited to ~0.005M $FeCl_2$ concentration in the cytoplasmic bath. We thus must invoke some type of extrapolation scheme to extend from the low concentrations that we can access with our PNP solver to the very low physiological concentration of $[Fe^{2+}]$ in the cytoplasm. In the present study, we fit data points on a current-concentration (I-C) curve to a Michaelis-Menten (MM) functional form, i.e.:

$$I = \frac{I_{max}[Fe^{2+}]}{C_{max}+[Fe^{2+}]} \tag{5.5}$$

We have found in previous work on other ion channels that this functional form provides an accurate description of the saturation behavior of I-C curves with increasing ionic strength of the non-zero bathing solution that drives ionic flux through the channel (Cheng et al., 2007; Coalson and Cheng, 2010). In the present study, we adjust the parameters $I_{max}$ and $C_{max}$ to optimize the fit to our computed I-C data points, and then extrapolate Equation 5.5 down to the physiologically relevant concentration of ca. $10^{-5}$M $Fe^{2+}$.

Figure 5.11 shows a typical set of data points under conditions of 0 M $[Fe^{2+}]$ inside the ferritin channel when the electric potential difference inside vs. outside the ferritin cavity is set to zero. The optimized MM fit to these data points is also indicated. Using the MM fit, we estimate an inward $Fe^{2+}$ ionic flux at $2\times10^{-5}$ M $[Fe^{2+}]$ in the cytoplasmic reservoir of 184.4 $Fe^{2+}$ ions/sec. By inverting this flux, we can estimate the transit time of a single $Fe^{2+}$ ion inwards through the 3-fold pore of ferritin as ca. 5.4ms. This number is in good agreement with the experimental estimation of the same transit time given by Bou-Abdallah et al., 2008.

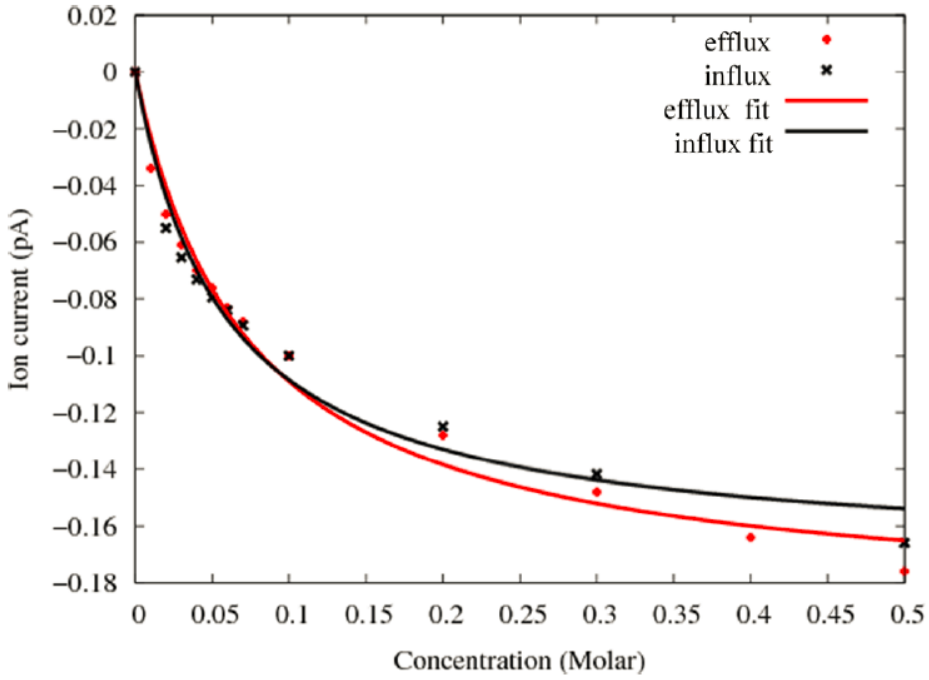


**Figure 5.11:** Current−concentration (I−C) curves are shown for influx ([$Fe^{2+}$] = 0 in the ferritin cavity) and efflux ([$Fe^{2+}$] = 0 in the cytoplasm) permeation processes. In both cases the electric potential difference between the two aqueous reservoirs is set to 0.

Efflux of iron from the ferritin core is instigated by dissolution of the mineral core, whereby $Fe^{3+}$ is converted to $Fe^{2+}$ in significant quantities. The release of $Fe^{2+}$ can be detected experimentally under physiological conditions (Theil, 2013). (While the exact trigger for this process is not well understood *in vivo*, spectroscopic studies *in vitro* have shown that a number of chemical agents including urea and biologically relevant riboflavin derivatives trigger efflux of $Fe^{2+}$ from the core. The initial reductive step results in an internal [$Fe^{2+}$] much higher than [$Fe^{2+}$] in the cytoplasm (Funk et al., 1985). This $Fe^{2+}$ can then exit the 3-fold pores via a Fick's Law driving force. To probe the details of the $Fe^{2+}$ efflux process, we repeated the computation described above with a non-zero fixed [$Fe^{2+}$] value inside the ferritin shell and [$Fe^{2+}$]=0 in the cytoplasm. The resultant I-C curve is also shown in Figure 5.11. Interestingly, it closely resembles

the I-C curve computed for the influx process, which would imply a similar time scale for $Fe^{2+}$ efflux as for influx of ions at similar driving concentrations of $Fe^{2+}$.

## 5.4 DISCUSSION AND CONCLUSIONS

In a standard membrane-spanning ion channel protein, the transit time of an individual ion is typically on the order of 10-100 nanoseconds. For ferritin, experimental estimation of the time for an $Fe^{2+}$ to pass from the cytoplasmic entrance to the exit of the protein coat into the internal aqueous region is on the millisecond time scale. What factors could account for the much slower ion transit through ferritin? One possibility is that the electrostatic binding sites inside the 3-fold ferritin pore are so strong that ions entering the pore become stuck for a long time in deep attractive potential wells. Our recent MD simulations of $Fe^{2+}$ flow through 3-fold pores in ferritin did not show such an effect (Laghaei et al., 2013). No evidence for infrequent barrier crossing events was seen. In contrast, using a very large (~20M) cytoplasmic $Fe^{2+}$ concentration in our MD simulations, we found that $Fe^{2+}$ traversed the channel rather quickly – in a few nanoseconds. Of course the physiological concentration of cytoplasmic $Fe^{2+}$ is very low, ca. $10^{-5}$ M, which goes a long way towards explaining the slow transit through the channel. By contrast, typical physiological concentrations of ions like [$Na^+$] and [$Cl^-$] are in the ~0.1 M range, consistent with larger Fick's law driving forces than in the case of $Fe^{2+}$ into ferritin, and hence larger ion fluxes and smaller ion transit times. With our 3D PNP solver, we can simulate steady state conditions of non-equilibrium ion flux down to ca. 0.005M cytoplasmic $Fe^{2+}$. By extrapolation of the I-C curve down to $10^{-5}$ M, we are able to estimate the inward flux through the 3-fold ferritin pores. The ion currents obtained in this manner are indeed much lower than typical currents observed in standard ion channels. Inverting the ion current, we can obtain a crude estimate of the transit time per $Fe^{2+}$ ion. Our computational study has determined this transit time through the 3-fold channels to be in the millisecond time scale regime, consistent with experimental estimates.

Apart from the low concentration of $Fe^{2+}$, there is another factor that strongly influences the long time scales found for $Fe^{2+}$ influx into ferritin in our PNP calculations, namely, the low values of the diffusivity constants that govern motion of ions inside the 3-fold ferritin channels. The FACF analysis performed in this work indicates an extremely large reduction in the bulk water diffusion constant of $Fe^{2+}$ when the ion penetrates deep into the 3-fold ferritin channel. We estimated an average reduction factor of the intra-pore diffusivity of ca. 400. Since the flux of ions according to the NP Equation scales with the diffusivity profile in the flow space (inside the channel), this reduction factor will translate into a similar reduction factor for the ion current, with a corresponding increase in the ion transit time. In standard membrane-spanning ion channels that pass monovalent ions, a reduction in the internal diffusivity relative to the bulk diffusion coefficient by a factor of ca. 10 times is expected for narrow (single file passage) channels, with a less severe reduction occurring in wider channels. Again, this helps to explain the extremely large reduction in ion current obtained for $Fe^{2+}$ influx into ferritin relative to typical ion currents in standard ion channels. We traced the large reduction in ion diffusivity within the channel to two unique features of the ferritin 3-fold pores, namely, i) the existence of two negative rings of charge (from a trio of deprotonated glutamates and a trio of deprotonated aspartates) separated by <5 Å along the channel pore, and ii) a kinking of the pore that occurs in the same region of the channel. We would intuitively expect both features to inhibit ion diffusion through the pore. We would also expect these effects to be enhanced for a divalent ion like $Fe^{2+}$ relative to the behavior of a monovalent ion like $Na^{+}$, due to stronger Coulomb forces experienced by the divalent ion. (These forces will affect both the average force felt on a permeant ion and the magnitude of the temporal fluctuations about the average, thus increasing the size of the random force autocorrelation function and ultimately of the local friction constant.)

Although we were primarily concerned here with the influx of $Fe^{2+}$ into the 3-fold ferritin pore, we also considered the reverse process, i.e., the situation where there is a significant excess of $Fe^{2+}$ in the aqueous cavity that lies inside the protein shell relative to the amount in the cytoplasmic exterior (which is indeed tiny). Such a concentration generates a Fick's Law driving force for expulsion of $Fe^{2+}$ to the cytoplasm through 3-fold pores. The efflux process is less well understood, particularly *in vivo,* as to how and what agents trigger the reduction of $Fe^{2+}$, how electron transfer to the mineral core occurs, etc. However, several experimental studies suggest that $Fe^{2+}$ ions exit to the cytoplasm via the 3 fold pores once the reduction has taken place. (This process may be further regulated by a gating process in which the N terminal part of the bundle acts as a gate that opens or closes to control $Fe^{2+}$ passage through the pore (Tosha et al., 2012)) Interestingly, we found that the current-voltage (I-C) curve for this putative efflux process was quite similar to the corresponding influx curve. This is perhaps surprising given the geometric asymmetry of the 3-fold pore with respect to reflection through a transverse central plane. It may point to the importance of the double ring of negative charges inside the channel described above. Their tendency to attract positive ions into the channel, but not to bind them so strongly that they get permanently stuck inside it, works in a similar fashion for cations entering from either the cytoplasm or the internal mineral cavity (cf. Figure 5.9).

The procedure we have used to estimate ion fluxes and transit times of $Fe^{2+}$ flow through the 3-fold pores of ferritin is not without its flaws. PNP theory is far from exact. It is a mean-field theory, essentially a non-equilibrium version of Poisson-Boltzmann (PB) theory. Correlation effects that are neglected in the mean-field approximation are known in the context of equilibrium PB theory to be significantly more prominent for divalent ions than for multivalent ones (Guldbrand et al., 1984; Duncan et al., 2005). Presumably, a similar situation holds in the non-

equilibrium PNP case. Furthermore, in a PNP calculation we compute ion flux through the channel. We have assumed here that the inverse of the ion flux (# ions passing through the channel per second) gives the time it takes for one ion to pass from entrance to exit of the channel. One can imagine kinetic scenarios where this relation fails. However, if there is a steady flow of ions through the channel and there are not too many binding sites (in ferritin there are 3 binding sites seen in X-ray structures and in MD simulations), the inverse of the current should serve as a rough but reasonable measure of the time scale for a typical ion to move through the channel.

In addition, the primitive form of PNP theory employed here gives only a coarse measure of the molecular level driving forces ("drift forces") that a permeant ion experiences in traversing the channel. We have assumed a simple electrostatic model of these forces. A more accurate measure of the force field experienced by an ion in the channel could be obtained by calculating the single-ion Potential of Mean Force (PMF) from an all-atom simulation. Indeed, this would be a useful next step in studying ion permeation through ferritin. The version of PNP theory employed here also assumes a rigid pore structure which forms a conduit through which mobile ions can move. In fact, our MD simulation indicates that the protein pore (here the 3-fold pore region of ferritin) fluctuates considerably (see, for example, Figures 5.2 and 5.4 of the present study). Some of these fluctuation effects can be folded into a single-ion PMF calculation, which averages explicitly over protein fluctuations, with the net PMF function, say, w(z), inputted as the single-particle potential in an otherwise standard PNP calculation (Mamonov et al., 2003).

Despite its relative simplicity our computational approach has proven successful in reproducing experimentally relevant properties such as the millisecond time scale for $Fe^{2+}$ ion influx from the cytoplasm into the inner cavity. It has also provided insights into the slowness of this influx process compared to analogous processes in standard membrane-spanning ion protein

channel proteins whose permeation pathways bear some structural similarity (e.g., in pore radius, length of the channel, charged amino acid rings that guide select ions into the pore, etc.). Unlike experiments, this approach has enabled us to study the kinetics of iron uptake into ferritin by looking at both the diffusional components and the interactions of the $Fe^{2+}$ ions with the electrostatic gradients inside the channel. Future work will concentrate on improved estimation of drift forces, ion residence times, passage of ions other than $Fe^{2+}$, and other aspects which should provide novel mechanistic details on the atomistic scale to elucidate how ferritin functions *in vivo*.

## 5.5 ACKNOWLEDGEMENTS

This work was supported in part by NSF Grant CHE-0750332, and through TeraGrid resources provided by Pittsburgh Supercomputing Center, NICS, PSC, and TACC.

# 6.0 CONCLUSIONS AND FUTURE DIRECTIONS

The work described in this document encompasses a variety of computational approaches for studying as well as predicting the function of biological ion channels. The three channels discussed in this document presented different opportunities in terms of methodological application.

Since alpha-hemolysin was already a well-studied ion channel in terms of experimental and computational work, it allowed us to explore questions involving the methods, particularly testing the applicability of applying our modified NEMD approach (freezing residues away from the protein-solvent interface), and determining how pH-dependent charge states of titratable residues throughout the channel structure should be treated in computational approaches.

The work in chapter 2 that predicted and examined the effect of the lysine 147 to serine point mutation is one example of the utility of using a computational approach to predict protein function by substitution of amino acid residues, rather than requiring experimental methods such as alanine scanning (Howlander et al., 2010). In particular, it would be useful to apply our NEMD and point mutation approach to the epithelial acid-sensing sodium channel ASC1a, for which there is recently published structural data describing distinct residues forming a selectivity filter (Baconguis et al., 2014).

The work in chapter 3 regarding recalculation of pKa values and partial charges of titratable residues should be followed up with calculations of $\alpha$-HL using BD to verify our PNP results, and then by an application of the method to a narrower channel system, where the electrophysiological characteristics of the system would be more sensitive to partial charges along the channel. In examining a narrower channel, calculation of I-V properties should probably be done using BD,

considering some of the known issues with using PNP in systems with a pore radius less than one Debye length (Corry et al., 2000).

VDAC and Ferritin presented systems with little prior knowledge about their structurally-dependent function. The project described in chapter 4 allowed for us to both determine that the VDAC channel was in the open state as well as propose a gating mechanism for this voltage-dependent channel. Although our proposed mechanism is quite likely not correct, the work has served as a starting point for numerous other studies of this channel (Tejido et al., 2002; Amodeo et al., 2014; Krammer et al., 2015) and leaves opportunity for further study using NEMD or steered molecular dynamics to propose a plausible gating mechanism for this system.

Our work with human H-chain ferritin described in chapter 5 provided an initial investigation of the dynamics of the pathway for $Fe^{2+}$ ions to enter the ferritin protein and will likely serve as a starting point for further investigative work to elucidate chemical processes involving these ions once they gain entry into the protein. It would provide a good opportunity to study kinetics of this system further using quantum mechanics/molecular mechanics, simulating the ion permeation pathway using molecular dynamics, and then addressing chemical reduction of $Fe^{2+}$ at the ferroxidase enzyme with a quantum mechanical approach.

## BIBLIOGRAPHY


Adams J.M., S. Cory. 1998. The Bcl-2 protein family: arbiters of cell survival. *Science.* **281:** 1322–6.

Aguilar, C.M., W.B. De Almeida, and W.R. Rocha. 2007. The electronic spectrum of Fe2+ ion in aqueous solution: A sequential Monte Carlo/quantum mechanical study. *Chemical Physics Letters*. **449**: p. 144-148.

Aksimentiev, A., and Schulten, K. 2005. Imaging a-Hemolysin with Molecular Dynamics: Ionic Conductance, Osmotic Permeability, and the Electrostatic Potential Map. *Biophysical Journal*. **88**: 2745-2761.

Alder, B.J. and T.E. Wainwright. 1957. Phase transition for a hard sphere system. *Journal of Chemical Physics*, **27**: 1208-1209.

Alder, B.J. and T.E. Wainwright. 1959. Studies in Molecular Dynamics I. General Method. *Journal of Chemical Physics*, **31 (2)**: 459-466.

Allen, T.W., O.S. Anderson, B. Roux. 2004. Energetics of ion conduction through the gramicidin channel. *Proc. Nat. Acad. Sci USA* **101**: 117-122.

Amodeo G., M Scorciapino, A. Messina, V. De Pinto, M. Ceccarelli. 2014. Charged residues distribution modulates selectivity of the open state of human isoforms of the voltage dependent anion-selective channel. *PLoS One.* **9**(8) e103879.

Andrews, S.C. 2010. The Ferritin-like superfamily: Evolution of the biological iron storeman from a rubrerythrin-like ancestor. *Biochimica Et Biophysica Acta-General Subjects*. **1800**: p. 691-705.

Arseniev, A.S., I.L. Barsukov, V.F. Bystrov, A.L. Lomize, and A. Ovchinnikov Yu. 1985. 1H-NMR study of gramicidin A transmembrane ion channel. Head-to-head right-handed, single-stranded helices. *FEBS Lett.* **186**: p. 168-174.

Atkins P. and de Paula, J. 2002. Physical Chemistry. Oxford University Press. p. 742.

Baconguis, I, E. Gouaux. 2012. Structural plasticity and dynamic selectivity of acid sensing ion channel–toxin complexes. *Nature.* **489:** 400-405.

Baconguis, I., C. Bohlen, A. Goehring, D. Julius, E. Gouaux. 2014. X-ray structure of acid-sensing ion channel 1–snake toxin complex reveals open state of a $Na^+$-selective channel. *Cell.* **156**(4): 717-729.

Baker N.A., D. Sept, S. Joseph, M.J. Holst, J.A. McCammon. 2001. Electrostatics of nanosystems: application to microtubules and the ribosome. *Proc Natl Acad Sci USA.* **98**: 10037–10041.

Barcilon, V., D. Chen, R.S. Eisenberg, M.A. Ratner. 1993. Barrier crossing with concentration boundary conditions in biological channels and chemical reactions. *J. Chem. Phys.* **98**: 1193-1212.

Barnes, C.M., E.C. Theil, and K.N. Raymond. 2002. Iron uptake in ferritin is blocked by binding of [Cr(Tren)(H2O)(OH)]^2+; a slow dissociating model for [Fe(H2O)6]^2+. *Proceedings of the National Academy of Sciences of the United States of America*. **99**: p. 5195-5200.

Bas, D.C., D.M. Rogers, J.H. Jensen. 2008. Very fast prediction and rationalization of pKa values for protein-ligand complexes. *Proteins* **73(3):** 765-83.

Bashford, D. and M. Karplus. 1990. pKa's of ionizable groups in proteins: Atomic detail from a continuum electrostatic model. *Biochemistry* **29**: 10219–10225.

Bashford, D. and M. Karplus. 1991. Multiple-site titration curves of proteins: An analysis of exact and approximate methods for their calculations. *J. Phys. Chem.* **95**: 9556–9561.

Bathori G., G. Csordas, C. Garcia-Perez, E. Davies, G. Hajnoczky. 2006. Ca2+-dependent control of the permeability properties of the mitochondrial outer membrane and voltage-dependent anion selective channel (VDAC). *J Biol Chem*. **281**: 17347–58.

Bayrhuber M, T. Meins, M. Habeck, S. Becker, K. Giller, S. Villinger, C. Vonrhein, C. Griesinger, M. Zweckstetter, K. Zeth. 2008. Structure of the human voltage-dependent anion channel. *Proc Natl Acad Sci USA.* **105:** 15370–5.

Bean RC, Shepherd WC, Chan H, Eichner J. 1969. Discrete conductance fluctuations in lipid bilayer protein membranes. *J Gen Physiol.* **53**(6):741–757

Bell, J.E., C. Miller. 1984. Effects of phospholipid surface charge on ion conduction in the K+ channel of sarcoplasmic reticulum. *Biophys. J.* **45:** 279–287.

Behera, R.K., H.L. Ng, O. Bhattasali, T. Alber, and E.C. Theil. 2012. Ferritin Protein NanocageIon Channels GATING BY N-TERMINAL EXTENSIONS. *Journal of Biological Chemistry*. **287**: p. 13016-13025.

Berendsen, H. J. C., J. P. M. Postma, W. van Gunsteren, A. DiNola, J.R. Haak. 1984. Molecular dynamics with coupling to an external bath. *J. Chem. Phys.*, **81**: 3684-3690.

Berman, H.M., J. Westbrook, Z. Feng, G. Gilliland, T. N. Bhat, H. Weissig, I. N. Shindyalov, P.E. Bourne1. 2000. The Protein Data Bank. *Nucl. Acids Res.* **28 (1):** 235-242.

Bernstein, F. C., T. F. Koetzle, G. J. Williams, E. F. Meyer, M. D. Brice, J. R. Rogers, O. Kennard, T. Shimanouchi, and M. Tasumi. 1977. The Protein Data Bank: a computer-based archival file for macromolecular structures. *J. Mol. Biol.* **112:** 535–542.

Bertini, I., D. Lalli, S. Mangani, C. Pozzi, C. Rosa, E.C. Theil, and P. Turano. 2012. StructuralInsights into the Ferroxidase Site of Ferritins from Higher Eukaryotes. *Journal of the American Chemical Society.* **134**: p. 6169-6176.

Bezanilla, F. 2006. Ion Channels: From Structure to Function. *Neuron*. **60**: 456-469.

Bezrukov, S.M. and J.J. Kasianowicz. 1993. Current noise reveals protonation kinetics and number of ionizable sites in an open protein ion channel. *Phys. Rev. Lett.* **70**: 2352-2355.

Blachly-Dyson E., S. Peng, M. Colombini, M. Forte. 1990. Selectivity changes in site-directed mutants of the VDAC ion channel: structural implications. *Science.* **247:** 1233–6.

Borisenko, V., M. Sansom, G. A. Woolley. 2000. Protonation of Lysine Residues Inverts Cation/Anion Selectivity in a Model Channel. *Biophys J.* **78:** 1335-1348.

Bou-Abdallah, F., P. Santambrogio, S. Levi, P. Arosio, and N.D. Chasteen. 2005. Unique ironbinding and oxidation properties of human mitochondrial ferritin: A comparative analysis with human H-chain ferritin. *Journal of Molecular Biology*. **347**: p. 543-554.

Bou-Abdallah, F., G.H. Zhao, H.R. Mayne, P. Arosio, and N.D. Chasteen. 2005. Origin of theunusual kinetics of iron deposition in human H-chain ferritin. *Journal of the AmericanChemical Society*. **127**(11): p. 3885-3893.

Bou-Abdallah, F., G. Zhao, G. Biasiotto, M. Poli, P. Arosio, and N.D. Chasteen. 2008. Facilitated Diffusion of Iron(II) and Dioxygen Substrates into Human H-Chain Ferritin. A Fluorescence and Absorbance Study Employing the Ferroxidase Center Substitution Y34W. *Journal of the American Chemical Society*. **130**: p. 17801-17811

Bou-Abdallah, F. 2010. The iron redox and hydrolysis chemistry of the ferritins. *Biochimica EtBiophysica Acta-General Subjects*. **1800**: p. 719-731.

Braha, O., B. Walker, S. Cheley, J.J. Kasianowicz, M.R. Hobaugh, L Song, J.E. Gouaux, H. Bayley. 1997. Structure-based design of a heteromeric transmembrane pore. *Chemistry & Biology* **4**: 497-505.

Brünger, A. T. 1992. X-PLOR, Version 3.1: A System for X-Ray Crystallography and NMR. The Howard Hughes Medical Institute and Department of Molecular Biophysics and Biochemistry, Yale University Press.

Cardenas A.E., R.D. Coalson, M. G. Kurnikova. 2000. Three-dimensional Poisson-Nernst-Planck theory studies: influence of membrane electrostatics on gramicidin A channel conductance. *Biophys J.* **79**: 80–93.

Case, D.A., T.E. Cheatham, III, T. Darden, H. Gohlke, R. Luo, K.M. Merz, Jr., A. Onufriev, C. Simmerling, B. Wang and R. Woods. 2005. The Amber biomolecular simulation programs. *J. Computat. Chem.* **26,** 1668-1688.

Cesar M., J. Wilson. 2004. All three isoforms of the voltage-dependent anion channel (VDAC1,VDAC2, and VDAC3) are present in mitochondria from bovine, rabbit, and rat brain. *Arch Biochem Biophys.* **422:** 191–6.

Ceci, P., G. Di Cecca, M. Falconi, F. Oteri, C. Zamparelli, and E. Chiancone. 2011. Effect of the charge distribution along the "ferritin-like" pores of the proteins from the Dps family on the iron incorporation process. *Journal of Biological Inorganic Chemistry*. **16**: p. 869-880.

Chanda B., O.K. Asamoah, R. Blunck, B. Roux, F. Bezanilla. 2005. Gating charge displacement in voltage gated ion channels involves limited transmembrane movement. *Nature*. **436**: 852–6.

Chandrasekhar, S. 1943. Stochastic problems in physics and astronomy. *Rev Mod Phys*. **15**: p. 1-89.

Chang, TMS. 1964. Semipermeable microcapsules. *Science,* **146**: 524-525.

Chen, D.P., V. Barcilon, R.S. Eisenberg. 1992. Constant fields and constant gradients in open ionic channels. *Biophys. J.* **72**: 1372-1393.

Chen, D.P. and R.S. Eisenberg. 1993. Charges, currents, and potentials in ionic channels of one conformation. *Biophys J.* **64**: 1405-1421.

Cheng, M.H., and R.D. Coalson. 2005. An accurate and efficient empirical approach for calculating the dielectric self energy and ion-ion pair potential in continuum models of biological ion channels. *J. Phys. Chem. B.* **109**: 488–498.

Cheng, M.H., A. Mamonov, J.W. Dukes, and R.D. Coalson. 2007. Modeling the Fast Gating Mechanism in ClC Chloride Channels. *J. Phys. Chem. B.* **111**(5956-5965).

Cheng, M.H., R.D. Coalson, and P. Tang. 2010. Molecular Dynamics and Brownian Dynamics Investigation of Ion Permeation and Anesthetic Halothane Effects on a Proton-Gated Ion Channel. *J. Am. Chem. Soc*. **132**: p. 16442-16449.

Chiu S. W., J. A. Novotny, E. Jakobsson. 1993. The nature of ion and water barrier crossings in a simulated ion channel, *Biophys. J.* **64(1)**: 98-108.

Choudhary, O.P., R. Ujwal, W. Kowallis, R. Coalson, J. Abramson, and M. Grabe. 2010. The electrostatics of VDAC: implications for selectivity and gating. *J. Molec. Biol.* **96**: 580-592.

Chung, S.H., M. Hoyles, T. Allen, and S. Kuyucak. 1998. Study of ion currents across a model membrane channel using Brownian dynamics. *Biophys J.* **75**: 793-809.

Coalson, R.D. and M.G. Kurnikova, 2005. Poisson-Nernst-Planck theory approach to the calculation of current through biological ion channels. *IEEE Trans. Nanobioscience,* **4**: p. 81-93.

Coalson, R.D. and M.G. Kurnikova. 2007. Poisson-Nernst-Planck theory of ion permeation through biological channels in Biological and Medical Physics, Biomedical Engineering, S.H. Chung, O.S. Andersen, and V. Krishnamurthy, Editors. Springer, 233 Spring Street, New York, Ny 10013, United States. p. 449-484.

Coalson, R.D. and M.H. Cheng. 2010. Discrete-State Representation of Ion Permeation Coupled to Fast Gating in a Model of ClC Chloride Channels: Comparison to Multi-Ion ContinuousSpace Brownian Dynamics simulations. *J. Phys. Chem. B.* **114**: p. 1424-33.

Cohen B.E., T. McAnaney, E. Park, Y. Jan, S. Boxer, L. Jan. 2002. Probing protein electrostatics with a synthetic fluorescent amino acid. *Science.* **296:** 1700–3.

Cohen, J, and K. Schulten. 2004. Mechanism of Anionic Conduction Across ClC. *Biophysical Journal*, **86**, 836-845.

Cohen, S.; Chang, A.; Boyer, H.; Helling, R. 1973. Construction of biologically functional bacterial plasmids in vitro. *Proceedings of the National Academy of Sciences of the United States of America.* **70** (11): 3240–3244.

Cole K.S. and H. J. Curtis. 1939. Electric impedance of the squid giant axon during activity. *The Journal of General Physiology*, **22**:649-670.

Cole, K.S., 1949. Dynamic electrical characteristics of the squid axon membrane. *Arch. Sci. Physiol.* **3**: p. 253-258.

Colombini M. 1989. Voltage gating in the mitochondrial channel, VDAC. J Membr Biol. **111:** 103–11.

Colombini M, E. Blachly-Dyson, M. Forte. 1996. VDAC, a channel in the outer mitochondrial membrane. *Ion Channels.* **4**: 169–202.

Cooper, K.E., E. Jakobsson, P. Wolynes. 1985. The theory of ion transport through membrane channels. *Prog. Biophys. Mol. Biol.* **46**: 51-96.

Corry, B., S. Kuyucak, and S.H. Chung. 2000. Tests of continuum theories as models of ion channels. II. Poisson-Nernst-Planck theory versus Brownian Dynamics. *Biophys J.* **78**: 2364-2381.

CRC Handbook of Chemistry and Physics. 1994, Cleveland: CRC Press.

Crichton, R.R. and J.P. Declercq. 2010. X-ray structures of ferritins and related proteins.*Biochimica Et Biophysica Acta-General Subjects.* **1800**: p. 706-718.

Crozier, Paul. S., D. Henderson, R. L. Rowley, D. D. Busath. 2001. Model Channel Ion Currents in NaCl-Extended Simple Point Charge Water Solution with Applied-Field Molecular Dynamics. *Biophys J.* **81**: 3077-3089.

Crozier, P.S., R.L. Rowley, N.B. Holladay, D. Henderson, and D.D. Busath. 2001. Molecular Dynamics Simulation of Continuous Current Flow Through a Model Biological Membrane Channel. *Phys. Rev. Lett.* **86**: 2467.

Darden, T., D. York, and L. Pedersen. 1993. Particle Mesh Ewald. An N_log(N) method for Ewald sums in large systems. *J. Chem. Phys.* **98**: 10089–10092.

Day T., A. Soudackov, M. Cuma, U. Schmitt, G. Voth. 2002. A Second Generation Multi-State Empirical Valence Bond Model for Proton Transport in Aqueous Systems. *J. Chem. Phys.* **117**: 5839-5849

de Levie, R., N.G. Seidah, and H. Moreira. 1972. Transport of ions of one kind through thin membranes. I. Nonequilibrium steady-state behavior. J. *Membr. Biol.* **10**: p. 171-192.

De Pinto V, O. Ludwig, J. Krause, R. Benz, F. Palmieri. 1987. Porin pores of mitochondrial outer membranes from high and low eukaryotic cells: biochemical and biophysical characterization. *Biochim Biophys Acta.* **894:** 109–19.

De Pinto V., G. Prezioso, F. Thinnes, T.A. Link, F. Palmieri. 1991. Peptide-specific antibodies and proteases as probes of the transmembrane topology of the bovine heart mitochondrial porin. Biochemistry. **30**: 10191–200.

d'Estaintot, B.L., S. Paolo, T. Granier, B. Gallois, J.M. Chevalier, G. Precigoux, S. Levi, and P. Arosio. 2004. Crystal structure and biochemical properties of the human mitochondrial ferritin and its mutant Ser144Ala. *Journal of Molecular Biology.* **340**: p. 277-293.

Di Russo, N., D. Estrin, M. Martı´, A. Roitberg. 2012. pH-Dependent Conformational Changes in Proteins and Their Effect on Experimental pKas: The Case of Nitrophorin. *PLOS Comp. Biol.* **8 (11):** 1-9.

Dobson, C.M. 2003. Protein Folding and Misfolding. *Nature.* **426:** 884-890.

Dolinsky T.J., J.E. Nielsen, J.A. McCammon, N.A. Baker. 2004. PDB2PQR: an automated pipeline for the setup of Poisson-Boltzmann electrostatics calculations. *Nucleic Acids Res*. **32**:W665–7.

Donnini, S., R. T. Ullmann, G. Groenhof, H. Grubmüller. 2016. Charge-Neutral Constant pH Molecular Dynamics Simulations Using a Parsimonious Proton Buffer. *J Chem. Theory Comp.* **12:** 1040-1051.

Douglas, T. and D.R. Ripoll. 1998. Calculated electrostatic gradients in recombinant human H-chain ferritin. *Protein Science*. **7**: p. 1083-1091.

Doyle DA, J. Morais Cabral, R. Pfuetzner, A. Kuo, J. Gulbis, S. Cohen, B. Chait, R. MacKinnon. 1998. The structure of the potassium channel: molecular basis of K+ conduction and selectivity. *Science.* **280:** 69–77.

Duncan, A., R.D. Sedgewick, and R.D. Coalson. 2005. Improved Local Lattice Approach for Coulombic Simulations. *Phys. Rev. E*. **71**: p. 046702:1-8.

Dutzler, R, E. B. Campbell, M. Cadene, B. T. Chait, & R. MacKinnon. 2002. X-ray structure of a ClC chloride channel at 3.0 Å reveals the molecular basis of anion selectivity. *Nature.* **415**: 287-294.

Dutzler, R., E. B. Campbell, M. Cadene, and R. MacKinnon. 2003. Gating the selectivity filter in ClC chloride channels. *Science.* **300**: 108-12.

Ebrahimi, K.H., E. Bill, P.-L. Hagedoorn, and W.R. Hagen. 2012. The catalytic center of ferritin regulates iron storage via Fe(II)-Fe(III) displacement. *Nature Chemical Biology*. **8**(11): p. 941-948.

Edelheit, O., I. Hanukoglu, N. Dascal, A. Hanukoglu. 2011. "Identification of the roles of conserved charged residues in the extracellular domain of an epithelial sodium channel (ENaC) subunit by alanine mutagenesis". *Am. J. Physiol. Renal Physiol.* **300** (4): F887–97.

Egwolf, B., Y. Luo, D. E. Walters, and B. Roux. 2010. Ion selectivity of alpha-hemolysin with beta-cyclodextrin adapter. II. Multi-ion effects studied with grand canonical Monte Carlo/Brownian dynamics simulations. The journal of physical chemistry **114:** 2901-2909.

Einstein, A.(1905). "Über die von der molekularkinetischen Theorie der Wärme geforderte Bewegung von in ruhenden Flüssigkeiten suspendierten Teilchen" (PDF). Annalen der Physik (in German) 322 (8): 549–560.

Eisenberg, R.S., M.M. Klosek, Z. Schuss. 1995. Diffusion as a chemical reaction: Stochastic Trajectories between fixed concentrations. *J. Chem. Phys.* **102**: 1767-1780.

Eisenberg, R.S. 1996. Computing the field in proteins and channels. *J. Membrane Biol*. **150**:p. 1-25.

Elinder, F. Nilsson, J, Arhem, P. 2007. On the opening of voltage-gated ion channels. *Physiology & Behavior* **92,** 1–7.

Ermak, D.L. and J.A. McCammon. 1978. Brownian dynamics with hydrodynamic interactions. *J. Chem. Phys.* **69:** p. 1352-1360.

Feller, S. E., Y. H. Zhang, R. W. Pastor, and B. R. Brooks. 1995. Constant pressure molecular dynamics simulation—the Langevin piston method. *J. Chem. Phys.* **103:** 4613–4621.

Feller, S. E., and A. MacKerell. 2000. An improved empirical potential energy function for molecular simulations of phospholipids. *J. Phys. Chem. B.* **104**: 7510–7515.

Fitch C.A., D. A. Karp, K. Lee, W. Stites, E. Lattman, B. Garcı´a-Moreno. 2002. Experimental pKa Values of Buried Residues: Analysis with Continuum Methods and Role of Water Penetration. *Biophys J.* **82:** 3289–3304.

Ford, J. 1973. The Transition from Analytic Dynamics to Statistical Mechanics. *Adv. Chem. Phys.* **24**: 155-158.

Forsyth W.R., M.K. Gilson, J. Antosiewicz, O. Jaren, A.D. Robertson. 1998. Theoretical and experimental analysis of ionization equilibria in ovomucoid third domain. *Biochemistry* **37:** 8643–8652.

Forsyth W.R., A. Robertson. 2000. Insensitivity of perturbed carboxyl pKa values in the ovomucoid third domain to charge replacement at a neighboring residue. *Biochemistry.* **39:** 8067–8072.

Funk, F., J.P. Lenders, R.R. Crichton, and W. Schneider. 1985. Reductive mobilisation of Ferritin Iron. *Eur. J. Biochem*. **52**: p. 167-172.

Galluzzi L, O. Kepp, N. Tajeddine, G. Kroemer. 2008. Disruption of the hexokinase-VDAC complex for tumor therapy. *Oncogene.* **27:** 4633–5.

Goldman, D.E. 1943. Potential, impedance, and rectification in membranes. *J. Gen. Physiol*, **27:** p. 37-60.

Gouaux, J.E., O. Braha, M.R. Hobaugh, L.Z. Song, S. Cheley, C. Shustak, H. Bayley. 1994. Stochastic Stoichiometry of Staphylococcal alpha-hemolysin in crystals and on membranes – a heptameric transmembrane pore. *Proc. Natl. Acad. Sci.* **91**: 12828-12931.

Gouaux, J.E. 1998. α-hemolysin from *Staphylococcus aureus*: An archetype of β-barrel, channel-forming toxins. *J. Struct. Biol.* **121**: 110-122.

Grabe M., H. Lecar, Y.N. Jan, L.Y. Jan. 2004. A quantitative assessment of models for voltage-dependent gating of ion channels. *Proc Natl Acad Sci USA*. **101**: 17640–5.

Grabe M., D. Bichet, X. Qian, Y. Jan, L. Jan. 2006. K+ channel selectivity depends on kinetic as well as thermodynamic factors. *Proc Natl Acad Sci USA*. **103:** 14361–6.

Graf, P., A. Nitzan, M. G. Kurnikova, and R. D. Coalson. 2000. A dynamic lattice Monte Carlo model of ion transport in inhomogeneous dielectric environments: Method and implementation. *J. Phys. Chem. B* **104**: 12324-12338.

Graf P., M.G. Kurnikova, R.D. Coalson, A. Nitzan. 2004. Comparison of dynamic lattice Monte Carlo simulations and the dielectric self-energy Poisson-Nernst-Planck continuum theory for model ion channels. *J Phys Chem B.* **108**: 2006–2015.

Grubmüller, H. 1996. SOLVATE 1.0. http://www.mpibpc.gwdg.de/abteilungen/071/solvate/docu.html.

Gu, L. Q., and H. Bayley. 2000. Interaction of the noncovalent molecular adapter, beta-cyclodextrin, with the staphylococcal alpha-hemolysin pore. *Biophys. J.* **79**: 1967–1975.

Gu, L. Q., S. Cheley, and H. Bayley. 2001. Prolonged residence time of a noncovalent molecular adapter, *β*-cyclodextrin, within the lumen of mutant *α*-hemolysin pores. *J. Gen. Physiol.* **118**:481–493.

Gu, L. Q., M. Dalla Serra, J. B. Vincent, G. Vigh, S. Cheley, O. Braha, and H. Bayley. 2001. Reversal of charge selectivity in transmembrane protein pores by using noncovalent molecular adapters. *Proc. Natl. Acad. Sci. USA*. **97**: 3959–3964.

Guldbrand, L., B. Jönsson, H. Wennerströmm , and P. Linse. 1984. Electrical double layer forces. A Monte Carlo study. *J. Chem. Phys.* **80**: p. 2221 - 2228.

Guo X.W., P.R. Smith, B. Cognon, D. D'Arcangelis, E. Dolginova, C. Mannella. 1995. Molecular design of the voltage-dependent, anion-selective channel in the mitochondrial outer membrane. *J Struct Biol.* **114:** 41–59.

Haldar, S., L.E. Bevers, T. Tosha, and E.C. Theil. 2011. Moving Iron through Ferritin Protein Nanocages Depends on Residues throughout Each Four alpha-Helix Bundle Subunit. *Journal of Biological Chemistry.* **286**: p. 25620-25627.

Hamill, O.P., A. Marty, E. Neher, B. Sakmann, and F.J. Sigworth. 1981. Improved patch-clamp techniques for high-resolution current recording from cells and cell-free membrane patches. *Pflugers Arch.,* **391**: p. 85-100.

Harada, T. and H. Yoshimura. 2013. Ferritin protein encapsulated photoluminescent rare earth nanoparticle. *Journal of Applied Physics.* **114**.

Hempstead, P.D., S.J. Yewdall, A.R. Fernie, D.M. Lawson, P.J. Artymiuk, D.W. Rice, G.C. Ford, and P.M. Harrison. 1997. Comparison of the three-dimensional structures of recombinant human H and horse L ferritins at high resolution. *Journal of Molecular Biology*. **268**: p. 424-448.

Henderson, L.J. 1908. Concerning the relationship between the strength of acids and their capacity to preserve neutrality. *Am. J. Physiol.* **21 (4):** 173–179.

Henderson, D., D.D. Busath, R.L. Rowley, P.S. Crozier, and D. Boda, 2001. Simulation study of channels in biological membranes. *Proceedings of the International Conference on Computaional Nanoscience*, pp. 45-48.

Hille, B. 2001. Ion channels of excitable membranes. 3. Sinauer; Sunderland, Mass:

Hiller S., r. Garces, T. Malia, V. Orekhov, M. Colombini, G. Wagner. 2008. Solution structure of the integral human membrane protein VDAC-1 in detergent micelles. *Science.* **321:** 1206–10.

Hilton, R.J., B. Zhang, L.N. Martineau, G.D. Watt, and R.K. Watt. 2012. Anion deposition into ferritin. *Journal of Inorganic Biochemistry*. **108**: p. 8-14.

Hinsch KD, V. De Pinto, V. Aires, X. Schneider, A. Messina, E. Hinsch. 2004. Voltage-dependent anionselective channels VDAC2 and VDAC3 are abundant proteins in bovine outer dense fibers, a cytoskeletal component of the sperm flagellum. *J Biol Chem.* **279**: 15281–8.

Hodgkin, A.L., A.F. Huxley, and B. Katz, 1949. Ionic currents underlying activity in the giant axon of the squid. *Arch. Sci. Physiol*, **3**: 129-150.

Hodgkin, A.L. and A.F. Huxley, 1952a. Currents carried by sodium and potassium ions through the membrane of the giant axon of Loligo. *J. Physiol. (Lond.)*, **116**: p. 449-472.

Hodgkin, A.L. and A.F. Huxley, 1952b. The components of membrane conductance in the giant axon of Loligo. *J. Physiol. (Lond.),* **116:** p. 473-496.

Hodgkin, A.L. and B. Katz. 1949. The effect of sodium ions on the electrical activity of the giant axon of the squid. *J. Physiol. (Lond.)* **108**: p. 37-77.

Hollerbach, U., D.P. Chen, D.D. Busath, and B. Eisenberg. 2000. Predicting function from structure using the Poisson-Nernst-Planck equations: Sodium current in the gramicidin A channel. *Langmuir.* **16**: p. 5509-5514.

Hoogenboom B.W., K. Suda, A. Engel, D. Fotiadis. 2007. The supramolecular assemblies of voltage dependent anion channels in the native membrane. *J Mol Biol.* **370:** 246–55.

Hoover, W. G. 1985. Canonical Dynamics: Equilibrium Phase-Space Distributions. *Phys. Rev. A*, **31**: 1695.

Howlader, M.T., Y Kagawa, A Miyakawa, A Yamamoto, T. Taniguchi , T. Hayakawa, H. Sakai. 2010. Alanine scanning analyses of the three major loops in domain II of Bacillus thuringiensis mosquitocidal toxin Cry4Aa. *Appl. Environ. Microbiol.* **76** (3): 860–5.

Humphrey W., A. Dalke, K. Schulten. 1996. VMD: visual molecular dynamics. *J Mol Graph*. **14**: 33–8. 27–8.

Hutchison, C. A., S. Phillips, M. H. Edgell, S. Gillam, P. Jahnke, M. Smith. 1978. Mutagenesis at a Specific Position In a DNA Sequence. *J Biol Chem.* **253**(18): 6551-60.

Im W, B. Roux. 2002. Ion permeation and selectivity of OmpF porin: a theoretical study based on molecular dynamics, Brownian dynamics, and continuum electrodiffusion theory. *J Mol Biol.* **322**: 851–69.

Imoto, K., C. Busch, B. Sakmann, M. Mishina, T. Konno, J. Nakai, H. Bujo, Y. Mori, K. Fukuda, and S. Numa. 1988. Rings of negatively charged amino acids determine the acetylcholine receptor channel conductance. *Nature*, **335**: p. 645-648.

Islas L.D., F.J. Sigworth. 2001. Electrostatics and the gating pore of Shaker potassium channels. *J Gen Phys.* **117**: 69–89.

Jackson, D.; Symons, R.; Berg, P. 1972. Biochemical method for inserting new genetic information into DNA of Simian Virus 40: Circular SV40 DNA molecules containing lambda phage genes and the galactose operon of Escherichia coli. *Proceedings of the National Academy of Sciences of the United States of America.* **69** (10): 2904–2909.

Jin, W.L., H. Takagi, B. Pancorbo, and E.C. Theil. 2001. "Opening" the ferritin pore for iron release by mutation of conserved amino acids at interhelix and loop sites. *Biochemistry.* **40**: p. 7525-7532.

Jo S., T. Kim, V.G. Iyer, W. Im. 2008. CHARMM-GUI: a web-based graphical user interface for CHARMM. *J Comput Chem.* **29**:1859–1865.

Jordan, P.C. 1982. Electrostatic modeling of ion pores. Energy barriers and electric field profiles. *Biophys. J.* **39**: 157-164.

Jordan, P.C. 1983. Electrostatic modeling of ion pores. II. Effects attributable to the membrane dipole potential profile. *Biophys. J.* **41**: 189-195.

Jordan, P.C. 1984. Effect of pore structure on energy barriers and applied voltage profiles. I. Symmetrical channels. *Biophys. J.* **45:** 1091-1100.

Jordan, P.C. 1984 . Effect of pore structure on energy barriers and applied voltage profiles. II. Unsymmetrical channels. *Biophys J.* **45**: 1101-1107.

Jordan, P.C. 1987. Microscopic approaches to ion transport through transmembrane channels. The model system gramicidin. *J. Phys. Chem.* **91**: 6582-6591.

Kale L, Skeel R, Bhandarkar M, Brunner R, Gursoy A, Krawetz N, Phillips J, Shinozaki A, Varadarajan K, Schulten K. 1999. NAMD2: Greater scalability for parallel molecular dynamics. *J Comp Phys*. **151**: 283–312.

Kang, Y.J., M. Uchida, H.H. Shin, T. Douglas, and S. Kang. 2011. Biomimetic FePt nanoparticle synthesis within Pyrococcus furiosus ferritins and their layer-by-layer formation. *Soft Matter*. **7**: p. 11078-11081.

Kasianowicz, J.J. 1994. Voltage-dependent gating kinetics of an ion channel modulated by ionic strength. *Biophys. J.* **66:** A430

Kasianowicz, J.J., S.M. Bezrukov. 1995. Protonation dynamics of the α-toxin ion channel from spectral analysis of pH dependent current fluctuations. *Biophys. J.* **69**: 94-105.

Kasyutich, O., A. Ilari, A. Fiorillo, D. Tatchev, A. Hoell, and P. Ceci. 2010. Silver Ion Incorporation and Nanoparticle Formation inside the Cavity of Pyrococcus furiosus Ferritin: Structural and Size-Distribution Analyses. *Journal of the American Chemical Society*. **132**: p. 3621-3627.

Kendrew J. C., Parrish R. G. 1957. The Crystal Structure of Myoglobin. III. Sperm-Whale Myoglobin. *Proc. Roy. Soc. A* **238:** 305–324.

Kendrew JC, Bodo G, Dintzis HM, Parrish RG, Wyckoff H, Phillips DC. 1958. A three-dimensional model of the myoglobin molecule obtained by x-ray analysis. *Nature*. **181**: 662-6.

Keyes, J.D., R.J. Hilton, J. Farrer, and R.K. Watt. 2011. Ferritin as a photocatalyst and scaffold for gold nanoparticle synthesis. *Journal of Nanoparticle Research.* **13**: p. 2563-2575.

Khalili-Arghi, F., B. Ziervogel, J.C. Gumart, and B. Roux. 2013. Molecular Dynammics Simulations of Membrane Proteins Under Asymmetric Ionic Concentrations. *J. Gen. Physiol.*, **142:** p. 465-475.

Kim, J.-W., S.H. Choi, P.T. Lillehei, S.-H. Chu, G.C. King, and G.D. Watt. 2007. Electrochemically controlled reconstitution of immobilized ferritins for bioelectronic applications. *Journal of Electroanalytical Chemistry*. **601**: p. 8-16.

Kim, J.W., A.E. Posey, G.D. Watt, S.H. Choi, and P.T. Lillehei. 2010. Gold Nanoshell Assembly on a Ferritin Protein Employed as a Bio-Template. *Journal of Nanoscience and Nanotechnology*. **10**: p. 1771-1777.

Koneshan, S., R.M. Lynden-Bell, and J.C. Rasaiah. 1998. Friction Coeficients of Ions in Aqueous Solution at 25C. *J. Am. Chem. Soc*. **120**: p. 12041-12050.

Koppel D.A., K. Kinnally, P. Masters, M. Forte, E. Blachly-Dyson, C. Mannella. 1998. Bacterial expression and characterization of the mitochondrial outer membrane channel. Effects of n-terminal modifications. *J Biol Chem.* **273:** 13794–800.

Kozlov, A., T. Lohman. 2000. Large contributions of coupled protonation equilibria to the observed enthalpy and heat capacity changes for ssDNA binding to Escherichia coli SSB protein. *Proteins* **4:** 8-22.

Krasilnikov, O.V., R.Z. Sabirov. 1989. Ion transport through channels formed in lipid bilayers by Staphylococcus aureus alpha-toxin. *Gen. Physiol. Biophys.* **8:** 213–222.

Kubo, R. 1996. Many-Body Theory. 1966, Tokyo: Syokabo and Benjamin.

Kumar, S., D. Bouzida, R. H. Swendsen, P. A. Kollman, & J. M. Rosenberg, 1992. Molecular dynamics simulations suggest that the Eco RI kink is an example of molecular strain. *J. Comp. Chem.* **13**: 1011-1021.

Kurnikova M.G., R.D. Coalson, P. Graf, A. Nitzan. 1999. A lattice relaxation algorithm for three-dimensional Poisson-Nernst-Planck theory with application to ion transport through the gramicidin A channel. *Biophys J.* **76**: 642–56.

Kutzner, C., H. Grubmuller, B.L. de Groot, U. Zachariae, 2011, Computational Electrophysiology: The Molecular Dynamics of Ion Channel Permeation and Selectivity in Atomistic Detail. *Biophys J.* **101:** p. 809-817.

Laghaei, R., D.G. Evans, and R.D. Coalson. 2013. Metal binding sites of human H-chain ferritin and iron transport mechanism to the ferroxidase sites: A molecular dynamics simulation study. *Proteins-Structure Function and Bioinformatics*. **81**: p. 1042-1050.

Laurents D.V., Huyghues-Despointes B.M.P., Bruix M., Thurlkill R.L., Schell D., Newsom S., Grimsley G.R., Shaw K.L., Trevino S., Rico M. 2003. Charge-charge interactions are key determinants of the pK values of ionizable groups in ribonuclease Sa (pI _ 3.5) and a basic variant (pI _ 10.2). *J Mol Biol.* **325:** 1077–1092.

Levitt, D.G. 1999. Modeling ion channels. *J. Gen. Physiol.* **113**: 789-794.

Li, H., A.D. Robertson, J.H. Jensen. 2005. Very fast empirical prediction and rationalization of protein pKa values. *Proteins* **61(4):** 704-21.

Lindemann, B. 1982. Dependence of ion flow through channels on the density of fixed charges at the channel opening. *Biophys. J.* **39**: 15–22

Liu, X.F., W.L. Jin, and E.C. Theil. 2003. Opening protein pores with chaotropes enhances Fe reduction and chelation of Fe from the ferritin biomineral. *Proceedings of the National Academy of Sciences of the United States of America*. **100**(7): p. 3653-3658.

Liu, X.S., L.D. Patterson, M.J. Miller, and E.C. Theil. 2007. Peptides selected for the protein nanocage pores change the rate of iron recovery from the ferritin mineral. *Journal of Biological Chemistry.* **282**: p. 31821-31825.

Luo, Y., B. Egwolf, D. E. Walters, and B. Roux. 2010. Ion selectivity of alpha-hemolysin with a beta-cyclodextrin adapter. I. Single ion potential of mean force and diffusion coefficient. The journal of physical chemistry **114**: 952-958.

Lutter R., Abrahams J. P., Vanraaij M. J., Todd R. J., Lundqvist T., Buchanan S. K., Leslie A. G. W., Walker J. E. 1993. Crystallization of F1-ATPase from Bovine Heart Mitochondria. *J. Mol. Biol.* **229**:787–790.

Mackay, D.H.J., P.H. Berens, and K.R. Wilson. 1984. Structure and dynamics of ion transport through Gramicidin A. *Biophys. J.*, **46**: p. 229-248.

MacKerrell, A.D.J., B. Brooks, C.L.I. Brooks, L. Nilsson, B. Roux, Y. Won, and M. Karplus. 1998. CHARMM: The Energy Function and Its Parameterization with an Overview of the Program. The Encyclopedia of Computational Chemistry, ed. P.v.R. Schleyer. Vol. 1. Chichester: John Wiley & Sons.

Mamonov, A., R. D. Coalson, A. Nitzan and M. G. Kurnikova. 2003. The Role of the Dielectric Barrier in Narrow Biological Channels: a Novel Composite Approach to Modeling Single Channel Currents, *Biophys. J.* **84(6)**: 3646-3661.

Mamonov, A., R. D. Coalson, and M. G. Kurnikova. 2006. Diffusion constant of K+ inside Gramicidin A: a comparative study of four computational methods. *Biophys. Chem.* **124(3)**: 268-78.

Mann, Michael D. 1997. The Nervous System in Action. http://michaeldmann.net. p. 3-5

Mannella CA. 1982. Structure of the outer mitochondrial membrane: ordered arrays of porelike subunits in outer-membrane fractions from Neurospora crassa mitochondria. *J Cell Biol.* **94:** 680–7.

Mannella C.A. 1998. Conformational changes in the mitochondrial channel protein, VDAC, and their functional implications. *J Struct Biol.* **121**:207–18.

May, C.A., J.K. Grady, T.M. Laue, M. Poli, P. Arosio, and N.D. Chasteen. 2010. The sedimentation properties of ferritins. New insights and analysis of methods of nanoparticle preparation.

McCammon, J.A., Gelin, B.R., Karplus, M. 1977. Dynamics of folded protiens. *Nature (London)*, **267**: 585-590.

McDonald B.M., M.M. Wydro, R. Lightowlers, J. Lakey. 2009. Probing the orientation of yeast VDAC1 in vivo. *FEBS Lett*. **583**: 739–42.

McPherson A. 1999. Crystallization of Biological Molecules (Cold Spring Harbor Laboratory, Cold Spring Harbor, NY).

McQuarrie, D.A. 1976. Statistical Mechanics. Harper Collins Publishers, New York. p. 514.

Menestrina, G. 1986. Ionic channels formed by *Staphylococcus aureus* alpha-toxin: Voltage-dependent inhibition by divalent and trivalent cations. *J. Membr. Biol.* **90**: 177-190.

Miles, G., H. Bayley, and S. Cheley. 2002. Properties of Bacillus cereus hemolysin II: a heptameric transmembrane pore. *Protein Sci.* **11**: 1813–1824.

Miller, C. 1982. Open-State Substructure of Single Chloride Channels from Torpedo Electroplax. *Phil. Trans. Roy. Soc. Lon. B.* **299**: 401-411.

Miloshevsky, G.V. and P.C. Jordan. 2004 Permeation in ion channels: the interplay of structure and theory. *Trends in Neurosciences*, **27:** p. 308-314.

Misakian M. and J. J. Kasianowicz. 2003. Electrostatic control of ion transport through the α-hemolysin channel. *Journal of Membrane Biology*, **195 (3)**: 137-146.

Muirhead H, Perutz MF. Structure of haemoglobin. 1963. A three-dimensional Fourier synthesis of reduced human haemoglobin at 5.5 Å resolution. *Nature*. **199**: 633-8.

Neher, E and B. Sakmann. 1976. Noise analysis of drug induced voltage clamp currents in denervated frog muscle fibres. *The Journal of Physiology*, **258 (3)**: 705-729.

Nernst, W. 1888. Zur kinetik der in losung befindlichen korper: theorie der diffusion. *Z. Phys. Chem.*, **4**: p. 613-637.

Noda, M., H. Takahashi, T. Tanabe, M. Toyosato, Y. Furutani, T. Hirose, M. Asai, S. Inayama, T. Miyata, and S. Numa. 1982. Primary structure of alpha-subunit precursor of Torpedo californica acetylcholine receptor deduced from cDNA sequence. *Nature*, **299**: p. 793-797.

Noda, M., Y. Furitani, H.Takahashi et al. (11 co-authors). 1983. Cloning and sequence analysis of calf cDNA and human genomic DNA encoding alpha-subunit precursor of muscle acetylcholine receptor. *Nature* **305:** 818–823.

Nose, S. 1984. A unified formulation of the constant temperature molecular dynamic method. *J. Chem. Phys.*, **81**: 511-519.

Noskov S.Y., S. Bernèche, B. Roux. 2004. Control of ion selectivity in potassium channels by electrostatic and dynamic properties of carbonyl ligands. *Nature*. **431**: 830–4.

Noskov S.Y., W. Im, B. Roux. 2004. Ion permeation through the alpha-hemolysin channel: theoretical studies based on Brownian dynamics and Poisson-Nernst-Plank electrodiffusion theory. *Biophys J.* **87**: 2299–309.

Numa, S., M. Noda, H.Takahashi, T.Tanabe, M.Toyosato,Y. Furutani, and S. Kikyotani. 1983. Molecular structure of the nicotinic acetylcholine receptor. *Cold Spring Harb. Symp. Quant. Biol.* **48:** 57–69.

O'Keeffe JT, Cozmuta I, Bose D, Stolc V. A predictive MD-Nernst–Planck model for transport in Alpha-Hemolysin: Modeling anisotropic ion currents. Chemical Physics 2007; **342(6)**: 25–32.

Onufreiv, A., and E. Alexov. 2013. Protonation and pK changes in protein-ligand binding. *Q Rev Biophys.* **46**(2): 181–209.

Ostermeier C., Iwata S., Ludwig B., Michel H. 1995. Fv fragment-mediated crystallization of the membrane protein bacterial cytochrome c oxidase. *Nat. Struct. Biol.* **2:** 842–846.

Pace, C.N., G. Grimsley, J. M. Scholtz. 2009. Protein Ionizable Groups: pK Values and Their Contribution to Protein Stability and Solubility. *J. Biol. Chem.* **284 (20):** 13285-13289.

Paques, E.P., A. Paques, and R.R. Chriton. 1979. A Kinetic Study of the Mechanism of Ferritin Formation: The Effects of Buffer, of pH, and of the Iron Content of the Molecule. *J. Mol. Catal*. **5**: p. 363-375.

Passiniemi, P. 1983. Accurate Tracer Diffusion Coefficients of NA+ and Cl- Ions in Dilute Aqueous Sodium Chloride Solutions Measured with the Closed Capillary Method. *J. Sol. Chem*. **12**: p. 801-813.

Phillips, J.C., R. Braun, W. Wang, J. Gumbart, E. Tajkhorshid, E. Villa, C. Chipot, R.D. Skeel, L. Kale, and K. Schulten. 2005. Scalable Molecular Dynamics with NAMD. *Comput. Chem*. **26**: p. 1781-1802.

Planck, M. 1890. Ueber die erregung von elektricitat und warme in elektrolyten. *Ann. Phys. Chem., Neue. Folge.* **39:** p. 161-186.

Platzer, G., M. Okon, L. McIntosh. 2014. pH-dependent random coil $^{1}H$, $^{13}C$, and $^{15}N$ chemical shifts of the ionizable amino acids: a guide for protein pKa measurements. *J. Biomol. NMR.* **60(2):** 109-129.

Polanams, J., A.D. Ray, and R.K. Watt. 2005. Nanophase iron phosphate, iron arsenate, iron vanadate, and iron molybdate minerals synthesized within the protein cage of ferritin. *Inorganic Chemistry*. **44**: p. 3203-3209.

Popp B., D. Court, R. Benz, W. Neupert, R. Lill. The role of the N and C termini of recombinant Neurospora mitochondrial porin in channel formation and voltage-dependent gating. *J Biol Chem.* **271**:13593–9.

Prod'hom, B., D. Pietrobon, P. Hess. 1987. Direct measurements of proton transfer rates to a group controlling the dihydropyridine- sensitive Ca2+ channel. *Nature* **329**: 243–246.

Que, Lawrence Jr. 2000. Physical Methods in Bioinorganic Chemistry: Spectroscopy and Magnetism. Sausalito, CA: University Science Books. pp. 59–120.

Rahman, A. 1964. Correlations in the Motion of Atoms in Liquid Argon. *Physical Review A,* **136**: 405-411.

Riordan, J.R., Rommens, J.M., Kerem, B., Alon, N., Rozmahel, R., Grzelczak, Z., Zielenski, J., Lok, S., Plavsic, N., Chou, J.L. et al. 1989. Identification of the cystic fibrosis gene: cloning and characterization of complementary DNA. *Science*, **245**, 1066–1073.

Root, M.J., R. MacKinnon. 1994. Two identical noninteracting sites in an ion channel revealed by proton transfer. *Science* **265**:1852–1856.

Rostovtseva T, M. Colombini. 1997. VDAC channels mediate and gate the flow of ATP: implications for the regulation of mitochondrial function. *Biophys J.* **72:** 1954–62.

Rostovtseva, T.K., T. Liu, M. Colombini, V. Parsegian, S. Bezrukov. 2000. Positive cooperativity without domains or subunits in monomeric membrane channel. *Proc. Nat. Acad. Sci. USA* **97**: 7819–7822.

Roux, B. and M. Karplus. 1991. Ion transport in a Gramicidin-like channel: dynamics and mobility. *J. Phys. Chem*. **95**: p. 4856-4868.

Roux B. 1997. Influence of the membrane potential on the free energy of an intrinsic protein. *Biophys J.* **73**: 2980–9.

Roux B, MacKinnon R. 1999. The cavity and pore helices in the KcsA K+ channel: electrostatic stabilization of monovalent cations. *Science.* **285:** 100–2.

Sampson MJ, W. Decker, A. Beaudet, W. Ruitenbeek, D. Armstrong, M Hicks, W Craigen. 2001. Immotile sperm and infertility in mice lacking mitochondrial voltage-dependent anion channel type 3. *J Biol Chem.* **276:** 39206–12.

Schaefer, M., M. Sommer, and M. Karplus. 1997. pH-Dependence of protein stability: Absolute electrostatic free energy differences between conformations. *J. Phys. Chem. B* **101**: 1663–1683.

Schein SJ, M Colombini,A Finkelstein. 1976. Reconstitution in planar lipid bilayers of a voltage dependent anion-selective channel obtained from paramecium mitochondria. *J Membr Biol.* **30**: 99–120.

Schlenkrich, M., J. Brickmann, A. D. MacKerell, Jr., and M. Karplus. 1996. Empirical potential energy function for phospholipids: criteria for parameter optimization and applications. In Biological Membranes: A Molecular Perspective from Computation and Experiment. K. M. Merz, and B. Roux, editors. Birkhauser, Boston, MA. 31–81.

Schoppa NE, McCormack K, Tanouye MA, Sigworth FJ. 1992. The size of gating charge in wild-type and mutant Shaker potassium channels. *Science*. **255**: 1712–5.

Schrödinger LLC., The PyMOL Molecular Graphics System, version 1.3r1. Schrödinger, LLC, Portland, OR. **http://www.pymol.org/pymol**..

Schutz CN, A. Warshel. 2001. What are the dielectric "constants" of proteins and how to validate electrostatic models? *Proteins.* **44:** 400–17.

Shelley, J. C., M. Y. Shelley, R. C. Reeder, S. Bandyopadhyay, M. L. Klein. 2001. A Coarse Grain Model for Phospholipid Simulations. *J. Phys. Chem. B***, 105**: 4464-4470.

Shimizu S, M. Narita, Y. Tsujimoto. 1999. Bcl-2 family proteins regulate the release of apoptogenic cytochrome c by the mitochondrial channel VDAC. *Nature.* **399:** 483–7.

Shin, K.M., R.K. Watt, G.D. Watt, S.H. Choi, H.-H. Kim, S.I. Kim, and S.J. Kim. 2010. Characterization of ferritin core on redox reactions as a nanocomposite for electron transfer. *Electrochimica Acta.* **55**: p. 3486-3490.

Sitkoff D., N. BenTal, B. Honig. 1996. Calculation of alkane to water solvation free energies using continuum solvent models. *J Phys Chem.* **100**:2744–2752.

Smart, O.S., J.G. Neduvelil, X. Wang, B.A. Wallace, and M.S. Sansom. 1996. HOLE: A Program for the Analysis of the Pore Dimensions of Ion Channel Structural Models. *J. Mol. Graphics*. **14**: p. 354-360.

Song J., C. Midson, E. Blachly-Dyson, M. Forte, M. Colombini. 1998. The sensor regions of VDAC are translocated from within the membrane to the surface during the gating processes. *Biophys J.* **74**:2926–44.

Spassov, V., L. Yan. 2008. A fast and accurate computational approach to protein ionization. *Protein Science.* **17:** 1955-1970.

Stanley S, J. Dias, D. D'Arcangelis, C. Mannella. 1995. Peptide-specific antibodies as probes of the topography of the voltage-gated channel in the mitochondrial outer membrane of Neurospora crassa. *J Biol Chem*. **270:** 16694–700.

Stevens, C.F., 1972. Inferences about membrane properties from electrical noise measurements. *Biophys J.* **12**(8): 1028–1047.

Stillinger, F.H., Rahman, A. 1974. Improved simulation of liquid water by molecular dynamics. *Journal of Chem. Phys.*, **60**: 1545-1577.

Straub, J.E., M. Borkovec, and B.J. Berne. 1987. Calculation of dynamic friction on intramolecular degrees of freedom. *J Phys Chem*. **91**: p. 4995-4998.

Swope, W.C.; Andersen, H.C.; Berens, P.H.; and Wilson, K.R. 1982. A computer simulation method for the calculation of equilibrium constants for the formation of physical clusters of molecules: Application to small water clusters. *J. Chem. Phys.* **76**: 637.

Takagi, H., D.S. Shi, Y. Ha, N.M. Allewell, and E.C. Theil. 1998. Localized unfolding at the junction of three ferritin subunits - A mechanism for iron release? *Journal of Biological Chemistry*. **273**: p. 18685-18688.

Tamm, L., X. Han. 2000. Viral fusion peptides: a tool set to disrupt and connect biological membranes. *Biosci. Rep.* **20:** 501-518.

Teijido, O., R. Ujwal, C. Hillerdal, L. Kullman, T. Rostovtseva, J. Abramson. 2012. Affixing N-terminal α-helix to the wall of the voltage-dependent anion channel does not prevent its voltage gating. *J Biol Chem.* **287**(14): 11437-45.

TGES Biology. Online Text. 2014. http://tgesbiology.weebly.com/.

Theil, E.C., M. Matzapetakis, and X.F. Liu. 2006. Ferritins: iron/oxygen biominerals in protein nanocages. *Journal of Biological Inorganic Chemistry.* **11**: p. 803-810.

Theil, E.C., X.F.S. Liu, and T. Tosha. 2008. Gated pores in the ferritin protein nanocage. *Inorganica Chimica Acta*. **361**: p. 868-874.

Theil, E.C. 2011. Ferritin protein nanocages use ion channels, catalytic sites, and nucleation channels to manage iron/oxygen chemistry. *Current Opinion in Chemical Biology.* **15**: p. 304-311.

Theil, E.C. 2013. Ferritin: the protein nanocage and iron biomineral in health and in disease. *Inorg Chem.* **52**(21): p. 12223-33.

Theil, E.C., R.K. Behera, and T. Tosha. 2013. Ferritins for chemistry and for life. *Coordination Chemistry Reviews*. **257**: p. 579-586.

Toghraee R, Lee KI, Papke D, Chiu SW, Jakobsson E, Ravaioli U. 2010. Simulation of Ion Conduction with covalently attached β-cyclodextrin based on Boltzmann Transport Monte Carlo model. *J. Comput. Theor. Nanosci.* **12**: 2555-2567.

Törnroth-Horsefield S, Neutze R. 2008. Opening and closing the metabolite gate. Proc Natl Acad Sci USA. **105**:19565–6.

Torrie, G. M. & J. P. Valleau. 1977. Nonphysical sampling distributions in Monte Carlo free energy estimation: Umbrella sampling. *J. Comp. Phys.* **23**: 187-199.

Tosha, T., H.-L. Ng, O. Bhattasali, T. Alber, and E.C. Theil. 2010. Moving Metal Ions through Ferritin-Protein Nanocages from Three-Fold Pores to Catalytic Sites. *Journal of the American Chemical Society.* **132**: p. 14562-14569.

Tosha, T., R.K. Behera, and E.C. Theil. 2012. Ferritin Ion Channel Disorder Inhibits Fe(II)/O-2 Reactivity at Distant Sites. *Inorganic Chemistry.* **51**: p. 11406-11411.

Tosha, T., R.K. Behera, H.-L. Ng, and O. Bhattasali, Alber, T., Theil, E. C. 2012. Ferritin Protein Nanocage Ion Channels: Gating by N-Terminal Extensions. *J. Biol. Chem*. **287**: p. 13016-13025.

Toussaint, L., L. Bertrand, L. Hue, R.R. Crichton, and J.P. Declercq. 2007. High-resolution X-ray structures of human apoferritin H-chain mutants correlated with their activity and metalbinding sites. *Journal of Molecular Biology*. **365**: p. 440-452.

Treffry, A. and P.M. Harrison. 1984. Spectroscopic studies on the binding of iron, terbium, and zinc by apoferritin. *J Inorg Biochem*. **21**(1): p. 9-20.

Treffry, A., E.R. Bauminger, D. Hechel, N.W. Hodson, I. Nowik, S.J. Yewdall, and P.M. Harrison. 1993. Defining the roles of the threefold channels in iron uptake, iron oxidation and ironcore formation in ferritin - a study aided by site-directed mutagenesis. *Biochemical Journal.* **296**: p. 721-728.

Turano, P., D. Lalli, I.C. Felli, E.C. Theil, and I. Bertini. 2010. NMR reveals pathway for ferric mineral precursors to the central cavity of ferritin. *Proceedings of the National Academy of Sciences of the United States of America.* **107**(2): p. 545-550.

Ujwal R., D. Cascio, V. Chaptal, P. Ping, J. Abramson. 2009. Crystal packing analysis of murine VDAC1 crystals in a lipidic environment reveals novel insights on oligomerization and orientation. *Channels (Austin).* **3**:167–70.

Ujwal R, Cascio D, Colletier J-P, Faham S, Zhang J, Toro L, Ping P, Abramson J. 2008. The crystal structure of mouse VDAC1 at 2.3 A resolution reveals mechanistic insights into metabolite gating. *Proc Natl Acad Sci USA*. **105:** 17742–7.

Valiyaveetil F.I., M. Leonetti, T. Muir, R. Mackinnon. 2006. Ion selectivity in a semisynthetic K+ channel locked in the conductive conformation. *Science*. **314**: 1004–7.

Van Der Spoel, D., E. Lindahl, B. Hess, G. Groenhof, A.E. Mark, H.J. Berendsen. 2005. "GROMACS: fast, flexible, and free". *J Comput. Chem.* **26** (16): 1701–18.

van Gunsteren, W.F. and Berendsen, H.J.C. 1977. Algorithms for macromolecular dynamics and constraint dynamics. *Mol. Phys.*, **34**: 1311-1327.

Voet, D., J. Voet, and C. Pratt, 2008. Fundamentals of Biochemistry. Life at the Molecular Level. John Wiley & Sons, Inc.

Wardeska, G.G., V. B., and N.D. Chasteen. 1986. Metal Ion Complexes of Apoferritin. Evidence for Initial Binding in the Hydrophilic Channels. *J. Biol. Chem*. **261**: p. 6677-6683.

Warshel, A. and M. Karplus. 1972. Calculation of ground and excited state potential surfaces of conjugated molecules. I. Formulation and parametrization. *J. Amer. Chem. Soc*. **94**, 5612.

Warshel, A and M. Levitt. 1976. Theoretical studies of enzymic reactions: Dielectric, electrostatic and steric stabilization of the carbonium ion in the reaction of lysozyme. *Journal of Molecular Biology* **103** (2): 227–49.

Warshel A. and R.M. Weiss. 1980. An empirical valence bond approach for comparing reactions in solutions and in enzymes. *Journal of the American Chemical Society*, **102**: 6218-6226.

Watt, R.K. 2011. The many faces of the octahedral ferritin protein. *Biometals*. **24**: p. 489-500.

Watt, R.K. 2013. A Unified Model for Ferritin Iron Loading by the Catalytic Center: Implications for Controlling "Free Iron" during Oxidative Stress. *Chembiochem*. **14**: p. 415-419.

Wells, David A. 1859. The science of common things: a familiar explanation of the first principles of physical science. For schools, families, and young students., Publisher Ivison, Phinney, Blakeman. p. 290.

*Windhover's Review of Emerging Medical Ventures* 2003. The reemergence of Ion Channel Drug Discovery. **8(5)**: p. 9.

Wüthrich K. 1990. Protein structure determination in solution by NMR spectroscopy. *J. Biol. Chem.* **265** (36): 22059–62.

Xu X, W. Decker, M. Sampson, W. Craigen, M. Colombini. 1999. Mouse VDAC isoforms expressed in yeast: channel properties and their roles in mitochondrial outer membrane permeability. *J Membr Biol.* **170**: 89–102.

Yamashita, I., K. Iwahori, and S. Kumagai. 2010. Ferritin in the field of nanodevices. *Biochimica Et Biophysica Acta-General Subjects.* **1800**: p. 846-857.

Yang, A.S., M.R. Gunner, R. Sampogna, K. Sharp, B. Honig. 1993. On the calculations of pK's in proteins. *Proteins* **15**: 252–265.

Yang, X. and N.D. Chasteen. 1996. Molecular Diffusion into Horse Spleen Ferritin: A Nitroxide Radical Spin Probe Study. *Biophys. J.* **71**: p. 1587-1595.

Yuan, Z., D.N. Petsev, B.G. Prevo, O.D. Velev, and P. Atanassov. 2007. Two-dimensional nanoparticle arrays derived from ferritin monolayers. *Langmuir.* **23**: p. 5498-5504.

Zhang, B., J.N. Harb, R.C. Davis, S. Choi, J.W. Kim, T. Miller, S.H. Chu, and G.D. Watt. 2006. Electron exchange between Fe(II)-horse spleen ferritin and Co(III)/Mn(III) reconstituted horse spleen and Azotobacter vinelandii ferritins. *Biochemistry.* **45**: p. 5766-5774.

Zhang, B., R.K. Watt, N. Galvez, J.M. Dominguez-Vera, and G.D. Watt. 2006. Rate of iron transfer through the horse spleen ferritin shell determined by the rate of formation of Prussian Blue and Fe-desferrioxamine within the ferritin cavity. *Biophysical Chemistry*. **120**(2): p. 96-105.

Zhang, F., R.J. Gates, V.S. Smentkowski, S. Natarajan, B.K. Gale, R.K. Watt, M.C. Asplund, and M.R. Linford. 2007. Direct adsorption and detection of proteins, including ferritin, onto microlens array patterned bioarrays. *Journal of the American Chemical Society.* **129**: p. 9252-+.

Zhao, G.H., M.H. Su, and N.D. Chasteen. 2005. mu-1,2-1-Peroxo diferric complex formation in horse spleen ferritin. A mixed H/L-subunit heteropolymer. *Journal of Molecular Biology.* **352**: p. 467-477.

Zhao, G.H., P. Arosio, and N.D. Chasteen. 2006. Iron(II) and hydrogen peroxide detoxification by human H-chain ferritin. An EPR spin-trapping study. *Biochemistry.* **45**(10): p. 3429-3436.

Zhen, Z., W. Tang, C. Guo, H. Chen, X. Lin, G. Liu, B. Fei, X. Chen, B. Xu, and J. Xie. 2013 Ferritin Nanocages To Encapsulate and Deliver Photosensitizers for Efficient Photodynamic Therapy against Cancer. *ACS Nano.* **7**(8): p. 6988-6996.

Zheng, B., M. Uenuma, N. Okamoto, R. Honda, Y. Ishikawa, Y. Uraoka, and I. Yamashita. 2012. Construction of Au nanoparticle/ferritin satellite nanostructure. *Chemical Physics Letters.* **547**: p. 52-57.